Aircraft Engineering (Part-time)
MSc

Academic Year 2023 - 2026

Taner Cakir

Numerical Modelling of Structural Compromising Events on Various Types of Typical Airframe Structures (Crashworthiness or Bird Strike)

Supervisor: Dr. Ioannis Giannopoulos
February 2026

This thesis is submitted in partial fulfilment of the requirements for the degree of MSc Aircraft Engineering (Part-time)

© Cranfield University 2025. All rights reserved. No part of this publication may be reproduced without the written permission of the copyright owner.

Academic integrity declaration

I declare that:

- the thesis submitted has been written by me alone.
- the thesis submitted has not been previously submitted to this university or any other.
- that all content, including primary and/or secondary data, is true to the best of my knowledge.
- that all quotations and references have been duly acknowledged according to the requirements of academic research.

I understand that to knowingly submit work in violation of the above statement will be considered by examiners as academic misconduct.

Abstract

The aerospace industry's transition to monolithic carbon fibre reinforced polymer (CFRP) fuselages has introduced significant weight and fatigue benefits, but also critical vulnerabilities regarding low-velocity impact (LVI) events. Ground support operations pose a statistically high risk of impact damage, particularly to the main deck cargo door (MDCD). Unlike metallic structures, CFRP exhibits barely visible impact damage (BVID), where extensive internal failure can occur with minimal external indication. This thesis addresses the lack of high-fidelity numerical data for full-scale composite cargo doors by developing a multi-scale finite element (FE) model of the Airbus A350F MDCD using Abaqus/Explicit.

A semi-monocoque design featuring a monolithic skin and bonded omega stringers was modelled and subjected to impact energies of 5J, 20J, and 40J. The simulation incorporated Hashin's failure criteria for intralaminar damage and cohesive zone modelling (CZM) for skin-stringer delamination. Results indicate that while the structure remains semi-elastic at 5J, the 20J impact threshold generates critical "latent defects." At this energy, significant shear damage and delamination were observed up to the 15th ply, despite negligible surface indentation. At 40J, the failure mechanism transitions to catastrophic stringer decohesion driven by flange stiffness mismatch. The research concludes that visual inspection is statistically unreliable for post-incident airworthiness assessment and recommends mandatory ultrasonic testing for any reported ground contact, alongside design optimisations to taper stringer flanges.

Keywords:

Carbon Fibre Reinforced Polymer (CFRP), Low-Velocity Impact, Barely Visible Impact Damage (BVID), Finite Element Analysis (FEA), Cohesive Zone Modelling (CZM), Aircraft Cargo Door

Acknowledgements

I would like to express my sincere gratitude to my supervisor, Dr. Ioannis Giannopoulos, for his expert guidance, constructive feedback, and continuous encouragement throughout this research project.

I am deeply grateful to Airbus for sponsoring my Master's studies and providing the professional context that inspired this work.

Finally, a special thank you to my partner, Sibel Mas. Your unwavering support, patience, and understanding during the long hours of this process were invaluable. I could not have completed this journey without you.

Table of Contents

Academic integrity declaration i
Abstract ii
Acknowledgements iii
Table of Contents iv
List of Figures vii
List of Tables xiii
List of Equations xiv
List of Abbreviations xv
1 Introduction 1
1.1 Background and Motivation 2
1.2 Problem Statement 6
1.3 Aims and Objectives 10
1.4 Scope and Limitations 11
1.5 Thesis Outline 13
2 Literature Review 14
2.1 Principles of Airframe Structures 15
2.2 Aircraft Cargo Door Design Philosophy 19
2.3 Composite Materials in Aerospace Structures 22
2.4 Operational Loads and Impact Risks 27
2.4.1 The Ground Support Environment 27
2.4.2 Low-Velocity Impact Physics and BVID 29
2.4.3 The “Latent Defect” and Detection Challenges 30
2.5 Numerical Modelling of impact Events 32
2.5.1 Explicit Dynamic Solvers 33
2.5.2 Intralaminar Failure: Hashin’s Criteria 34
2.5.3 Interlaminar Failure: Cohesive Zone Modelling 35
2.5.4 Element Deletion and Mesh Sensitivity 36
2.6 Summary and Research Gap 37
3 Cargo Door Conceptual Design and Geometric Modelling 38
3.1 Design Requirements and Specifications 39
3.2 Structural Layout and Architecture 41
3.2.1 Monolithic Skin 41
3.2.2 Longitudinal Stiffeners (Omega Stringers) 42
3.2.3 Circumferential Frames (C-Frames) 43
3.2.4 Shear Clips 44
3.3 Geometric Modelling in CATIA V5 45
3.3.1 Fuselage Lofting and Surface Generation 45
3.3.2 Component and Assembly Generation 46
3.4 CAD Model Generation 47
4 Finite Element Model Development and Simulation Methodology 48

4.1 Pre-Processing and Meshing 49
4.1.1 Element Selection 50
4.1.2 Mesh Generation and Quality 52
4.2 Impact Source Modelling 54
4.3 Material and Failure Modelling 56
4.3.1 Material Specifications and Layup Definition 56
4.3.2 Constitutive Damage Framework 58
4.4 Boundary Conditions, Loads, and Interactions 63
4.4.1 Structural Boundary Conditions 63
4.4.2 Impactor Kinematics and Loading 64
4.4.3 Surface Interaction Assignments 65
4.5 Solver Setup 66
5 Results 68
5.1 Model Verification 68
5.1.1 Energy Balance Analysis 69
5.1.2 Numerical Signatures of Mass Scaling 70
5.2 Chronological Impact Analysis 71
5.2.1 Phase I: Inertial Loading & Contact Initiation 72
5.2.2 Phase II: Velocity Deceleration & Energy Absorption 73
5.2.3 Phase III: Peak Deflection & Elastic Rebound 75
5.3 Damage and Failure Analysis 76
5.3.1 Intralaminar Matrix and Shear Failure 77
5.3.2 Interlaminar Interface Integrity 79
5.3.3 Fibre Fracture and Penetration Depth 80
6 Discussion 82
6.1 Analysis of Failure Mechanisms 83
6.1.1 Matrix Initiation and Invisible Micro-Cracking 84
6.1.2 The Mechanics of Barely Visible impact Damage (BVID) 85
6.1.3 Interlaminar Coupling and Stringer Decohesion 86
6.1.4 Stringer Interlaminar Failure 88
6.2 Structural Performance Evaluation 91
6.2.1 Energy Absorption Efficiency 92
6.2.2 Ultimate Load Capacity 94
6.2.3 Post-Impact Stability and Permanent Set 95
6.3 Critique of Modelling Approach 96
6.3.1 Geometric Idealisation and Boundary Effects 96
6.3.2 Numerical Stability and Element Fidelity 97
6.3.3 Limitations of Residual Strength Assessment 98
6.4 Implications of Design Improvement 99
6.4.1 The Limits of Visual Inspection 99
6.4.2 Recommendations for Maintenance Protocols 100
6.4.3 Design Optimisation and Future Principles 101

7 Conclusion and Future Work 102
7.1 Conclusion 102
7.2 Recommendations for Future Work 103
7.2.1 Experimental Validation 103
7.2.2 Residual Strength Analysis (Compression After Impact) 103
7.2.3 Environmental Sensitivity 103
References 104
Appendices 115
Appendix A Ethical approval letter 115

List of Figures

Figure 1. Experimental vs Numerical Deformation of Al Alloy (5) 2
Figure 2. Evolution Composite Application (6) 2
Figure 3. Comparison of Composite and Metal Fatigue Behaviour (9) 3
Figure 4. Barely Visible Impact Damage on a Composite (12) 4
Figure 5. EASA AMC for Composite Aircraft Structures (15) 5
Figure 6. Structure of a Composite Material (18) 6
Figure 7. Schematic Impact Damage Patterns Representation (20) 7
Figure 8. Impact Damage for TRI Laminate (20) 7
Figure 9. Impact Damage for UD Laminate (21) 7
Figure 10. Finite Element Models for Impact Analysis of Composite Plate (22) (21) 8
Figure 11. A300/310 Cargo Door (23) 9
Figure 12. Aircraft Structural Design Evolution (24) 15
Figure 13. Monocoque Structure (26) 15
Figure 14. Semi-Monocoque Structure (26) 15
Figure 15. Stresses and Strains on an Aircraft Structure (25) 16
Figure 16. Cabin Pressurisation Induced Hoop and Tensile Stress (25) 16
Figure 17. Fuselage Structural Elements (31) 17
Figure 18. Stress Concentration around Door and Window (33) 17
Figure 19. Example of a Door-Surround-Structure with High Stress Areas (34) 18
Figure 20. A350- Freighter Cargo Door (35) 18
Figure 21. A330-200F Cargo Loading Operation (36) 19
Figure 22. A330-200F Cargo Door Inside View (37) 19
Figure 23. B777-Freighter Main Deck Cargo Door (41) 20
Figure 24. B787 Dreamliner Composite Cargo Door (43) 21
Figure 25. A350 Composite Passenger Door(44) 21
Figure 26. Comparison of materials use in Boeing 767 and Boeing 787 (45) .. 22
Figure 27. CFRP Usage over Time in Airbus and Boeing Aircraft (45) 22

Figure 28. Global Demand for CFRP Composites Over Time (45)..... 22

Figure 29. B787 Fuselage Section (46)..... 23

Figure 30. B787 One-shot Nose Section (46)..... 23

Figure 31. Example of Tube in Compression with and without Post Buckling (46) 23

Figure 32. Matrix Tensile Failure (DAMAGEMT) and CFRP Laminate Configurations 24

Figure 33. Chen et al. Experimental Test Set-Up Overview (48)..... 25

Figure 34. Tensile Thickness in Z direction for Unpinned and Z-Pinned Specimen (48) 25

Figure 35. Cen et al. Study Specimen Manufacturing and Preparation (48) 26

Figure 36. FEA Analysis Normal Stress Results for Z-Pinned Specimen Stress Results after Cool-Down (48) 26

Figure 37. Ground Handling Services Sequence for a Flight Operation (49) ... 27

Figure 38. Ground Damage Distribution Per Phase (50)..... 28

Figure 39. Typical Ground Support Service and Handling Operations around an Aircraft (50)..... 28

Figure 40. Ultrasonic Phased Array C-Scan Results for $\boldsymbol{20\,J}$ and $\boldsymbol{30\,J}$ Impact (51) 29

Figure 41. Camera Images of Damaged Specimens with Various Range of Impact Energy Levels (52)..... 30

Figure 42. Thermal Images of Damaged Specimens with Various Range of Impact Energy Levels 30

Figure 43. Damage Detection Algorithm Framework with C-Scans with X-ray CT- scans (53)..... 31

Figure 44. X-Ray CT scan (red colour) and Ultrasonic Results (blue colour) for a Specimen Impacted with $\boldsymbol{17.5\,J}$ Energy (53)..... 31

Figure 45. Experimental and FEA Model Test Specimen Overview Schematic (54) 32

Figure 46. Comparison of Experimental and FEA Test (54)..... 32

Figure 47. Equivalent Plastic Strain (PEEQ) Results for Specimen (a) without Scaling and (b) with Scaling (55) 33

Figure 48. Experimental vs FEA Simulation Load-Displacement Curve Comparison (56)..... 34

Figure 49. Impact Simulation Phase Comparison with Load-Displacement Curve (56) 34
Figure 50. Experimental and FEA Comparison of Impact Damage (56)..... 36
Figure 51. Low-Velocity Impact FEA Model with Graded Mesh Strategy (56).. 36
Figure 52. A350 Freighter Cargo Door Mock-Up Display (57)..... 39
Figure 53. Multifunctional Fuselage Demonstrator MFFD Demonstrator Upper Half of Fuselage (58) 40
Figure 54. Isometric view of the monolithic Inner and Outer Skin..... 41
Figure 55. Isometric View of Omega Stringers 42
Figure 56. Cross-Sectional Dimensions of the Omega Stringer Profile 42
Figure 57. Isometric View of C-Frames 43
Figure 58. Cross-Sectional Dimensions of the C-Frames Profile 43
Figure 59. Isometric View of Shear Clips 44
Figure 60. Cross-Sectional Dimensions of the Shear Clips..... 44
Figure 61. CATIA V5 Reference Planes Setup - Painting Gallery 45
Figure 62. Isometric view of the full cargo door assembly in CATIA V5 46
Figure 63. Fuselage Overview without Outer and Inner Skin 46
Figure 64. Schematic Showing the Full Door vs The Simplified Skin-Stringer Domain Used for Analysis 47
Figure 65. Transition from 3D Model to FEA 48
Figure 66. Element Types and Mesh Density (59) 49
Figure 67. Continuum Shell Model (SC8R) (60,62)..... 50
Figure 68. Element Type Selection in Abaqus – Continuum Shell SC8R..... 50
Figure 69. Discrete Rigid Element Type R3D4 (64) 51
Figure 70. Impact Zone Mesh Modelling 52
Figure 71. Assembly Mesh Generation 52
Figure 72. Mesh Element Controls..... 53
Figure 73. ASTM D7136 - Impact Device..... 54
Figure 74. Impactor Model..... 55
Figure 75. Simulation Setup Example for Low-Velocity Impact Damage of Composite Laminates (70)..... 55

Figure 76. Schematic of the Laminate Stacking Sequence 57
Figure 77. Abaqus Shell Element Elasticity in Plane Stress (72)..... 58
Figure 78. Elasticity Material Property Values 58
Figure 79. Abaqus Hashin Damage Initiation Criteria (73) 59
Figure 80. Hashin Damage Material Property Values (74) 59
Figure 81. Abaqus Hashin Damage Initiation Criteria (75) 60
Figure 82. Hashin Damage Material Property Values (74) 60
Figure 83. Cohesive Elements vs Cohesive Contact Approach (78) 61
Figure 84. Abaqus Typical Traction-Separation Response (78) 62
Figure 85. Abaqus Traction-Separation Modelling (79) 62
Figure 86. Abaqus Cohesive Contact 62
Figure 87. Abaqus Quads Damage Initiation 62
Figure 88. Abaqus B-K Damage Evolution 62
Figure 89. Abaqus Structural BC - Pinned 63
Figure 90. Skin-Stringer Assembly BC - Pinned 63
Figure 91. Impactor BC - $\boldsymbol{U3}$ 64
Figure 92. Impactor BC - $\boldsymbol{V3}$ 64
Figure 93. Abaqus General Contact Interaction 65
Figure 94. Abaqus Surface Interaction Assignments 65
Figure 95. Abaqus Dynamic Explicit Solver 66
Figure 96. Dynamic Explicit Step - Mass Scaling 67
Figure 97. Dynamic Explicit Step - Mass Time Increments 67
Figure 98. 25 $\boldsymbol{J}$ Impact of a CFRP Plate (2 mm) (13) 68
Figure 99. Global Energy History for the 20 $\boldsymbol{J}$ (2 $\boldsymbol{m/s}$) Impact Scenario demonstrating ETOTAL Preservation 69
Figure 100. Transient Stress Distribution and Impactor Interaction at Peak Displacement ($\boldsymbol{t}$ = 0.0025 $\boldsymbol{s}$) 69
Figure 101. Explicit Solver Job Monitor illustrating Stable Time Increment Decay and Mass Scaling Trigger ($\boldsymbol{t} \approx \boldsymbol{0.016\ s}$) 70
Figure 102. Impact Force Comparison 72

Figure 103. Velocity Comparison 73

Figure 104. Displacement Comparison 75

Figure 105. Isometric View of the Localised Damage Zone ($\mathbf{40\,J}$ Impact Case) 76

Figure 106. Evolution of Matrix Tensile Damage (DAMAGEMT) on the Last Ply (Rear Face) Impact Zone Across Impact Energies 77

Figure 107. Evolution of Matrix Compressive Damage (DAMAGEMC) on the Front Face Impact Zone Across Impact Energies 77

Figure 108. Cross-sectional 'Cut View' DAMAGESHR Penetration Depth Across Impact Energies 78

Figure 109. Front Face DAMAGESHR Impact Zone Length Across Impact Energies 78

Figure 110. Top-down view of the Skin-Stringer Interface showing CSDMG distribution 79

Figure 111. Cross-sectional 'Cut View' comparing DAMAGEFT Penetration Depth Across Impact Energies 80

Figure 112. Ply View Comparing DAMAGEFT Penetration Depth Across Impact Energies 81

Figure 113. $\mathbf{30\,J}$ Experimental Impact on 17 Ply Painted Laminate (84) 82

Figure 114. $\mathbf{40\,J}$ Impact Simulation on 16 Ply Painted Laminate (a) Top-View (b) Impact Zone 82

Figure 115. $\mathbf{5\,J}$ Impact Loading Phase Cut View 83

Figure 116. $\mathbf{5\,J}$ Impact Maximum Penetration Cut View 83

Figure 117. $\mathbf{5\,J}$ Impact Rebound Phase Cut View 83

Figure 118. Top View of Tensile Matrix Damage for $\mathbf{5\,J}$ (a) Ply 1 - Top Face (b) Ply 9 (c) Ply 13 (d) Ply 14 84

Figure 119. Cross-sectional View of Shear Damage (DAMAGESHR) Comparing the $\mathbf{5\,J}$ Partial Penetration vs. $\mathbf{40\,J}$ Full Penetration 84

Figure 120. Cross-sectional View of $\mathbf{20\,J}$ Impact Simulation Shear Damage (DAMAGESHR) 85

Figure 121. $\mathbf{20\,J}$ Impact Simulation Painted Assembly (a) Impact Zone (b) Isometric View 85

Figure 122. Comparative View of $\mathbf{20\,J}$ Showing Two Separate Failure Zones vs. $\mathbf{40\,J}$ Showing Merged Failure 86

Figure 123. Cross-sectional View of the $\mathbf{5}\,\boldsymbol{J}$ Impact Showing CSDMG delamination 87

Figure 124. View of Stringer-only showing Shear Damage (DAMAGESHR) Across Impact Energies 88

Figure 125. $\mathbf{20}\,\boldsymbol{J}$ Case Shear Damage on Lower Plies (1-8) (a) PLY 1 (b) PLY 3 (c) PLY 5 89

Figure 126. $\mathbf{20}\,\boldsymbol{J}$ Case Shear Damage on Upper Plies (9-16) (a) PLY 9 (b) PLY 13 (c) PLY 16 89

Figure 127. $\mathbf{30}\,\boldsymbol{J}$ Case Shear Damage on Lower Plies (1-8) (a) PLY 1 (b) PLY 6 (c) PLY 8 90

Figure 128. $\mathbf{30}\,\boldsymbol{J}$ Case Shear Damage on Upper Plies (9-16) (a) PLY 10 (b) PLY 13 (c) PLY 16 90

Figure 129. Ply Stack Plot for Stringer Composite Layup 90

Figure 130. Comparing Damage Dissipation Energy (ALLDMD) Across Impact Energies 92

Figure 131.Comparing Elastic Strain Energy (ALLSE) Across Impact Energies 93

Figure 132. Impact Force Comparison 94

Figure 133. Top Face View Across Impact Energies $\mathbf{5}\ \boldsymbol{J}$, $\mathbf{20}\ \boldsymbol{J}$, and $\mathbf{40}\ \boldsymbol{J}$ 94

Figure 134. Displacement Comparison 95

Figure 135. Cut View Across Impact Energies $\mathbf{5}\,\boldsymbol{J}$, $\mathbf{20}\,\boldsymbol{J}$, and $\mathbf{40}\,\boldsymbol{J}$ 95

Figure 136. Development of FEA Model from 3D Cargo Door Model 96

Figure 137. Max Degradation and Mass Scaling Employed for Explicit Simulation 97

Figure 138. ASTM D7137 Test Specimen and Fixture Assembly Overview (86) 98

Figure 139. Effect of Painted Aircraft Livery on Composite Visual Inspections (87) 99

Figure 140. Strain Gauge Instalment example on PZL 130 Orlik for Loads Measurement at Critical Locations (88) 100

List of Tables

Table 1.1 Comparison of Aircraft Model to OEW (7) 3

Table 2.1 From Patel et al. (47) Peak impact-resisting force, peak displacement, and residual displacement 24

Table 2.2 Experimental Results for TTS for Unpinned and Z-Pinned Specimen (48) 25

Table 2.3 Cohesive Interface Modelling, Bilinear Traction-Separation Model in Abaqus 35

Table 4.1 Assembly Mesh Element Types 51

Table 4.2. Material Properties for Hexcel AS4/8552 Unidirectional Pre-preg ... 56

Table 5.1: Evolution of Structural Stiffness via Velocity Gradients 74

Table 5.2: Definition of Field Output Variable for Damage Evaluation..... 76

List of Equations

(2.1) 33
(2.2) 33
(2.3) 33
(2.4) 35
(2.5) 35
(2.6) 35
(4.1) 61
(4.2) 61
(4.4) 63
(4.5) 64
(4.6) 67
(4.7) 67
(5.1) 74

List of Abbreviations

Al	Aluminium
AMC	Acceptable Means of Compliance
AMM	Aircraft Maintenance Manual
ASTM	American Society for Testing and Materials
BC	Boundary Condition
BVID	Barely Visible Impact Damage
B-K	Benzeggagh-Kenane
CAD	Computer-Aided Design
CAI	Compression After Impact
CFL	Courant-Friedrichs-Lewy
CFRP	Carbon Fibre Reinforced Plastic
CM	Certification Memorandum
CS	Certification Specification
CT	Computed Tomography
CZM	Cohesive Zone Modelling
CDM	Continuum Damage Mechanics
DSS	Door-Surround-Structure
EASA	European Union Aviation Safety Agency
FAA	Federal Aviation Administration
FAR	Federal Aviation Regulations
FE	Finite Element
FEA	Finite Element Analysis
GFRP	Glass Fibre Reinforced Plastic
GSE	Ground Support Equipment
M&S	Modelling and Simulation
NDT	Non-Destructive Testing
NLGEOM	Nonlinear Geometry
PMC	Polymer Matrix Composites
SEM	Scanning Electron Microscope
SHM	Structural Health Monitoring
TRI	Tri-axial
ISO	International Organization for Standardisation

UD	Unidirectional
UL	Ultimate Load
UT	Ultrasonic Testing
WOE	Weight of Evidence
XWB	Xtra Wide Body
3D DIC	Three-Dimensional Digital Image Correlation

1 Introduction

This chapter introduces the research undertaken for this thesis, which investigates the complex structural response of composite components on an aircraft to compromising events. The adoption of composite material on modern airframe design, shifting towards a weight saving and improved fatigue resistance approach has its own structural predicaments. The unpredictable behaviour and novel failure modes of composite laminates are far different compared to known performance of metallic alloys.

The primary factor that drives this material shift and industrial mindset change is the pursuit of fuel efficiency, exemplified by modern aircraft such as the Airbus A350 XWB with carbon fibre reinforced plastic (CFRP) wings and the Boeing 787 with more than 80 percent composite when measured by volume (1). A rule of thumb in aviation where a 1 percent reduction in weight would benefit the reduction in fuel consumption by 0.75 percent, resulting in a significant economic advantage for airlines in long term over airlines which utilise a fleet of non-composite aircrafts (2).

Despite their advantages, composite materials are vulnerable to barely visible impact damage (BVID), a significant concern for the aviation industry. Low-velocity impacts, such as a tool drop during maintenance, can induce critical subsurface failures like matrix cracking and delamination. Because these defects are not externally visible, they pose a serious challenge to structural health monitoring (SHM) and threaten the overall structural integrity of the aircraft (3).

This research confronts this challenge by developing a high-fidelity numerical model of a composite main cargo door to investigate its behaviour during structural compromising events. The work aims to provide crucial insights into damage mechanics, contributing to more robust predictive methodologies for modern airframe structures. The remainder of this introduction will formalise this investigation by presenting the core research objectives, defining the project's scope, and outlining the section-by-section structure of the thesis.

1.1 Background and Motivation

In aerospace industry, high strength aluminium (Al) alloys such as the 2000 and 7000 series have been the primary choice for aircraft manufacturing. This preference was based on several advantages such as the versatile compositions of alloys, manufacturing compatibility and the well-understood structural behaviour. This predictability made life assessment reliable and allowed straight forward maintainability compared to composite materials (4) (5).

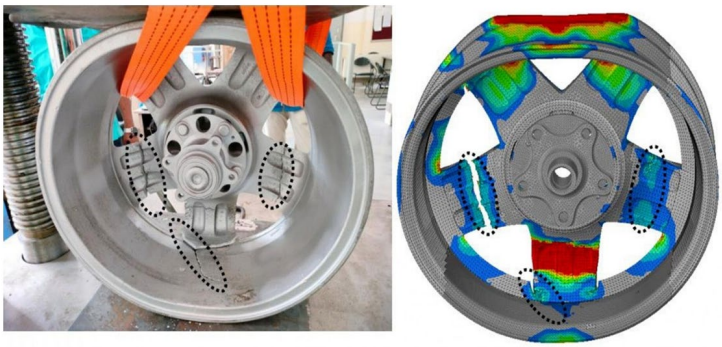

Figure 1. Experimental vs Numerical Deformation of Al Alloy (5)

Although metals are still required for high-stress or high-temperature applications, the shift to composites is a fundamental evolution in airframe design. This is driven by the significant fuel efficiency gains from their high strength-to-weight ratio. For instance, the Airbus A350 features an airframe of over 50% composite material, contributing to its 25% improvement in fuel efficiency. The Boeing 787 also features a similar composite-heavy airframe, highlighting this industry-wide trend, which is illustrated in Figure 3 (6).

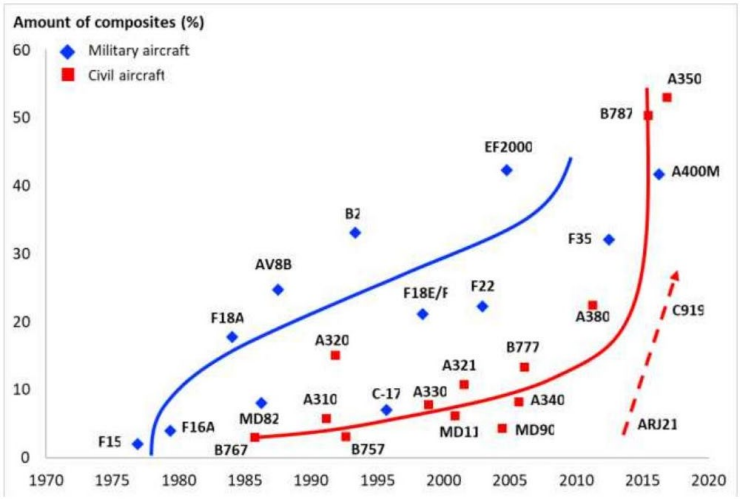

Figure 2. Evolution Composite Application (6)

A significant challenge in civil aviation today is the drive to reduce aircraft weight. This goal is critical because it links directly to several key benefits, including improved fuel efficiency, increased payload capacity, and lower atmospheric emissions. Composites, with their excellent strength-to-weight performance, have become the primary material to achieve this. They allow for lighter structural designs without sacrificing strength, which in turn provides significant economic advantages for airlines and aircraft manufacturers. Table 1.1 illustrates the clear weight-saving benefits of adopting composite materials (7).

Aircraft Model	Primary Material	Percentage of Composites	Operational Empty Weight (OEW)
Boeing 767	Aluminium	~5%	179,000 lbs
Boeing 787	Composite	~50%	134,000 lbs
Airbus A330	Aluminium	~10%	176,000 lbs
Airbus A350	Composite	~53%	138,000 lbs

Table 1.1 Comparison of Aircraft Model to OEW (7)

Beyond weight savings, composites offer several other advantages, notably superior fatigue and corrosion resistance, along with improved moisture resistance. These characteristics lead directly to a reduced maintenance burden and enable longer inspection intervals, as the material remains largely unaffected by these environmental factors. Metallic alloys, however, are susceptible to these very issues, experiencing fatigue degradation and a reduction in lifespan (6,8). The expectancy of composite materials being more damage tolerant than metals is demonstrated in Figure 3 (9).

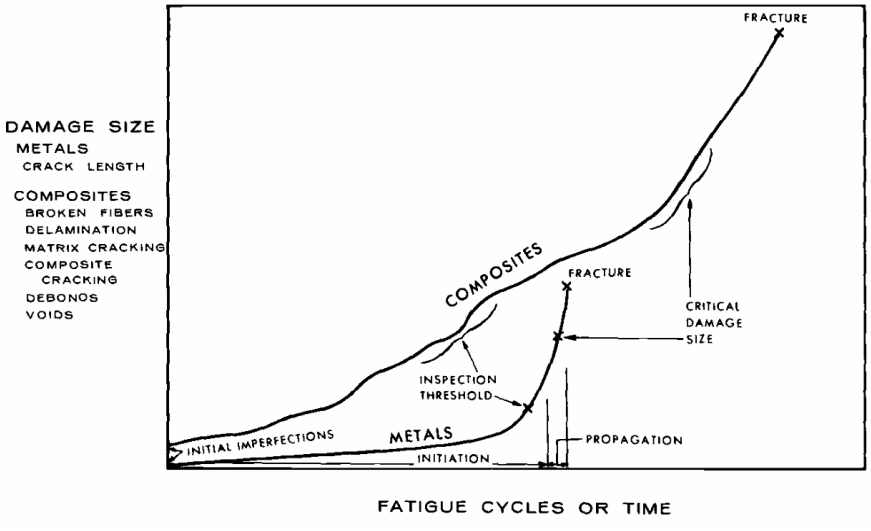

Figure 3. Comparison of Composite and Metal Fatigue Behaviour (9)

However, despite these advantages, another distinct characteristic of composite materials lies in their failure modes. Compared to the known and predictable mechanical failures of metals, composite failures are notably harder to predict. This is due to their inherent material composition, where the fibres, matrix, and binding resin can each contribute to the composite's overall failure in unique ways. This behaviour is often difficult to foresee and can sometimes remain hidden from view (10).

The phenomenon of localised damage within composite materials, such as fibre fractures, delamination, or matrix cracking, with little to no external visibility is known as barely visible impact damage (BVID). This damage is considered dangerous due to its possible effect on the material's residual strength. BVID typically originates from low-velocity and low-energy impacts, such as a tool being dropped during maintenance (10). As a general guideline, visually detectable damage between 0.3 mm and 0.5 mm could indicate the existence of BVID (11).

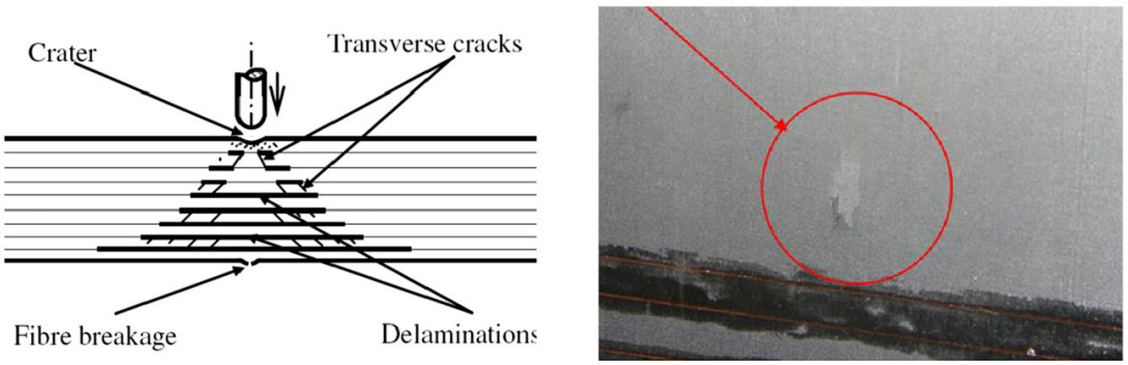

Figure 4. Barely Visible Impact Damage on a Composite (12)

As a result of the buckling of delaminated plies, composites can be significantly affected by low-velocity impact damage, potentially leading to a loss of up to 75% of their compression characteristic. For any aircraft structure made from composites, the residual strength must remain above the ultimate load (UL) to prevent catastrophic failure. This phenomenon, unlike the slow-growth crack approach seen in metals, poses a significant risk and thus places great importance on the accurate detection and timely repair of such damage (13).

Aircraft manufacturers must adhere to strict regulations from airworthiness authorities, such as the European Union Aviation Safety Agency (EASA) and the Federal Aviation Administration (FAA). For large aeroplanes, EASA's regulations are defined in CS-25. As a guide to satisfying the compliance requirements for composite structures,

EASA provides the acceptable means of compliance (AMC) 20-29, which aligns with the FAA's advisory circular (AC) 20-107B (14).

AMC 20-29 suggests the “building block” approach, which uses a mix of experimental testing and analysis. This method is used to demonstrate compliance with the damage tolerance and residual strength of composite structures for certification (15).

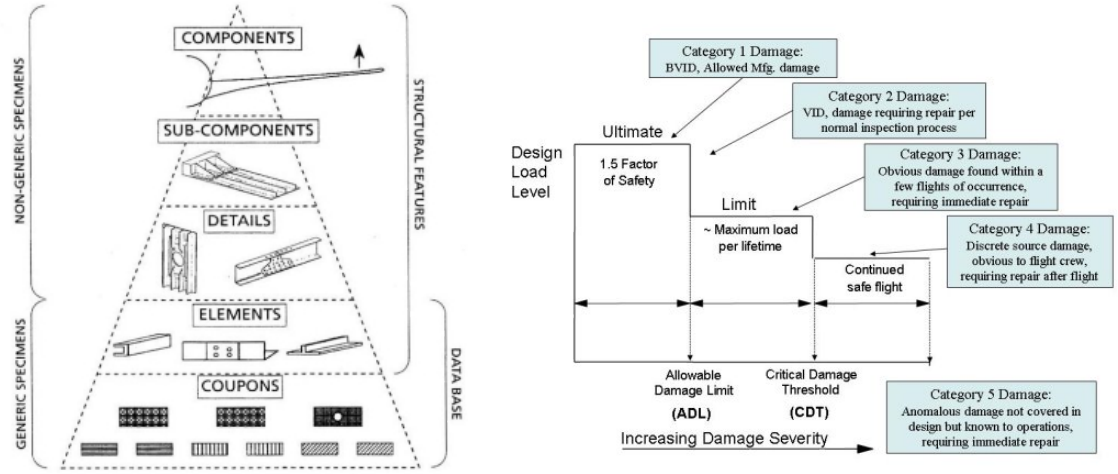

Figure 5. EASA AMC for Composite Aircraft Structures (15)

These legacy regulations and methods of compliance are costly and time consuming, largely due to their heavy reliance on experimental testing requirements. This, in turn, increases the need for effective modelling and simulation (M&S). This challenge has motivated the aviation industry, prompting EASA to publish a proposal for a new certification memorandum (CM), CM-S-014. This memorandum concerns the utilisation of M&S to support compliance with CS-25. A key aspect of this document is the requirement for simulations to produce reliable and accurate results, ultimately enabling the design of safer and more optimised aircraft (16).

1.2 Problem Statement

While there is a strong push for the increased use of M&S in aircraft design and certification, achieving reliable and accurate results remains the major roadblock. This difficulty stems from the composite materials themselves; their heterogeneous microstructure and anisotropic properties make the failure process and micro-mechanics distinct for each scenario (17).

To familiarise the reader with the composite material's structure, it can be defined by its two primary components. The first is the fibre, which acts as the reinforcement, providing the composite with its essential strength and stiffness. The second is the matrix material, which binds the fibres together and gives the component its final shape. The matrix is also the structure that is first exposed to any external forces (18).

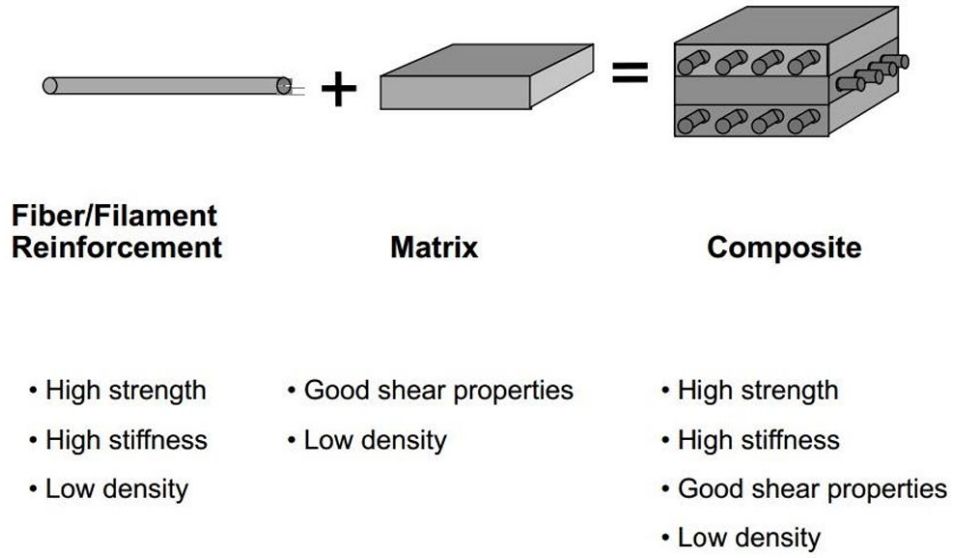

Figure 6. Structure of a Composite Material (18)

For monolithic materials, such as metals, the failure modes are significantly different. Their main failure concepts are yielding and fracture, which are examined by the theories of plasticity and fracture mechanics. When considering yielding, metals have a clear shear force threshold for inelastic behaviour. The most common class of composites, polymer matrix composites (PMC) like CFRP, do not exhibit this same threshold. The behaviour of cracks also differs. In metals, the growth of a single crack is the primary concern. In PMCs, however, matrix cracks are generally arrested within the composite volume. Instead, the concern for composites involves much more complex failure modes, such as the connection of multiple cracks or crack formations within the fibres, which eventually lead to the failure of the part (19).

As mentioned before, these complex failure modes make it particularly challenging to reliably and effectively understand the composite structure's response to a low-velocity impact. Figure 7 demonstrates the main failure modes involved, such as matrix cracking, fibre breakage, and delamination (debonding) (20).

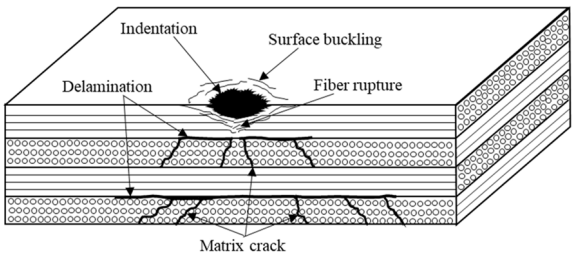

Figure 7. Schematic Impact Damage Patterns Representation (20)

In a study on the static residual tensile strength of unidirectional (UD) and tri-axial (TRI) Glass Fibre Reinforced Plastic (GFRP) composites, Kim et al. (2020) visually demonstrated the results of low-velocity impacts using a scanning electron microscope (SEM). They also investigated the resulting stress concentrations with three-dimensional Digital Image Correlation (3D DIC) measurements (20).

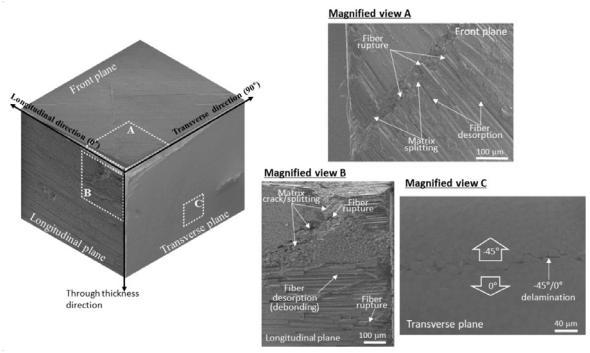

Figure 8. Impact Damage for TRI Laminate (20)

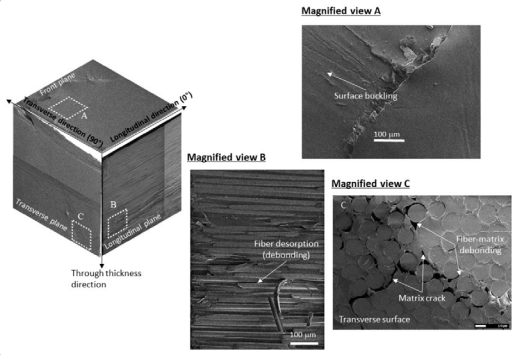

Figure 9. Impact Damage for UD Laminate (21)

The study concluded that even at the same impact energy level, the indent shape influences the reduction of residual strength. Furthermore, it was found that tri-axial GFRP is much more susceptible to both impact indentation and the resulting loss of in-plane tensile strength. The study also noted that evaluating this type of damage with non-destructive testing is not easy (20).

Another study carried out by Quo et al. reviews different models in finite element analysis (FEA) for the structural analysis of composite structures. The authors note that the success of FEA models is heavily dependent on the right choice of advanced

simulation methods, for example, cohesive zone modelling (CZM) and continuum damage mechanics (CDM). Furthermore, different environments or scenarios require the implementation of different FEA simulations, which can be named implicit or explicit. While implicit methods are typically used for general linear and nonlinear problems, explicit methods are more successful for highly dynamic, nonlinear, and, most importantly, contact situations (22).

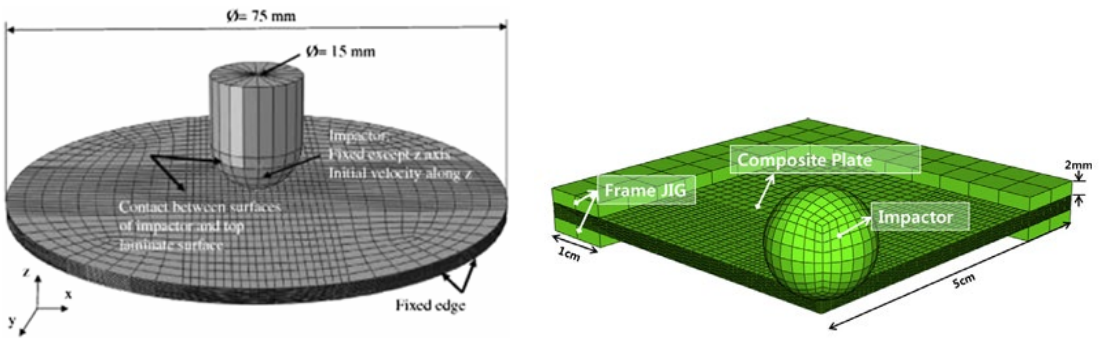

Figure 10. Finite Element Models for Impact Analysis of Composite Plate (21,22)

Existing research in this field has, to date, been generally based on simpler models, such as the flat plates or "coupons" represented in Figure 10. A strong argument exists that more complex modelling, which accurately represents the reality of large-scale airframe components, must also be validated. Carrying out these validation exercises is essential to advance aerospace manufacturing and design. This validation will also ensure FEA methods are more accurate, helping to align them with developing M&S safety regulations. Ultimately, this would contribute to a faster, more efficient adoption of these new rules, which in turn would help reduce significant costs in the manufacturing environment.

Therefore, while extensive research has focused on modelling simple coupons, there is a clear and defined gap in the literature regarding the application and validation of these high-fidelity models on a full-scale, structurally representative assembly such as an aircraft's main cargo door.

These challenges are magnified when applying FEA simulations to real-world components, such as an aircraft's main deck cargo door. This is a complex, curved assembly, typically constructed in a conventional monocoque style from an inner and outer skin, frames, longerons, and stringers (23).

Therefore, while research exists for modelling coupons, there is a clear and defined gap in the literature concerning the application and validation of these high-fidelity models on a full-scale, structurally representative assembly like an aircraft's main cargo door.

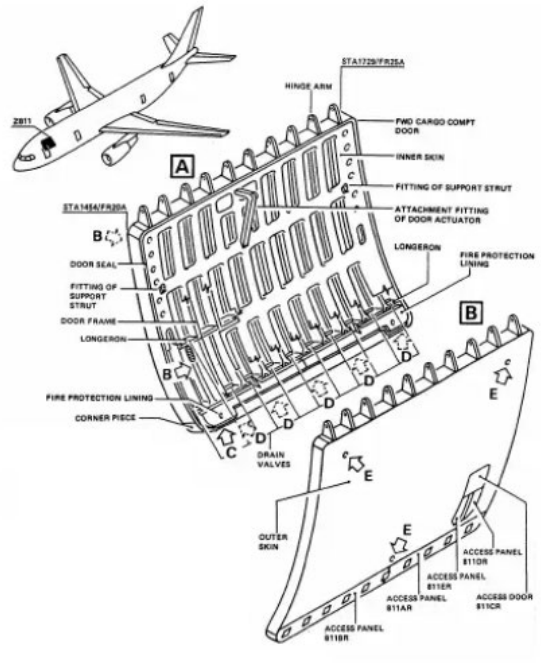

Figure 11. A300/310 Cargo Door (23)

The central problem addressed by this thesis is the lack of a robust and validated numerical methodology, and an associated design process, that can accurately predict damage initiation, propagation, and residual strength in a complex composite structure like the main cargo door. Addressing this gap will also contribute to a more efficient design process and support the validation methods required by evolving M&S regulations.

This defined problem forms the core aim of this research and sets the objectives that will guide the investigation and shape the outcome of this thesis.

1.3 Aims and Objectives

To address the central problem defined in the previous section, the following research aims and objectives have been defined in a sequential manner for clarity and ease of understanding.

The aim of this thesis is to develop and validate a robust numerical methodology, and an associated design process, that can accurately predict the damage initiation, propagation, and residual strength of a representative composite aircraft main cargo door.

To achieve the thesis aim, the following objectives will be met:

1. To conduct a comprehensive literature review of composite design philosophy, damage mechanics, relevant numerical simulation techniques (e.g., FEA, CZM), and the structural analysis of complex aircraft components.
2. To define and create a baseline geometric model of a representative composite aircraft main cargo door, including its key structural features (such as the skin, stiffeners, and curvature).
3. To develop a high-fidelity Finite Element (FE) model of the cargo door, including the selection and implementation of appropriate material models and failure criteria to simulate composite damage.
4. To perform a series of numerical simulations to analyse the damage progression and assess the residual strength of the aircraft main cargo door under defined structural compromising events, such as low-velocity impacts.
5. To validate the numerical methodology by comparing simulation results for a simplified case against published benchmark data or real-world experimental examples.
6. To critically analyse the final results, draw conclusions on the structural behaviour of the cargo door, and evaluate the effectiveness and validity of the developed modelling approach.

1.4 Scope and Limitations

This thesis is a computational investigation focused on the design and numerical analysis of a composite airframe structure. The research methodology is therefore scoped entirely to FEA, utilising Abaqus software. As such, the generation of new experimental data is, by design, outside the scope of this thesis. All validation and comparison will be based on data available in the public domain and existing literature.

The scope of the 3D CAD model is clearly defined. The model is a representative case study of the Airbus A350 Freighter (A350-F) main cargo door. As detailed manufacturer schematics are not shared, the geometry is developed based on an analysis of publicly available data, including technical specifications, photographs, and operational diagrams. The model is deliberately idealised for this FEA study, capturing the primary structural elements while excluding non-structural components (such as latching mechanisms or seals) that are not central to the structural response under impact.

The physics and analysis scope is defined to cover common operational hazards. The investigation is not limited to simple low-velocity impacts (e.g., a 'tool drop') but is extended to include higher-energy structural compromising events representative of ground service incidents. These scenarios include events such as cargo loader over-elevation or pallet misalignment impacts on the door structure. The subsequent analysis will focus on residual strength under quasi-static loads. High-velocity ballistic events, cyclic fatigue, and aeroelastic effects remain out of scope.

A primary limitation of this study is the lack of publicly available, identical experimental data for a direct, one-to-one validation of a full cargo door model. Therefore, the validation strategy is itself scoped to a 'weight of evidence' (WoE) approach. This methodology involves gathering information from a wide range of available sources to build confidence in the model. These sources will include, but are not limited to, published experimental data on similar composite structures (e.g., impacts on stiffened panels), public accident or incident reports from airworthiness bodies (EASA, FAA), and other relevant benchmark cases.

The goal is not to find an identical test to replicate, but to validate the model's methodology (e.g., failure criteria, contact definitions) and ensure the final results are credible when compared to documented real-world structural behaviour.

Finally, the research is subject to the following additional limitations:

1. Material Properties: The material properties used for the composite plies and interfaces are based on values from published literature and not from new, independent experimental characterisation.
2. Manufacturing Defects: The FE model assumes an ideal, defect-free structure. It does not account for potential manufacturing defects such as voids, porosity, or fibre waviness.
3. Joints and Fasteners: The connections between stiffeners and skin are idealised (e.g., as a "tie" constraint) and do not model the complex, non-linear physics of individual rivets or bolts.
4. Computational Cost: The fidelity of the simulation (e.g., mesh density) is constrained by the available computational resources.

1.5 Thesis Outline

Section 1 has established the background and motivation for this research. It has defined the specific problem of modelling complex composite airframes, outlined the core aims and objectives, and clarified the scope and limitations of the study.

Section 2 provides a critical literature review. It covers the fundamental principles of airframe structures, cargo door design philosophies, and the application of composite materials. It also investigates operational loads and impact risks relevant to cargo operations and the numerical methods used to model them, concluding with a summary of the identified research gap.

Section 3 details the conceptual and geometric design of the A350F cargo door. It outlines the key design requirements, details the proposed structural layout of the skin, stringers, and frames, and justifies the material selection, the generation of the final CAD model.

Section 4 details the development of the FE model. This covers the pre-processing, element selection, and meshing strategy, along with the modelling of the impact source, the setup of material and failure models, and the application of boundary conditions, loads, and solver parameters.

Section 5 presents the objective findings from the numerical simulations. It begins with the model verification, followed by a chronological analysis of the cargo impact scenario, presenting the objective data on damage propagation, structural deformation, and resulting stress patterns.

Section 6 provides an in-depth discussion of the results from the previous chapter. It features a detailed analysis of the failure mechanisms, an evaluation of the door's overall structural performance, and a critique of the modelling approach, concluding by exploring the implications for future design improvements.

Finally, Section 7 concludes the thesis. It summarises the key findings in relation to the original research aims, provides a final conclusion on the project's success, and offers specific, actionable recommendations for future research.

2 Literature Review

This section provides a critical review of the existing literature. It begins by establishing the fundamental principles of airframe structures and cargo door design, then investigates the specific challenges of composite materials and their operational impact risks. Finally, it reviews the current numerical methods used to model these events, thereby establishing the precise research gap this thesis will address.

2.1 Principles of Airframe Structures

The primary function of an airframe is to resist all aerodynamic, inertial, and ground loads while remaining both light and strong. The earliest structural type was the truss structure, still used today in many light aircraft. This was largely replaced by the monocoque design, a true eggshell where the skin carries all the loads. From this, the modern semi-monocoque structure evolved, which uses a thin skin reinforced by internal structural elements.

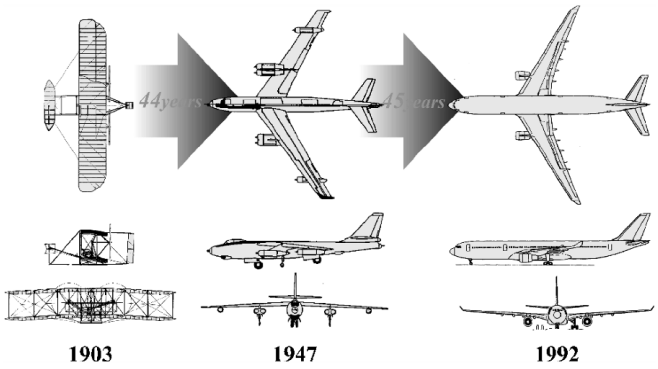

Figure 12. Aircraft Structural Design Evolution (24)

The internal framework of a semi-monocoque structure consists of longitudinal members (longerons and stringers) and transverse members (frames). These reinforcement elements stiffen the skin, increasing its ability to carry bending, shear, and torsional loads, while also allowing for a much more efficient load distribution. This superior ability to resist skin buckling and efficiently distribute loads is what makes the semi-monocoque design the preferred and far more efficient solution compared to the monocoque (25).

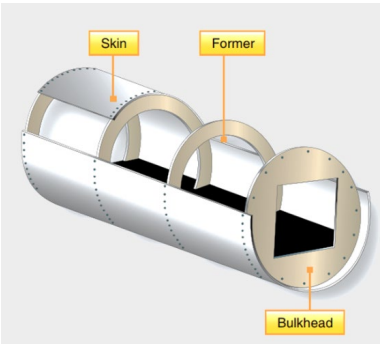

Figure 13. Monocoque Structure (26)

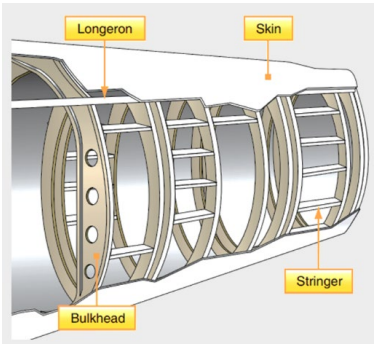

Figure 14. Semi-Monocoque Structure (26)

An aircraft fuselage is subjected to bending moments, shear forces, and torsional loads, which are resisted by stress-carrying structural members. The aircraft skin contributes to carrying shear stresses; this concept is known as the 'stressed skin'. It also resists the hoop stress caused by the pressurisation of the cabin (27).

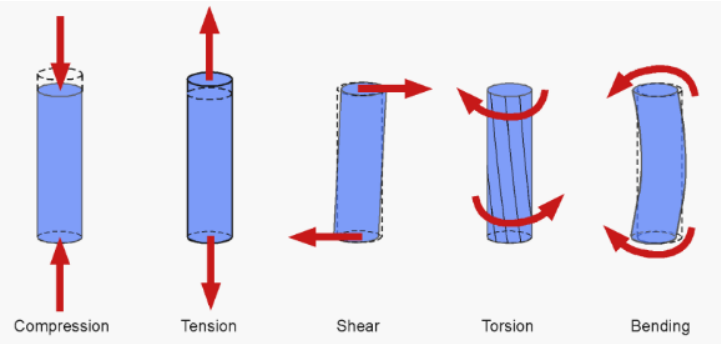

Figure 15. Stresses and Strains on an Aircraft Structure (25)

Cabin pressurisation causes both hoop stress and longitudinal stresses (tension and compression) on the fuselage skin. The fuselage design must account for these loads, considering all operational phases, including ground and in-flight conditions. A typical operational pressure differential for a civil passenger aircraft is around 8.77 psi (maintaining an 8,000 ft. cabin altitude). However, the structure must be designed to withstand the maximum pressure differential to ensure safety, which can be much higher (28).

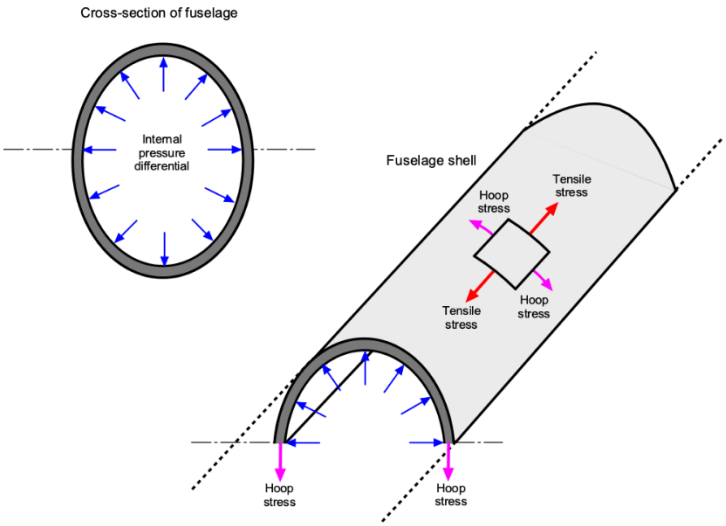

Figure 16. Cabin Pressurisation Induced Hoop and Tensile Stress (25)

Furthermore, the fuselage is subjected to significant bending moments induced by the tail, alongside torsional loads originating from the vertical fin and rudder. As these forces present a considerable risk of skin buckling, the outer skin is reinforced by internal structural elements, specifically the frames and stringers, which ensure the efficient distribution of stress. The transverse frames serve the critical function of maintaining the cross-sectional geometry of the fuselage. Simultaneously, the longitudinal stringers and longerons provide the necessary structural stiffness to withstand primary torsion and bending loads, thereby managing the associated axial tension and compression while acting as a reinforcement against local skin instability (29,30).

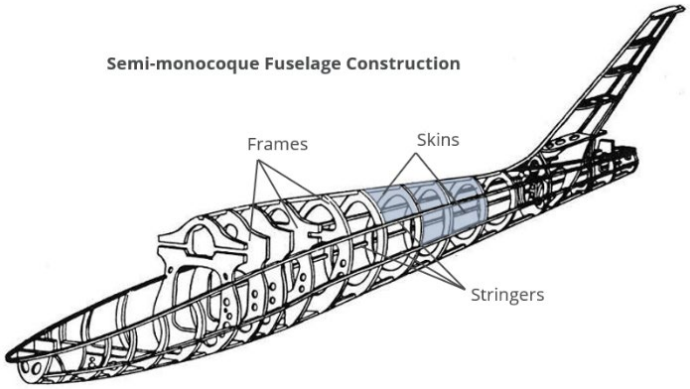

Figure 17. Fuselage Structural Elements (31)

Continuity of strength and resistance against these loads and stresses are disrupted by cut-outs on the fuselage such as windows and doors. For a freighter aircraft, the main cargo door is a major cut-out where huge stress concentration zones appear around the corners which requires attention for load re-distribution in these areas (32).

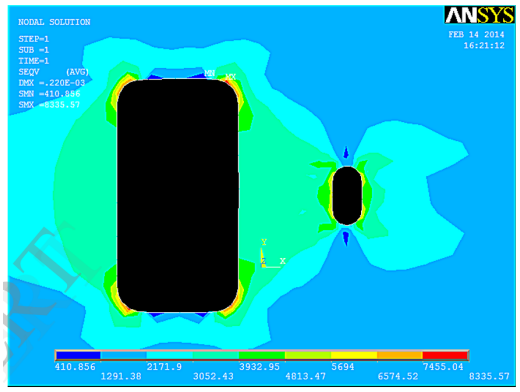

Figure 18. Stress Concentration around Door and Window (33)

The redistribution of concentrated internal pressure and flight loads is achieved through reinforcements surrounding the door cutout, known as the door-surround-structure (DSS). This structure typically comprises additional doubler plates applied to the fuselage skin in corner regions, sills, intercostals, and auxiliary frames as required (32).

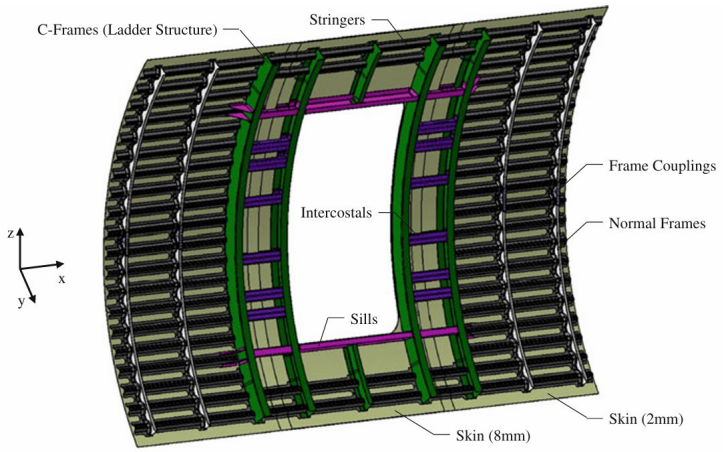

Figure 19. Example of a Door-Surround-Structure with High Stress Areas (34)

Cargo door design isn't constrained by the same airworthiness rules that apply to cabin doors; the main engineering constraint is simply the physical size of the intended cargo. To solve the challenge of loading large high-bypass aero engines onto the A350F, a massive outward-opening door was necessary. Engineers utilised a 4.5-meter wide cutout to create a usable 4.3-meter opening, resulting in a door that is 15% wider than its competitor on the Boeing 777 Freighter (35).

Figure 20. A350- Freighter Cargo Door (35)

2.2 Aircraft Cargo Door Design Philosophy

The primary purpose of a cargo door is to facilitate the efficient loading and unloading of freight onto an aircraft. While various operational mechanisms exist, large fuselage-mounted cargo doors generally employ an outward-opening configuration. This design choice is primarily dictated by internal volume constraints that preclude inward operation, as well as the necessity to provide unobstructed access to the main deck, thereby enhancing the overall efficiency of cargo handling processes. This configuration and its implementation on the Airbus A330-200F are provided in Figures 21 and 22.

Figure 21. A330-200F Cargo Loading Operation (36)

Figure 22. A330-200F Cargo Door Inside View (37)

To mitigate the primary structural challenges of weight penalties arising from stress concentrations, advanced materials such as CFRP are increasingly utilised. The superior strength to weight ratio of these composites compared to traditional metallic alloys makes them the optimal material choice for high load applications, as they facilitate significant mass reductions while simultaneously enhancing structural integrity. While aluminium alloys have historically been the standard for door structures, these performance advantages have led Airbus to confirm that the main deck cargo door for the new A350 Freighter will be constructed from composite materials to ensure adherence to stringent safety and operational standards (38,39).

The structural architecture of a cargo door is fundamentally composed of an outer skin, an inner skin, and an internal framework comprising transverse frames and longerons. In addition to these primary load-bearing elements, the assembly incorporates critical mechanical interfaces necessary for airframe integration, including the piano hinge and various hoist points and actuation systems. A visual representation of this structural and mechanical arrangement as implemented on the Boeing 777 Freighter is provided in Figure 23, although it should be noted that this particular airframe primarily utilises traditional aluminium alloys for these components (40).

Figure 23. B777-Freighter Main Deck Cargo Door (41)

Technological advancements and the rising demand for materials with bespoke mechanical properties have driven the aerospace industry towards the widespread adoption of composite applications. The inherent tailorability of these materials allows for the precise engineering of structural characteristics through the manipulation of fibre reinforcement architectures, constituent volume fractions, and lamination sequences. Consequently, this versatility has facilitated a transition from traditional aluminium alloys to composite structures for critical components, such as cargo doors, where material properties can be optimised to meet specific operational requirements (42).

Within the commercial aviation sector, a primary precedent for the implementation of composite cargo doors is established by the Boeing 787 Dreamliner, with the structural assembly manufactured and supplied by Saab. This implementation serves as a significant case study for the integration of advanced materials into large-scale fuselage apertures, demonstrating the transition away from traditional metallic constructions in modern wide-body aircraft.

Figure 24. B787 Dreamliner Composite Cargo Door (43)

Although standard fuselage design is well documented, the use of composites for large cargo doors lacks extensive public research. Most existing designs are company know-how and based on the specific expertise of individual manufacturers rather than industry-wide standards. Another application is the composite passenger door on the Airbus A350, which is illustrated in Figure 25.

Figure 25. A350 Composite Passenger Door (44)

2.3 Composite Materials in Aerospace Structures

The aerospace industry's pursuit of reduced structural mass and increased fuel efficiency has driven a definitive transition from isotropic metallic alloys to carbon fibre reinforced polymers (CFRP). As detailed in the comprehensive global review by Zhang et al., this shift is best exemplified by the latest generation of wide-body aircraft. The Boeing 787 and Airbus A350 XWB now incorporate approximately 50% and 53% CFRP by weight in their primary structures, respectively (45).

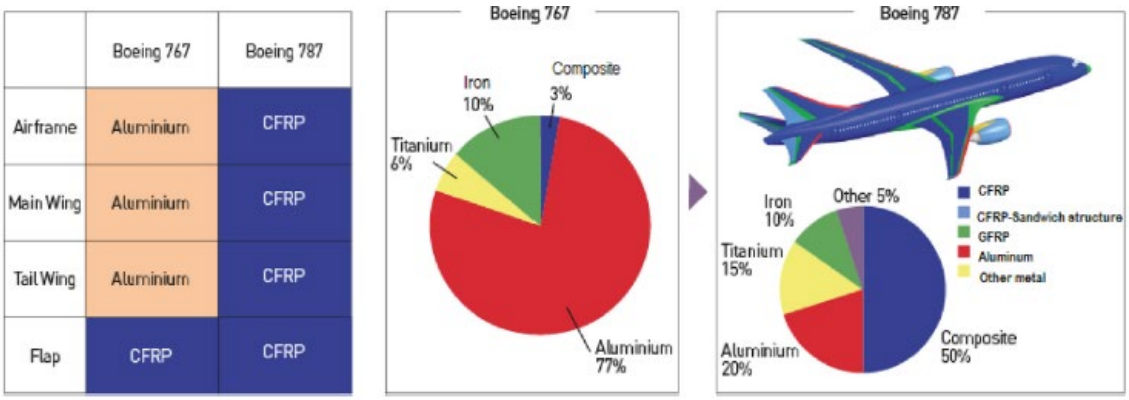

Figure 26. Comparison of materials use in Boeing 767 and Boeing 787 (45)

This represents a paradigm shift from previous generations, such as the Boeing 777 (12% composite) or Airbus A380 (25%), where composites were largely restricted to secondary structures. The primary driver for this adoption is the superior specific strength and modulus of carbon fibre, which allows for lighter airframes that directly correlate to reduced fuel consumption and CO_2 emissions.

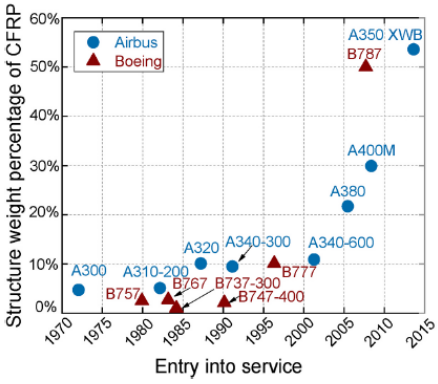

Figure 27. CFRP Usage over Time in Airbus and Boeing Aircraft (45)

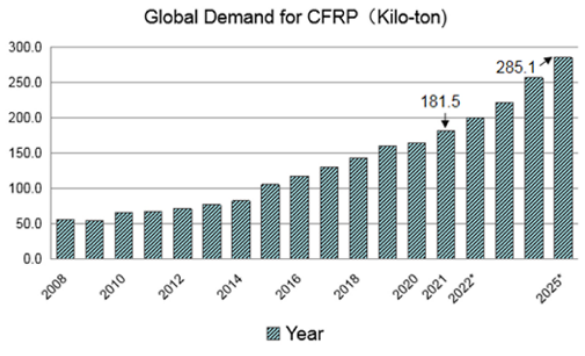

Figure 28. Global Demand for CFRP Composites Over Time (45)

However, the application of CFRP in primary fuselage structures, such as the Main Deck Cargo Door, necessitates a fundamental change in structural design philosophy. While honeycomb sandwich panels have historically been favoured for their high stiffness-to-weight ratio in control surfaces, the industry has moved towards monolithic stiffened structures for primary fuselage sections. In this configuration, often referred to as "Black Metal," a relatively thin solid laminate skin is reinforced by co-bonded or co-cured longitudinal stringers and circumferential frames (46).

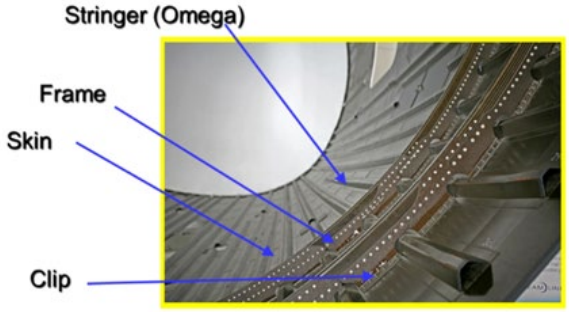

Figure 29. B787 Fuselage Section (46)

Figure 30. B787 One-shot Nose Section (46)

This architecture is preferred over sandwich panels for large fuselage sections due to superior damage tolerance and the ability to operate safely in the post-buckling regime. As illustrated by the comparative analysis in Castanié et al., a stiffened cylinder design can achieve mass savings of up to 42% compared to an equivalent aluminium structure by allowing the skin to buckle elastically between stiffeners while the stringers carry the primary compressive load. This capability is notably absent in sandwich panels due to the risk of core crushing and face-sheet disbanding (46).

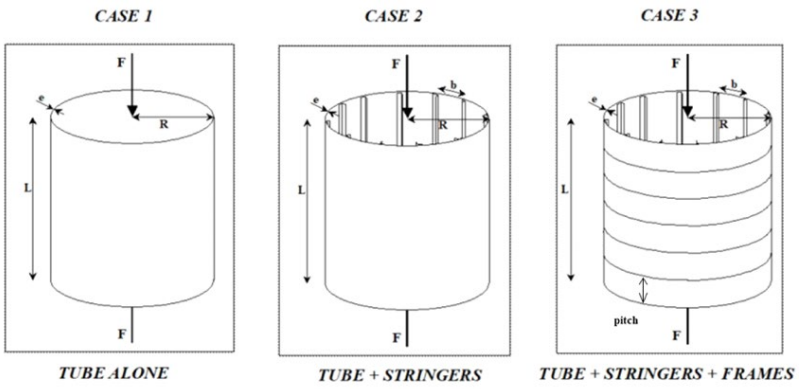

Figure 31. Example of Tube in Compression with and without Post Buckling (46)

Unlike isotropic metals, the mechanical performance of these monolithic laminates is strictly governed by the anisotropy of the ply stacking sequence. A recent numerical investigation by Patel et al. critically assessed the impact damage resistance of various CFRP laminate configurations, including unidirectional $[0]_8$, cross-ply $[0/90]_{2s}$, and quasi-isotropic $[0/+45/-45/90]_s$ layouts. Their findings conclusively demonstrated that the quasi-isotropic configuration offers superior impact resistance (47).

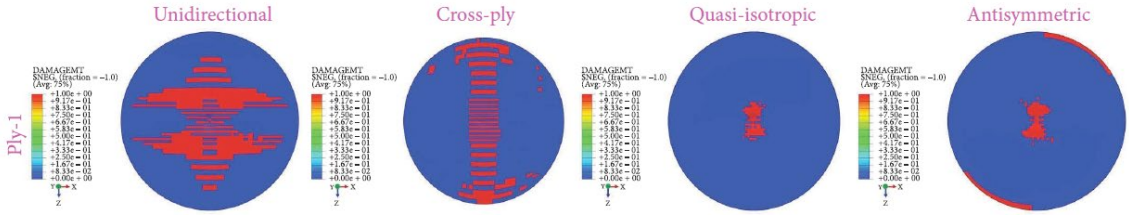

Figure 32. Matrix Tensile Failure (DAMAGEMT) and CFRP Laminate Configurations (47)

As presented in their impact response data, the quasi-isotropic laminate exhibited the highest peak impact-resisting force and the lowest peak displacement compared to other orientations. Specifically, under a $7.35\ J$ impact, the quasi-isotropic layup demonstrated a peak force of $3.5\ kN$, significantly higher than the $2.8\ kN$ observed for the unidirectional sample. This indicates that the multidirectional fibre distribution facilitates a more uniform stress distribution, thereby minimising the extent of intralaminar matrix cracking and delamination under low-velocity impact events. This finding justifies the industry-standard practice of utilising balanced, multidirectional stacking sequences for fuselage skins exposed to operational impact risks.

	Impact energy (J)	Unidirectional	Cross-ply	Quasi-isotropic	Antisymmetric
Peak impact-resisting force	7.35	2.8 kN	3.5 kN	5.2 kN	5.1 kN
	11.03	3.3 kN	4.3 kN	6.4 kN	6.1 kN
	14.70	3.9 kN	4.7 kN	6.7 kN	6.2 kN
Peak displacement	7.35	4.8 mm	4.3 mm	3.6 mm	3.7 mm
	11.03	5.9 mm	5.1 mm	4.2 mm	4.4 mm
	14.70	6.9 mm	5.7 mm	4.9 mm	5.1 mm
Residual displacement	7.35	0.69 mm	0.79 mm	0.56 mm	0.67 mm
	11.03	0.43 mm	1.37 mm	0.61 mm	0.79 mm
	14.70	0.45 mm	1.59 mm	0.63 mm	0.94 mm

Table 2.1 From Patel et al. (47) Peak impact-resisting force, peak displacement, and residual displacement

Despite these in-plane advantages, laminated composites remain inherently vulnerable in the through-thickness (z) direction due to the lack of fibre reinforcement across the ply interfaces. This weakness makes them susceptible to delamination, where the interlaminar shear stresses generated by an impact exceed the strength of the polymer matrix. While through-thickness reinforcement (TTR) techniques such as Z-pinning have been proposed to arrest this delamination, recent experimental work by Chen et al. suggests that these reinforcements may be detrimental to damage initiation strength (48).

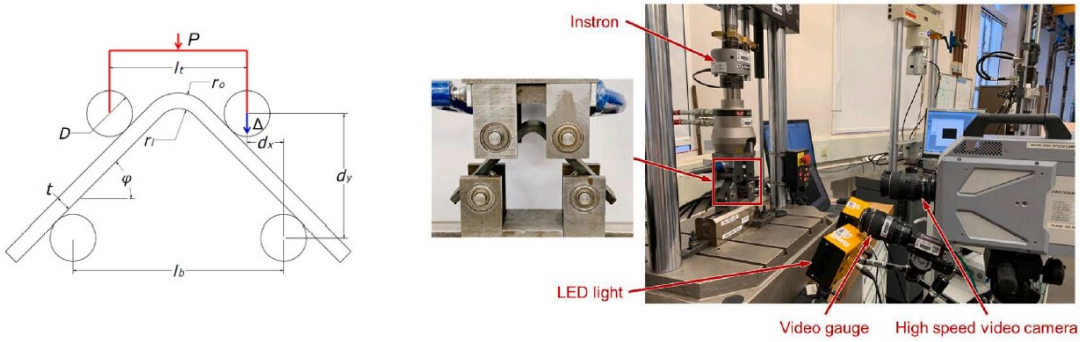

Figure 33. Chen et al. Experimental Test Set-Up Overview (48)

In their study on curved carbon/epoxy laminates, Chen et al. found that the insertion of Z-pins reduced the through-thickness tensile strength (TTS) by up to 38% compared to unpinned samples. The study correlates these findings with three different factors (48).

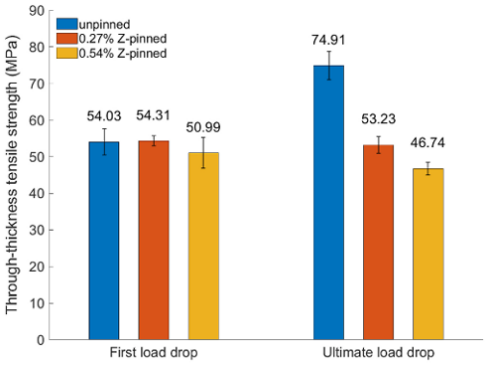

Figure 34. Tensile Thickness in Z direction for Unpinned and Z-Pinned Specimen (48)

Sample ID	Unpinned		0.27 % Z-pinned		0.54 % Z-pinned	
	First TTS (MPa)	Ultimate TTS (MPa)	First TTS (MPa)	Ultimate TTS (MPa)	First TTS (MPa)	Ultimate TTS (MPa)
1	–	61.65	–	55.96	–	41.90
2	46.94	73.57	51.17	56.92	46.78	43.96
3	–	76.78	57.62	49.39	55.20	48.62
4	58.00	76.93	55.09	46.29	–	51.41
5	57.16	85.60	53.36	57.59	–	47.81
Mean	**54.03**	**74.91**	**54.31**	**53.23**	**50.99**	**46.74**
C.V.	11.4 %	11.6 %	5.0 %	9.5 %	11.7 %	8.1 %

Table 2.2 Experimental Results for TTS for Unpinned and Z-Pinned Specimen (48)

They attributed this reduction to significant residual tensile stresses generated around the pins during the post-cure cool-down phase, as well as microstructural defects like resin pockets and fibre waviness induced by the pin insertion (48).

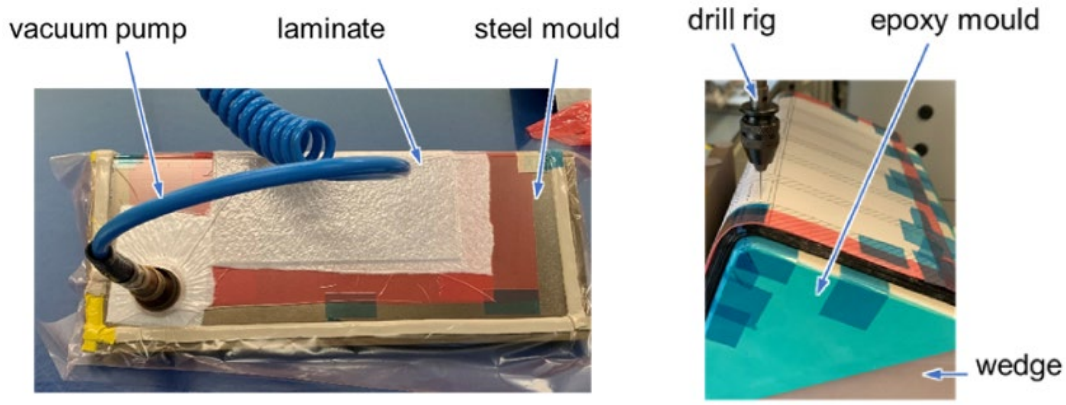

Figure 35. Cen et al. Study Specimen Manufacturing and Preparation (48)

The stress maps generated by their finite element analysis reveal a high concentration of residual tensile stress in the immediate vicinity of the pin, acting as a precursor for early delamination onset. Consequently, most certified civil aircraft structures, including the cargo door assembly modelled in this thesis, rely on standard unpinned laminates. This design choice prioritises high initiation strength but leaves the structure susceptible to BVID. In this scenario, low-energy impacts can induce extensive subsurface delamination without visual surface indications, a phenomenon that underscores the critical need for accurate damage prediction models (48).

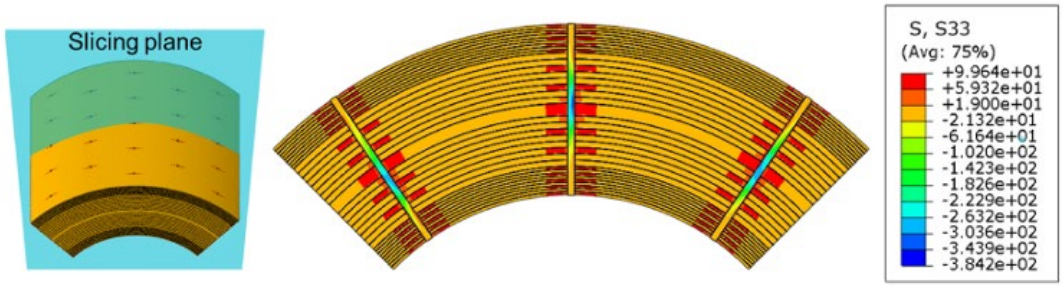

Figure 36. FEA Analysis Normal Stress Results for Z-Pinned Specimen Stress Results after Cool-Down (48)

2.4 Operational Loads and Impact Risks

While the aerodynamic and pressurisation loads defined in Section 2.1 dictate the primary sizing of the airframe for flight, the operational environment introduces a distinct spectrum of mechanical threats that occur exclusively on the ground. For a freighter aircraft, the main deck cargo door (MDCD) operates in a high-density industrial environment known as the "ramp" or "apron". This zone is characterised by the close proximity of heavy ground support equipment (GSE) to the aircraft fuselage. Unlike the flight phase, where risks are aerodynamic, the primary threat on the ground is the physical collision between service vehicles and the composite airframe, a phenomenon widely referred to in the industry as "ramp rash".

2.4.1 The Ground Support Environment

The complexity of aircraft turnaround operations necessitates the simultaneous interaction of multiple vehicle types. A comprehensive review by Zhou et al. (49) identifies the specific fleet of GSE required for servicing, which includes ferry vehicles, baggage trains, refuelling trucks, and, most critically for this study, catering and cargo high-loaders. The operation of these vehicles is highly interdependent and constrained by limited space and strict time windows.

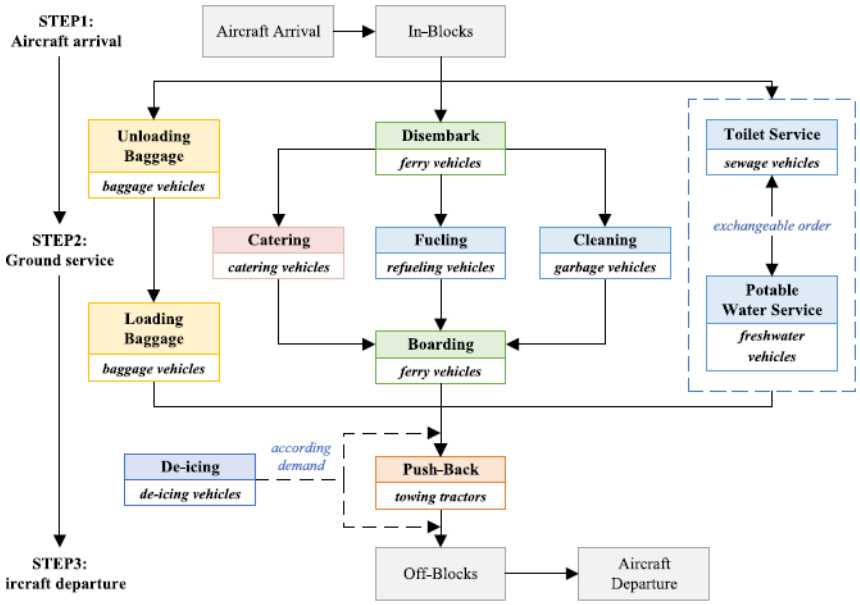

Figure 37. Ground Handling Services Sequence for a Flight Operation (49)

Statistical analysis confirms that this congestion directly correlates with damage frequency. In a safety investigation of ground handling, Balk [6] analysed over 2,800 incidents and determined that the vast majority (84% to 92%) of ground damage occurs while the aircraft is "Standing" (stationary at the gate). Crucially, Balk found that 61% of these incidents occur specifically when an interface is established between the aircraft and the ground equipment. For a cargo door, this is the moment the high-loader docks with the fuselage. The analysis identified that damage is most frequently inflicted by actors attaching vehicles to passenger or cargo doors, identifying a clear operational risk at the specific location modelled in this thesis (50).

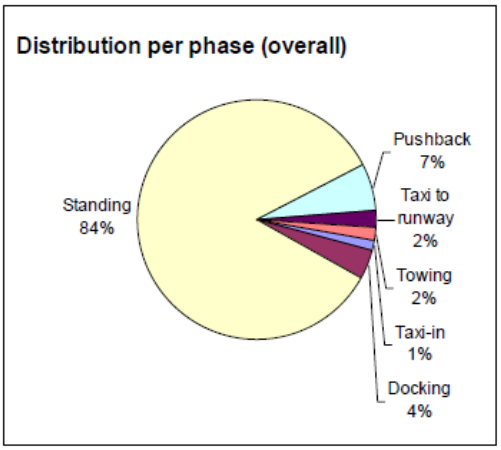

Figure 38. Ground Damage Distribution Per Phase (50)

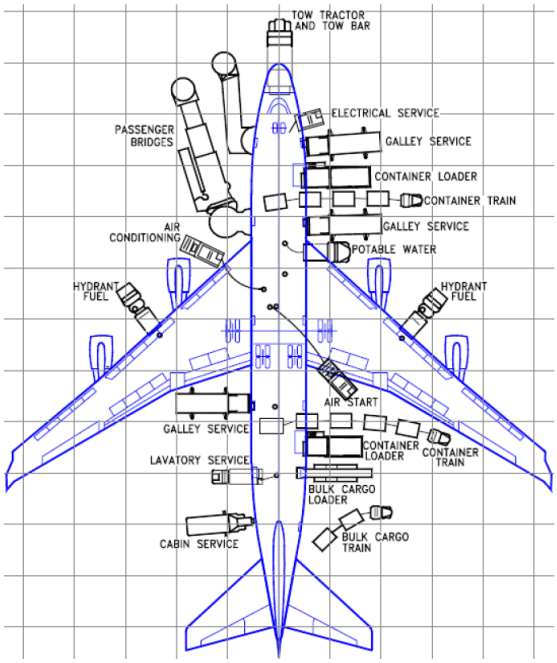

Figure 39. Typical Ground Support Service and Handling Operations around an Aircraft (50)

2.4.2 Low-Velocity Impact Physics and BVID

The collisions described above are categorised as low-velocity impacts (LVI). It is vital to distinguish LVI from high-velocity ballistic events such as bird strikes or runway debris. Caminero et al. (51) define LVI not by speed (typically <$10\ ms^{-1}$) but by the structural response. In LVI events, the contact duration is sufficiently long for the entire structure to respond quasi-statically, absorbing energy through global bending and local indentation rather than immediate perforation. However, because ground service vehicles possess significant mass, even low-speed collisions involve substantial kinetic energy, often ranging from $20\ J$ to over $50\ J$.

The most insidious consequence of LVI on composite structures is the phenomenon of BVID. Unlike ductile aluminium, which exhibits a clear plastic dent at the impact site, CFRP laminates often deform elastically and recover their surface profile, leaving little to no visual indication of the event. However, as demonstrated by Caminero et al. (51) through phased array ultrasonic testing, this surface recovery masks extensive internal damage. Their experiments on carbon/epoxy laminates subjected to $20\ J$ and $30\ J$ impacts revealed large delamination areas and matrix cracking at the ply interfaces, despite the surface indentation being minimal.

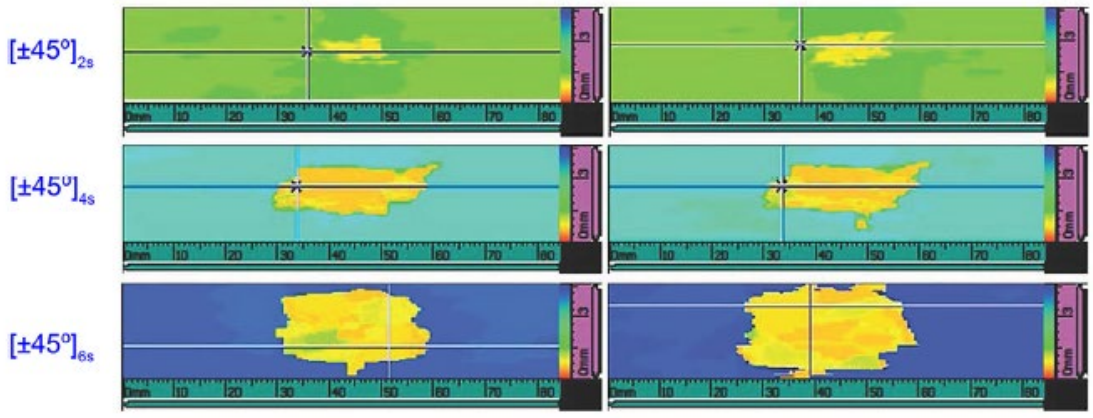

Figure 40. Ultrasonic Phased Array C-Scan Results for $20\ J$ and $30\ J$ Impact (51)

2.4.3 The “Latent Defect” and Detection Challenges

This "invisible" damage morphology creates a critical safety risk known as a "latent defect." A cargo door may sustain a $20\ J$ impact from a loader bump during turnaround, visually pass the pre-flight walk-around inspection, and then be cleared for flight. However, as the aircraft climbs and the fuselage pressurises, the internal delamination acts as a stress concentration point, potentially propagating under the hoop stress described in Section 2.1.

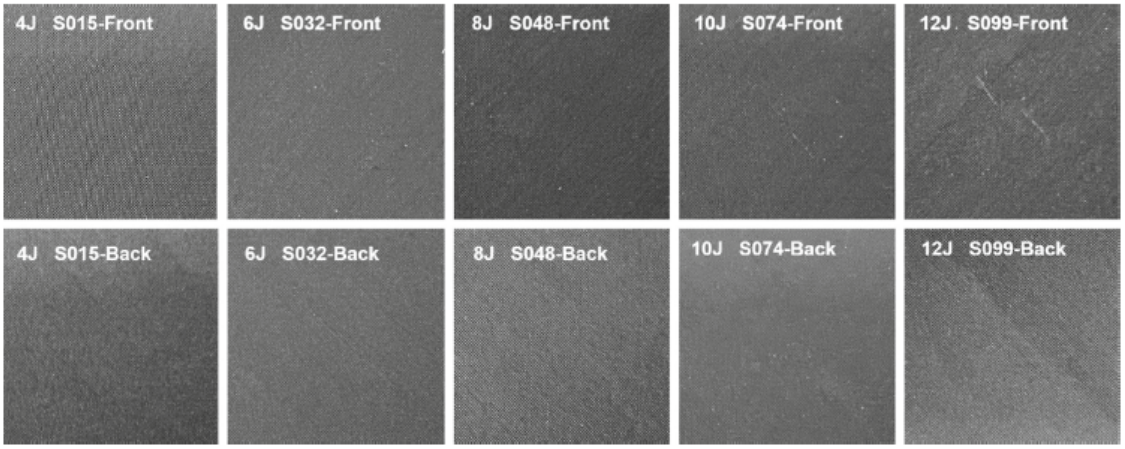

Figure 41. Camera Images of Damaged Specimens with Various Range of Impact Energy Levels (52)

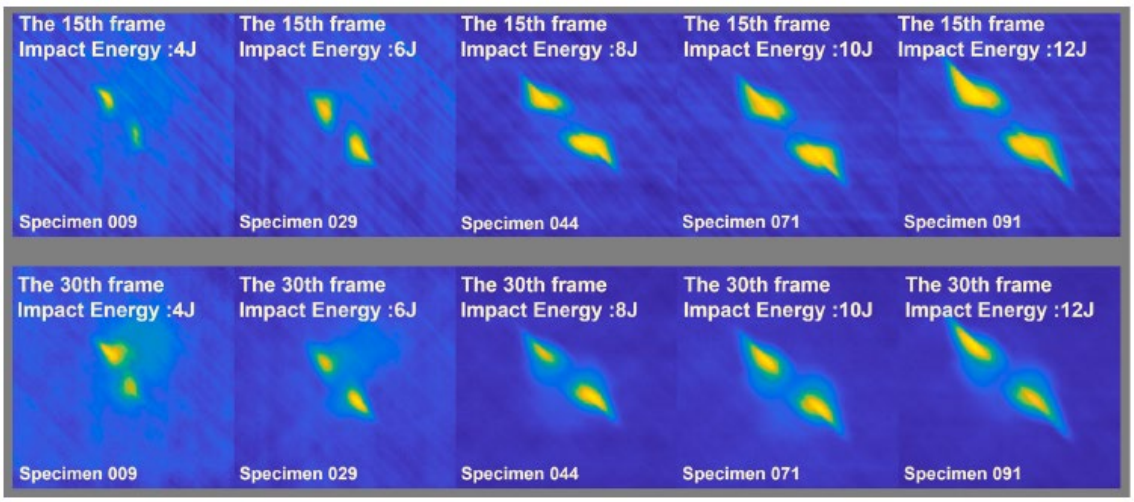

Figure 42. Thermal Images of Damaged Specimens with Various Range of Impact Energy Levels

Detecting this damage requires advanced non-destructive testing (NDT) rather than simple visual checks. Katunin et al. (53) highlighted that standard visual inspections are insufficient for BVID and that even ultrasonic testing (UT) can misestimate the true extent of damage if not calibrated correctly. Their fusion of UT and X-ray computed tomography (CT) data revealed that internal fracture networks are often far more complex than 2D scans suggest.

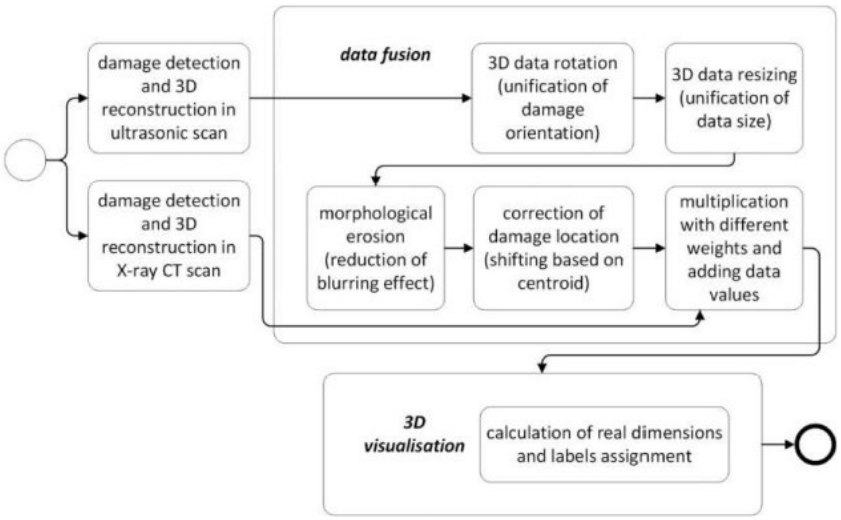

Figure 43. Damage Detection Algorithm Framework with C-Scans with X-ray CT- scans (53)

Similarly, Deng et al. (52) proposed deep learning frameworks using pulsed thermography to classify these invisible defects, proving that distinguishing between a harmless $4\,J$ bump and a critical $12\,J$ delamination requires sophisticated thermal analysis that is rarely available on the ramp during a rapid turnaround.

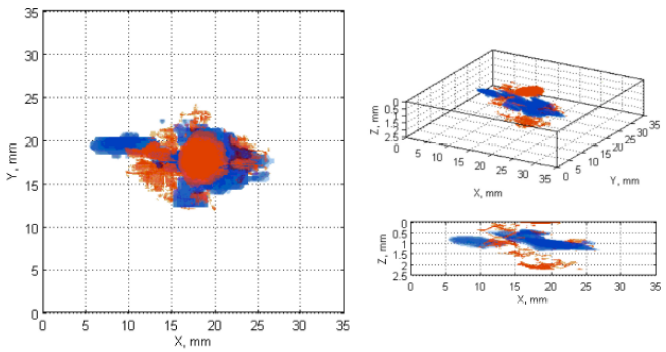

Figure 44. X-Ray CT scan (red colour) and Ultrasonic Results (blue colour) for a Specimen Impacted with $17.5\,J$ Energy (53)

2.5 Numerical Modelling of impact Events

The prohibitive cost and complexity of full-scale physical testing have driven the aerospace industry towards a "certification by analysis" approach. As highlighted by the validation studies of Bergan (54) at NASA, high-fidelity FEA is now a primary tool for predicting progressive damage analysis (PDA) in composite structures. However, accurate modelling of low velocity impact (LVI) requires a specific combination of solver strategies, failure criteria, and damage evolution laws to capture the complex interaction between intralaminar fracture and interlaminar delamination (54).

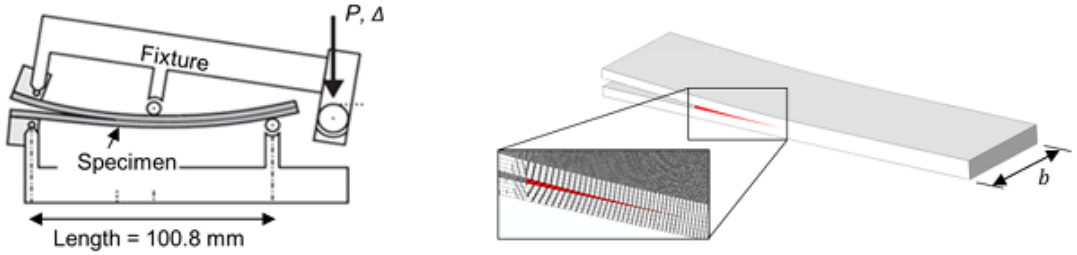

Figure 45. Experimental and FEA Model Test Specimen Overview Schematic (54)

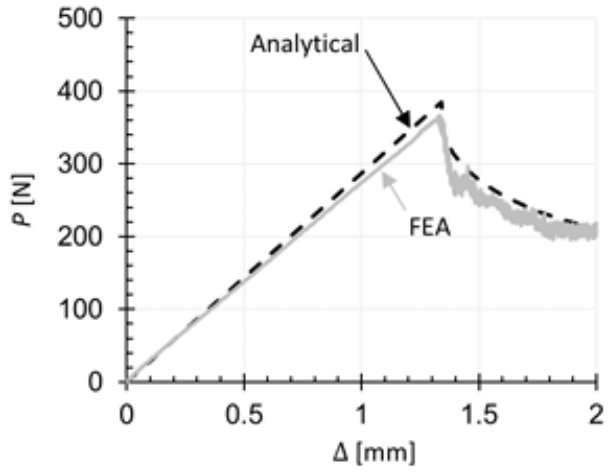

Figure 46. Comparison of Experimental and FEA Test (54)

2.5.1 Explicit Dynamic Solvers

The simulation of impact events typically necessitates the use of an explicit dynamic solver rather than a standard implicit solver. While implicit methods are unconditionally stable and suitable for static loading, they struggle with the highly discontinuous nature of impact events where contact conditions change rapidly, and material stiffness degrades instantaneously upon failure. Bergan (54) demonstrates that explicit solvers, which use the central difference integration rule to advance the kinematic state of the model, are computationally more efficient for wave propagation problems. The stability of these solvers is governed by the critical stable time, which requires extremely small-time increments determined by the smallest element dimension and the speed of sound in the material (55).

$$\Delta T \leq \Delta T_C = (T_{min}/\pi) = (2/\omega_{max}) \quad \textbf{(2.1)}$$

$$N = T/\Delta T \quad \textbf{(2.2)}$$

$$\Delta T_C \approx (L_{min}/C_d) \quad \textbf{(2.3)}$$

To mitigate the computational cost of these small-time increments, mass scaling is frequently employed. This technique artificially increases the density of the smallest elements to increase the stable time increment. Gattmah et al. (55) investigated the effects of mass scaling on explicit simulations and established a critical validity criterion. The technique is considered acceptable provided that the artificial increase in mass does not introduce significant dynamic artefacts. Specifically, the ratio of kinetic energy to internal energy must remain below 5% throughout the quasi-static phase of the analysis to ensure the solution remains physically representative.

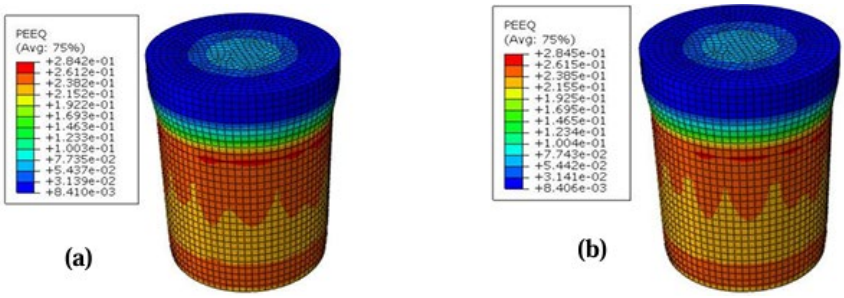

Figure 47. Equivalent Plastic Strain (PEEQ) Results for Specimen (a) without Scaling and (b) with Scaling (55)

2.5.2 Intralaminar Failure: Hashin's Criteria

Modelling the failure of the composite ply itself (intralaminar damage) requires a failure theory that can distinguish between failure modes. Xu et al. (56) highlight that while simple criteria like maximum stress are useful for initial sizing, they fail to identify the specific failure mechanism (e.g., fibre tension vs. matrix compression). Consequently, the Hashin failure criteria has become the industry standard for unidirectional laminates. Hashin's model separates damage initiation into four distinct modes:

1. Fibre tension: Rupture of the carbon fibres.
2. Fibre compression: Buckling or kinking of fibres.
3. Matrix tension: Cracking of the resin matrix.
4. Matrix compression: Crushing of the matrix.

Once initiation occurs, the material stiffness is degraded according to a damage evolution law. Xu et al. (56) utilised a linear degradation scheme where the element stiffness is progressively reduced to zero, simulating the loss of load-carrying capacity

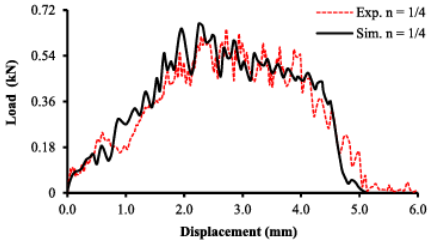

Figure 48. Experimental vs FEA Simulation Load-Displacement Curve Comparison (56)

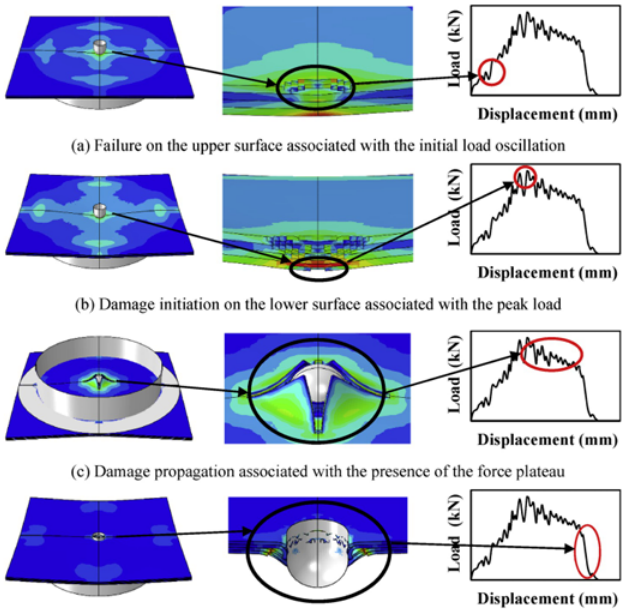

Figure 49. Impact Simulation Phase Comparison with Load-Displacement Curve (56)

2.5.3 Interlaminar Failure: Cohesive Zone Modelling

The most critical failure mode in low-velocity impact of laminated composites is delamination, the separation of plies. Standard continuum elements cannot simulate this decohesion naturally. To address this, cohesive zone modelling is employed at the ply interfaces. As detailed by Xu et al. [10], this utilises a bilinear traction-separation law (see Table 2.3).

- Elastic stage: The interface acts as a stiff spring, holding plies together.
- Damage initiation: Once the interlaminar traction stress exceeds the interfacial strength (quadratic nominal stress criterion), damage initiates.
- Damage evolution: The traction reduces linearly as the separation increases.
- Failure: When the area under the curve (interlaminar fracture energy, G_c) is exhausted, the element is deleted, and the plies separate.

Elasticity Matrix to Traction Separation Constitutive Behaviour (56)	$\mathbf{t} = \begin{Bmatrix} \mathbf{t_n} \\ \mathbf{t_s} \\ \mathbf{t_t} \end{Bmatrix} = \begin{bmatrix} \mathbf{K_{nn}} & \mathbf{K_{ns}} & \mathbf{K_{nt}} \\ \mathbf{K_{ns}} & \mathbf{K_{ss}} & \mathbf{K_{st}} \\ \mathbf{K_{nt}} & \mathbf{K_{st}} & \mathbf{K_{tt}} \end{bmatrix} \begin{Bmatrix} \boldsymbol{\delta}_\mathbf{n} \\ \boldsymbol{\delta}_\mathbf{s} \\ \boldsymbol{\delta}_\mathbf{t} \end{Bmatrix} = \mathbf{K}\boldsymbol{\delta}$	*(2.4)*
Quadratic Criterion in terms of Onset of Delamination (56)	$f_d = \left(\frac{\langle t_n \rangle}{N}\right)^2 \left(\frac{t_s}{S}\right)^2 \left(\frac{t_t}{T}\right)^2$	*(2.5)*
Linear Degradation of the Elasticity Matrix in Mixed-Mode Delamination (56)	$K_d = DK\ D = \frac{\delta_m^f(\delta_m^{max} - \delta_m^o)}{\delta_m^{max}(\delta_m^f - \delta_m^o)}$	*(2.6)*

Table 2.3 Cohesive Interface Modelling, Bilinear Traction-Separation Model in Abaqus

2.5.4 Element Deletion and Mesh Sensitivity

To simulate physical penetration or hole formation, finite element models typically employ element deletion. Elements are removed from the mesh when their damage variable reaches a critical value (typically $D = 1.0$). While effective for visualising puncture, Bergan (54) notes that this method is inherently mesh-dependent; the energy dissipated during fracture becomes a function of element size.

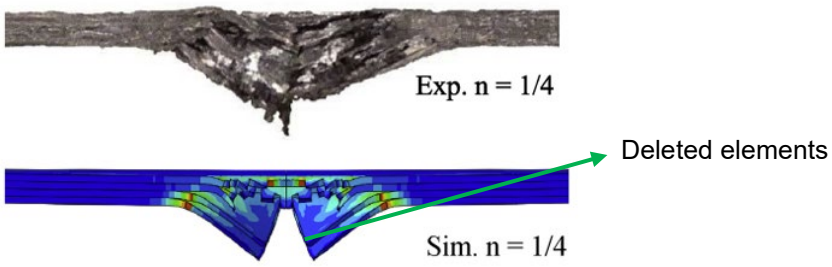

Figure 50. Experimental and FEA Comparison of Impact Damage (56)

Therefore, establishing a consistent mesh density in the impact zone is critical. Xu et al. (56) addressed this by implementing a **graded mesh strategy** (see Figure 51), utilising a high-density mesh ($0.5\ x\ 0.5\ mm$) exclusively in the central impact zone to capture high-gradient damage evolution, while transitioning to a coarser mesh in the far-field to maintain computational efficiency.

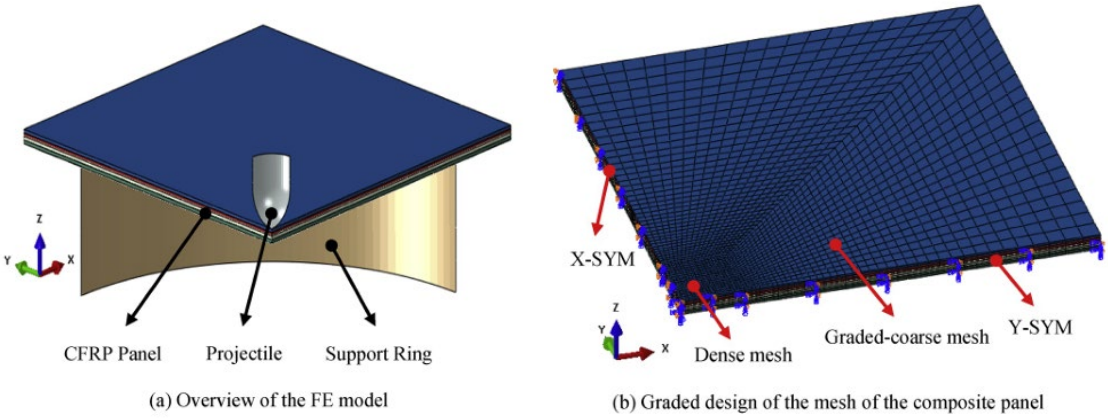

(a) Overview of the FE model

(b) Graded design of the mesh of the composite panel

Figure 51. Low-Velocity Impact FEA Model with Graded Mesh Strategy (56)

2.6 Summary and Research Gap

The aerospace industry is decisively transitioning to monolithic carbon fibre reinforced polymer (CFRP) structures to meet mass reduction and fatigue resistance targets (45,46). However, this material shift creates a critical vulnerability to low-velocity impact events during ground handling operations. As identified by Zhou et al. (49) and Balk (50), the interaction between ground support equipment and the airframe is a statistically significant threat. Unlike metallic structures, CFRP is prone to BVID. Extensive internal delamination can occur with minimal surface indication in this state (51,53). The difficulty in detecting these latent defects necessitates a damage tolerance design philosophy.

To address these challenges without the costs of full-scale testing, numerical modelling has become an essential certification tool. The literature confirms that explicit dynamic solvers, such as Abaqus/Explicit, are the industry standard for capturing transient impact forces (54). Furthermore, combining Hashin's failure criteria for intralaminar damage with Cohesive Zone Modelling (CZM) for interlaminar delamination is a validated methodology for predicting failure onset (56).

A distinct gap remains in the current body of knowledge. Most numerical studies focus on simple academic coupons or small-scale element tests rather than complex industrial assemblies (47,48). Research applying these high-fidelity damage models to the structural coupling between a curved fuselage skin and bonded stiffeners is limited. Consequently, this thesis addresses this gap by developing a multi-scale finite element model of the A350F Main Deck Cargo Door. This research applies validated explicit dynamics and cohesive zone modelling to quantify BVID thresholds and failure mechanisms that simplified.

3 Cargo Door Conceptual Design and Geometric Modelling

This chapter details the geometric definition, structural sizing and computer-aided design (CAD) generation of the main deck cargo door (MDCD) for the Airbus A350F platform.

While the preceding literature review established the theoretical vulnerability of composite airframes to ground impact, this section translates those findings into a physical design baseline. It outlines the specific operational requirements, the selection of a monolithic semi-monocoque architecture and the precise geometric parameters used to construct the high-fidelity 3D model in CATIA V5.

3.1 Design Requirements and Specifications

The structural definition of the MDCD is governed by a strict set of geometric and operational constraints derived from the Airbus A350F mission profile. The primary commercial driver is the capability to load modern high-bypass turbofan engines and ISO standard shipping pallets, necessitating a large, unobstructed opening.

Figure 52. A350 Freighter Cargo Door Mock-Up Display (57)

To satisfy these operational needs while ensuring structural integrity, the conceptual design was developed against the following key requirements specification (35):

1. **Geometric Constraints**

- **Fuselage Profile:** The door surface must match the constant fuselage cross-section diameter of **5.96 metres** to ensure aerodynamic continuity and correct hoop stress distribution under pressurisation.
- **Clear Opening:** A clear opening width of **4.3 metres** is required to accommodate large cargo payloads.
- **Structural Cutout:** To achieve the operational clearance, a structural cutout of **4.5 metres** is required in the fuselage skin.

2. Structural Architecture and Configuration

- **Semi-Monocoque Construction:** The assembly shall utilise a "Black Metal" semi-monocoque philosophy, replacing traditional aluminium panels with a fully composite architecture.
- **Primary Skin:** A monolithic CFRP skin shall act as the primary pressure vessel and aerodynamic surface.
- **Longitudinal Stiffening:** Buckling resistance must be provided by a grid of longitudinal stringers utilizing a closed Omega (Ω) profile to maximise torsional stiffness and bonding area.
- **Circumferential Stiffening:** The assembly must incorporate circumferential **C-frames** to maintain fuselage shape and transfer hoop loads.
- **Load Integration: Shear clips** must be installed at all frame-stringer intersections to ensure efficient load transfer between the floating frames and the skin-stringer assembly.

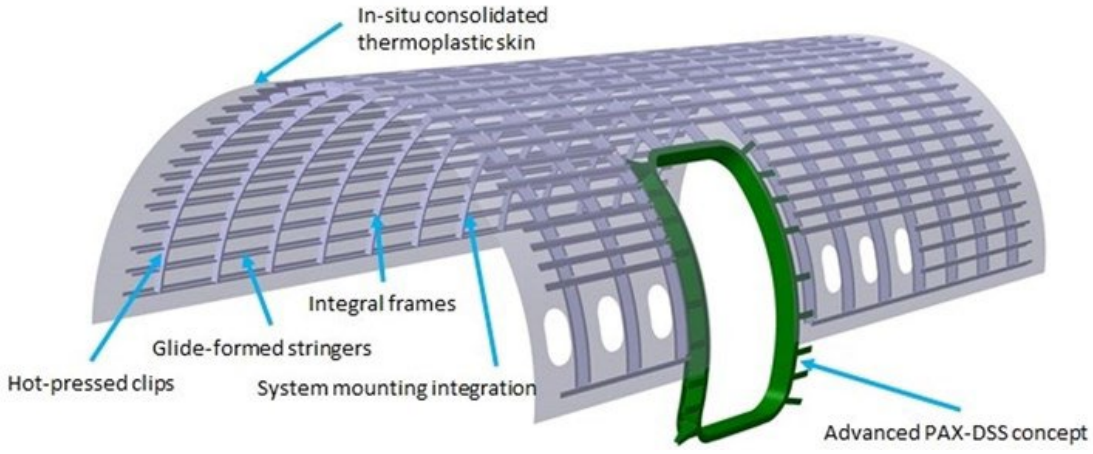

Figure 53. Multifunctional Fuselage Demonstrator MFFD Demonstrator Upper Half of Fuselage (58)

3.2 Structural Layout and Architecture

The structural architecture of the cargo door follows a semi-monocoque design philosophy. This configuration utilises a monolithic composite skin reinforced by a grid of longitudinal stringers and circumferential frames. This approach was selected to maximise the strength-to-weight ratio while providing the necessary damage tolerance against ground operations.

3.2.1 Monolithic Skin

The **outer skin** acts as the primary aerodynamic surface and pressure vessel. Unlike earlier generation aircraft that utilised aluminium skin panels, this design employs a solid carbon fibre reinforced polymer laminate. The skin thickness was defined as $3\,mm$ to withstand the operational pressure differential while minimizing weight. In the conceptual geometric model, the skin is represented as a continuous lofted surface derived from the fuselage master geometry to ensure a flush aerodynamic fit. An **inner skin** is also incorporated into the design to enclose the internal structure and protect the mechanism, effectively creating a structural box.

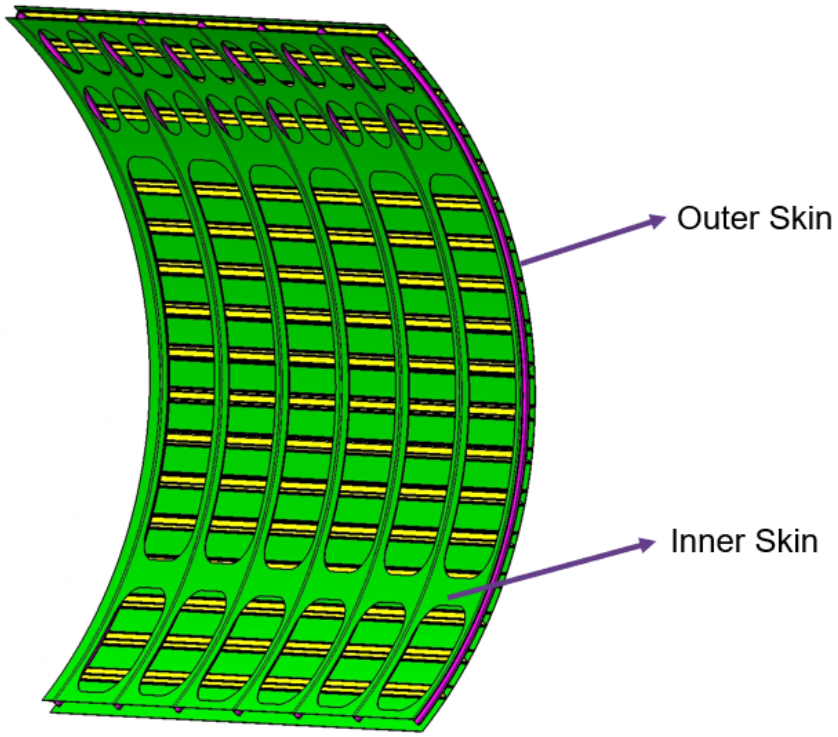

Figure 54. Isometric view of the monolithic Inner and Outer Skin

3.2.2 Longitudinal Stiffeners (Omega Stringers)

To resist buckling under compressive fuselage bending loads, the skin is stiffened by 13 longitudinal stringers. These components are spaced radially at 7.5-degree intervals across the door arc. An omega (Ω) profile was selected over traditional blade or T-stringers for specific structural reasons. This closed-section profile offers superior torsional rigidity compared to open sections. Furthermore, it provides two distinct bond lines at the feet of the profile which increases the total adhesive area and resistance to impact-induced delamination.

The stringer geometry was sized with a height of $30\ mm$ and a total base width of 70 mm. Each foot of the omega profile is $20\ mm$ wide to provide a substantial bonding surface. The top cap is $30\ mm$ wide to support bending loads.

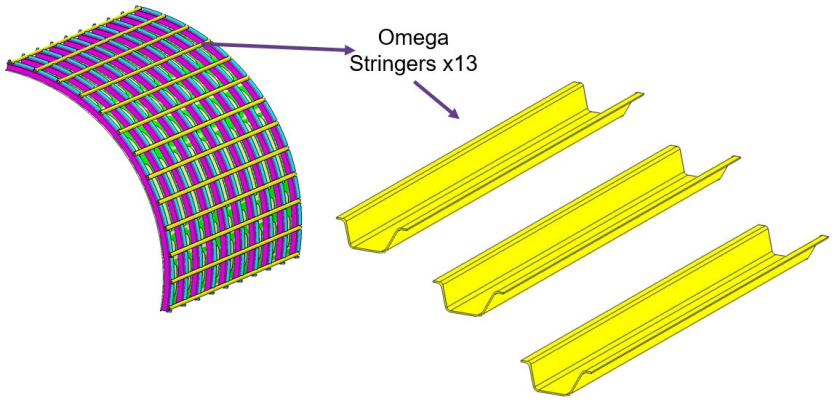

Figure 55. Isometric View of Omega Stringers

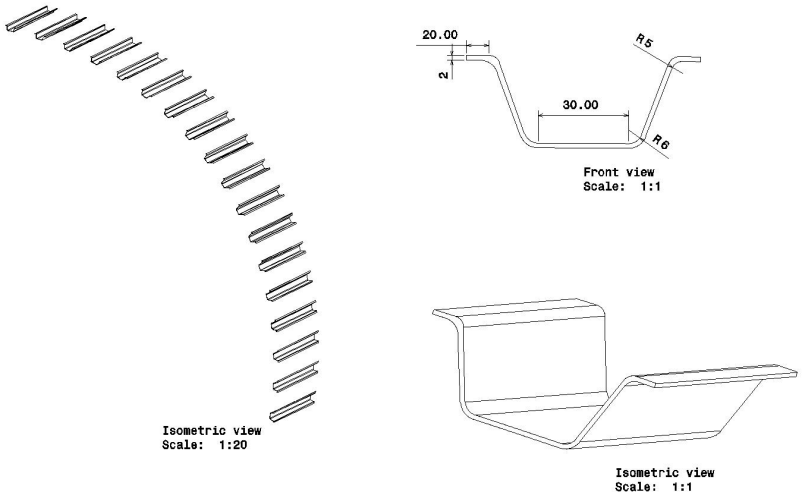

Figure 56. Cross-Sectional Dimensions of the Omega Stringer Profile

3.2.3 Circumferential Frames (C-Frames)

Vertical stiffness is provided by 10 circumferential frames. These are spaced at 492 mm intervals along the longitudinal axis of the door. These frames transfer the hoop loads from the skin into the door hinge and latching mechanisms. The frames feature a z-channel profile with a $110\ mm$ web height and a total width of $70\ mm$. This geometry provides the deep section modulus required to prevent ovalisation of the fuselage under pressurisation loads.

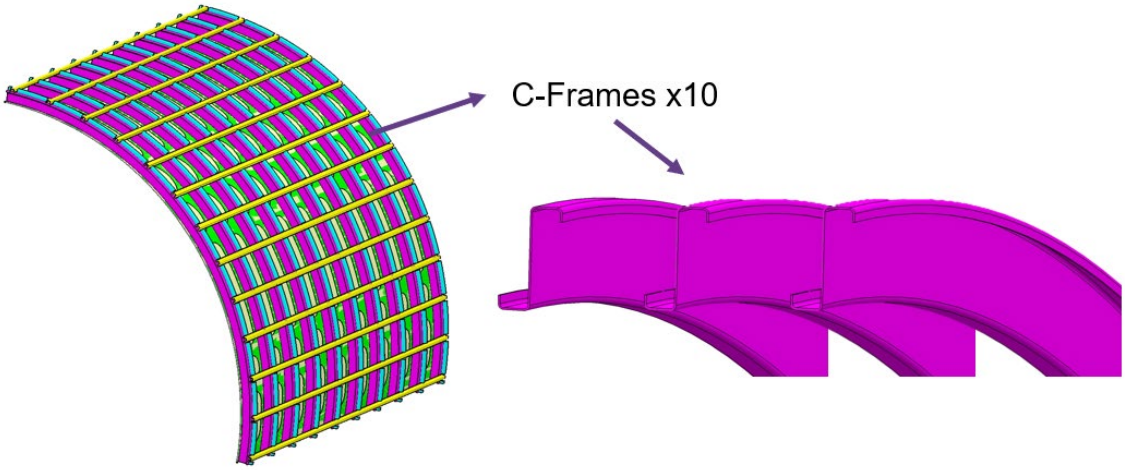

Figure 57. Isometric View of C-Frames

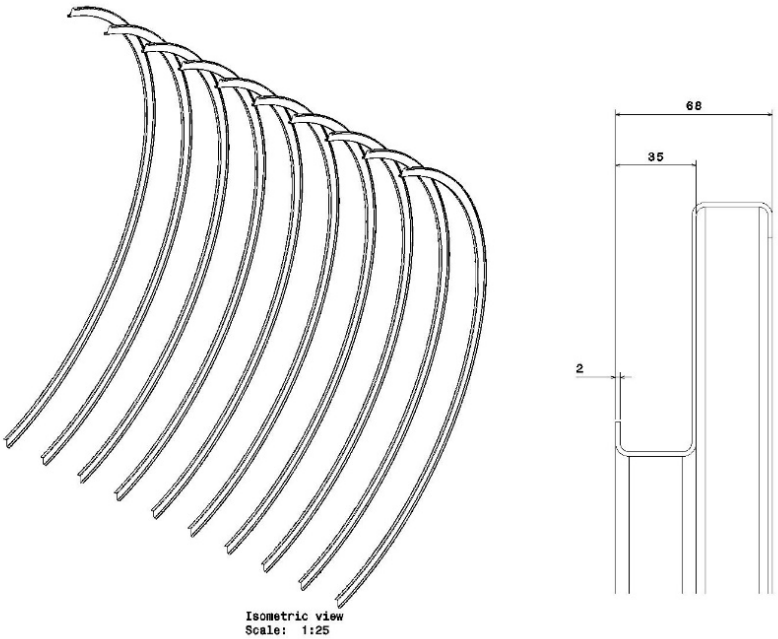

Figure 58. Cross-Sectional Dimensions of the C-Frames Profile

3.2.4 Shear Clips

To integrate the longitudinal and circumferential stiffeners, 10 shear clips are located at the frame-stringer intersections. These components have dimensions of $60\,mm$ in height and $35\,mm$ in width. They are installed at 492 mm intervals aligning with the frame stations. These clips ensure load transfer between the floating frames and the skin-stringer assembly. This prevents frame tripping or lateral instability under load.

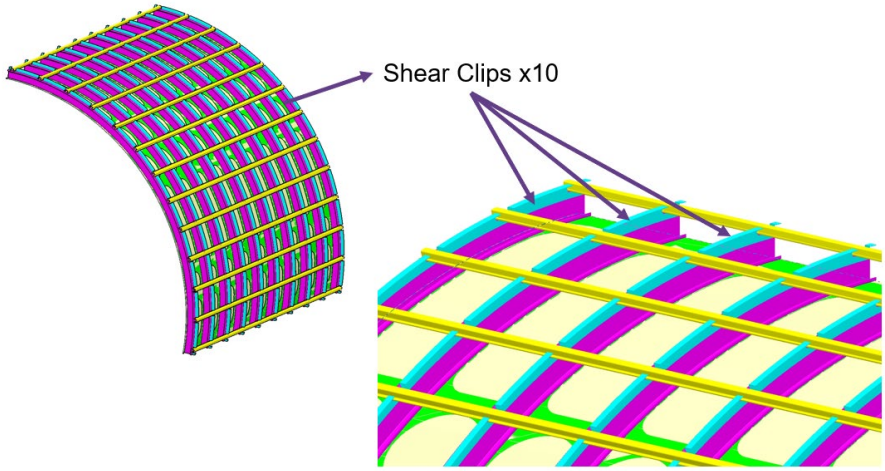

Figure 59. Isometric View of Shear Clips

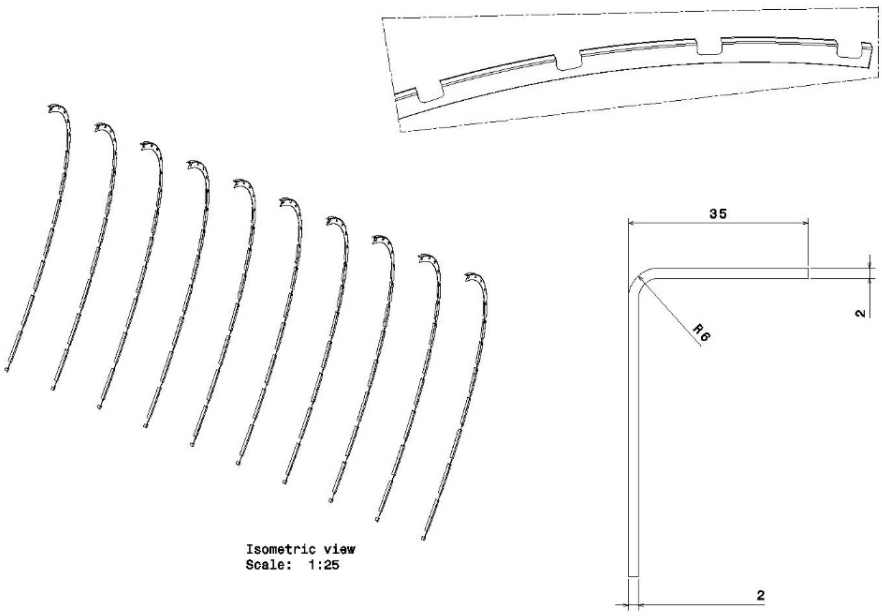

Figure 60. Cross-Sectional Dimensions of the Shear Clips

3.3 Geometric Modelling in CATIA V5

The transition from conceptual requirements to a high-fidelity three-dimensional model was executed using CATIA V5. This software was selected for its advanced surface modelling capabilities. Specifically, the generative shape design workbench was utilised as it is essential for capturing the complex aerodynamic curvature of the fuselage.

3.3.1 Fuselage Lofting and Surface Generation

To ensure the cargo door geometry accurately matched the Airbus A350-1000 airframe, a reverse-engineering approach was adopted using the Sketch Tracer functionality. This is often referred to as the painting gallery method. Official 2D orthogonal drawings of the aircraft including front, side, and top views were imported into the 3D workspace as reference planes. These raster images were scaled 1:1 to align with the known fuselage diameter of 5.96 metres.

Splines were then generated over the 2D reference lines to create the master guide curves. A multi-section surface loft was executed between these guides to generate the primary fuselage skin. This process ensured that the outer surface of the cargo door maintained perfect tangency with the surrounding airframe. This preserves the aerodynamic profile required for flight.

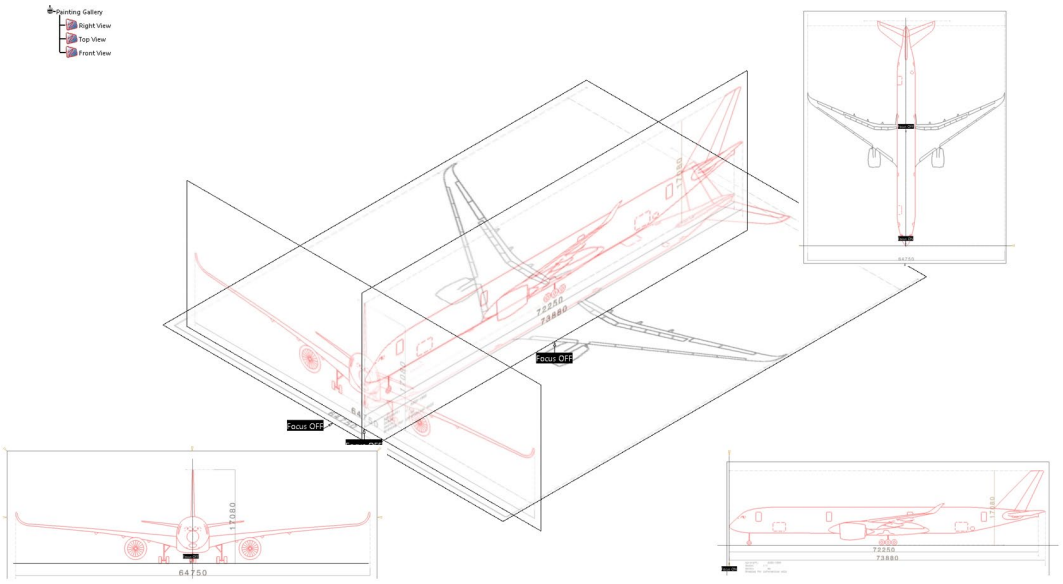

Figure 61. CATIA V5 Reference Planes Setup - Painting Gallery

3.3.2 Component and Assembly Generation

Following the generation of the master surface, the structural constituents defined in Section 3.2 were modelled as separate solid bodies. The stringer profiles were sketched on planes normal to the skin surface and swept along the longitudinal axis of the door curvature. A circular pattern operation was utilised to distribute the 13 stringers at the specified 7.5-degree radial intervals. Similarly, the circumferential frames were extruded and positioned at $492\,mm$ intervals. The final assembly integrates the skin, stringers, frames, and shear clips into a unified digital mock-up. This establishes the geometric baseline for the cargo door.

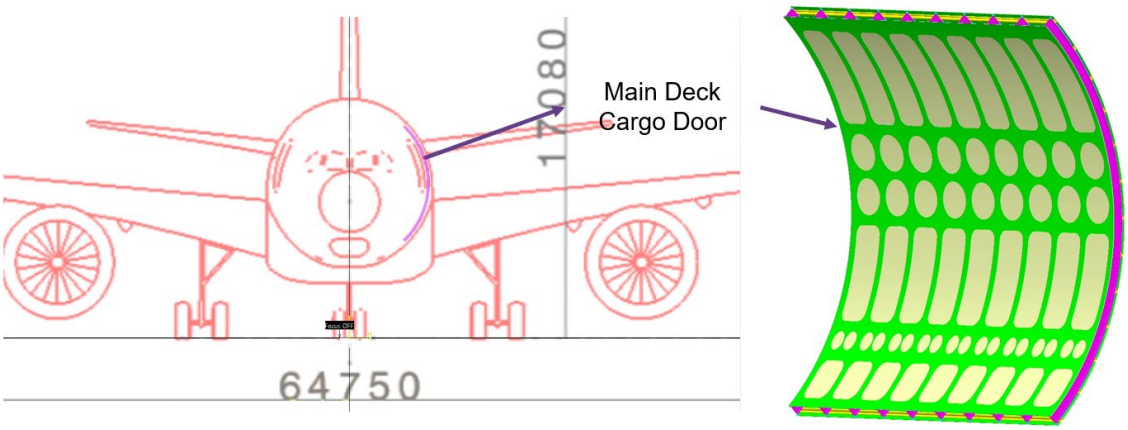

Figure 62. Isometric view of the full cargo door assembly in CATIA V5

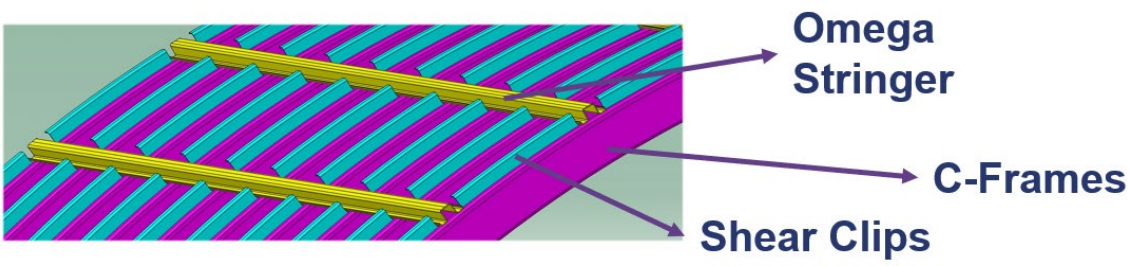

Figure 63. Fuselage Overview without Outer and Inner Skin

3.4 CAD Model Generation

The complete CAD assembly described in Section 3.3 defines the full architectural scope of the cargo door. However, simulating the entire structure for a localised impact event is computationally prohibitive and unnecessary for capturing the critical failure modes. The primary objective of this research is to investigate the onset of barely visible impact damage. This is a localised phenomenon dominated by the interaction between the skin and the stringer immediately beneath the impactor.

Consequently, the geometric domain for the finite element analysis was simplified. Rather than exporting the full door assembly, the specific geometry of the outer skin and the omega stringers was recreated within the simulation environment based on the dimensions defined in this chapter. Components such as the circumferential frames, shear clips, and inner skin were excluded from the explicit impact model. These components are critical for global fuselage stiffness but remote from the local impact zone. This sub-structuring approach allows for a highly refined mesh density in the critical skin-stringer bond line. It ensures accurate prediction of delamination without the computational cost of solving the entire door assembly.

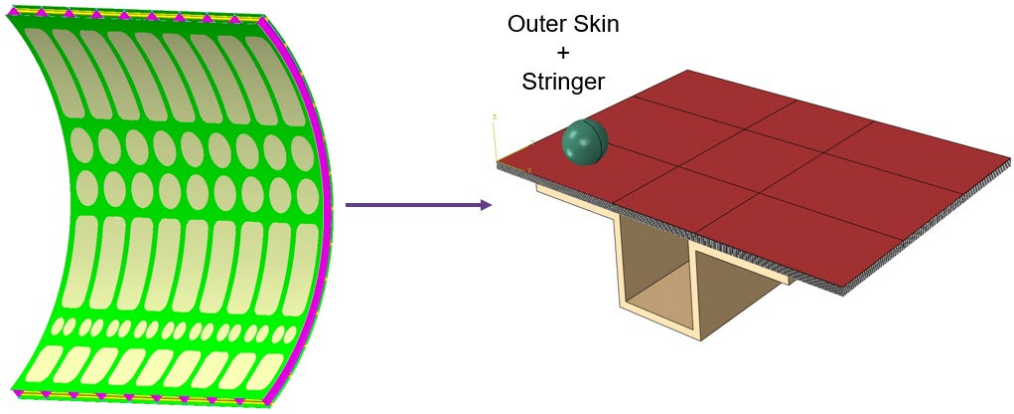

Figure 64. Schematic Showing the Full Door vs The Simplified Skin-Stringer Domain Used for Analysis

4 Finite Element Model Development and Simulation Methodology

While Section 3 established the geometric foundation and conceptual design of the cargo door, this section details the transition from physical geometry into a accurate numerical model designed to predict structural response. The primary objective of this model is to achieve high-fidelity predictions of stress distribution under internal pressurisation and to evaluate structural failure during external impact events.

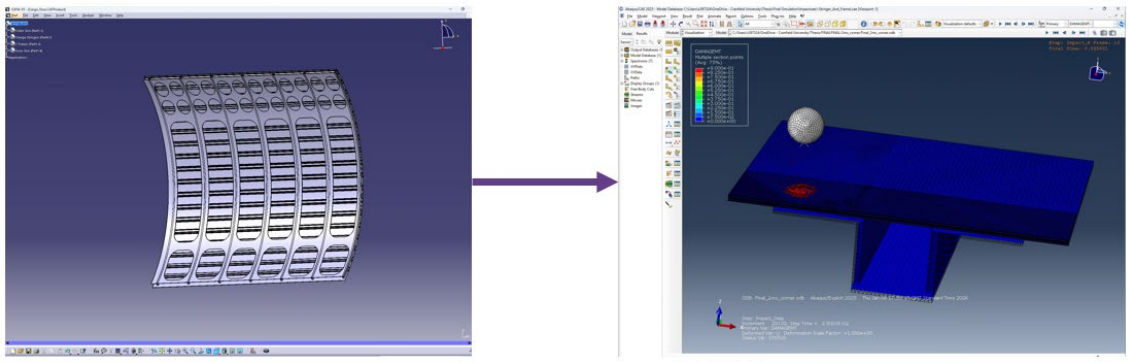

Figure 65. Transition from 3D Model to FEA

To achieve this, Abaqus was selected as the primary numerical tool. This software is chosen for its proven robustness in handling high-velocity, non-linear impact dynamics and its sophisticated ability to manage complex contact definitions through explicit dynamic simulations. The following sections outline the specific modelling parameters and failure laws implemented to ensure the integrity of the results.

4.1 Pre-Processing and Meshing

The reliability of the FEA is fundamentally dependent on the pre-processing steps, and meshing is one of the most critical steps in performing an accurate FEA simulation. A mesh is made up of elements which contain nodes that hold the coordinate locations in space that represent the shape of the geometry.

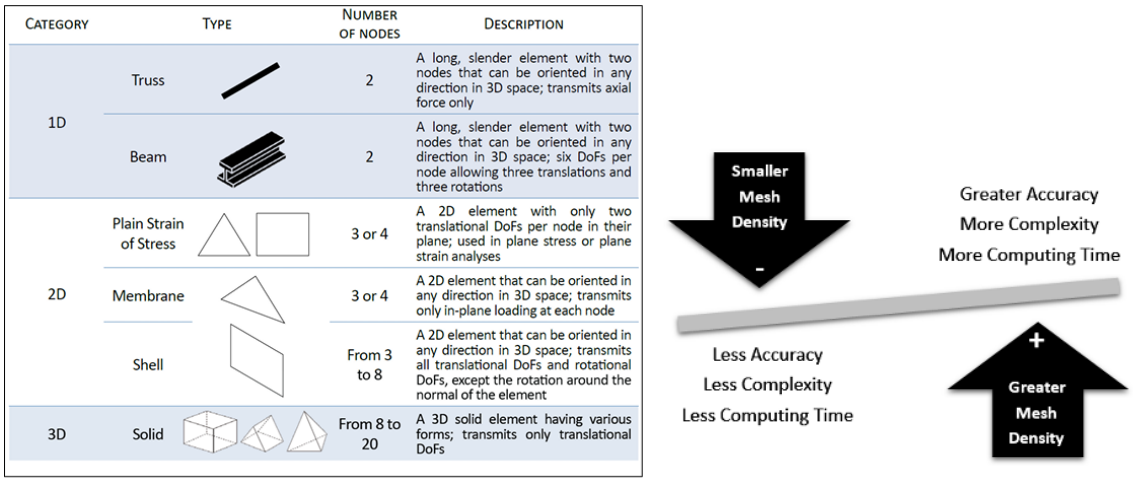

Category	Type	Number of Nodes	Description
1D	Truss	2	A long, slender element with two nodes that can be oriented in any direction in 3D space; transmits axial force only
	Beam	2	A long, slender element with two nodes that can be oriented in any direction in 3D space; six DoFs per node allowing three translations and three rotations
2D	Plain Strain of Stress	3 or 4	A 2D element with only two translational DoFs per node in their plane; used in plane stress or plane strain analyses
	Membrane	3 or 4	A 2D element that can be oriented in any direction in 3D space; transmits only in-plane loading at each node
	Shell	From 3 to 8	A 2D element that can be oriented in any direction in 3D space; transmits all translational DoFs and rotational DoFs, except the rotation around the normal of the element
3D	Solid	From 8 to 20	A 3D solid element having various forms; transmits only translational DoFs

Figure 66. Element Types and Mesh Density (59)

The mesh architecture must be sufficiently refined to capture damage initiation and stress gradients accurately, while remaining within the limits of computational economy to avoid being prohibitive. Inadequate meshing or a lack of quality control can lead to excessive element distortion, resulting in unreliable data or simulation instability. Consequently, achieving mesh convergence is a critical prerequisite for ensuring the reliability and physical validity of the impact results presented in this research.

4.1.1 Element Selection

The element type for the cargo door model has been chosen from the continuum shell family (SC8R element). The Abaqus SC8R is an 8-node, quadrilateral, reduced-integration continuum shell element.

Continuum shells provide the distinct advantage of featuring nodes both the upper and lower surfaces of each composite ply. This nodal configuration is essential for accurately capturing the traction separation behaviour between adjacent laminates correctly without having to account for rotational degrees of freedom in the cohesive element formulation (60,61).

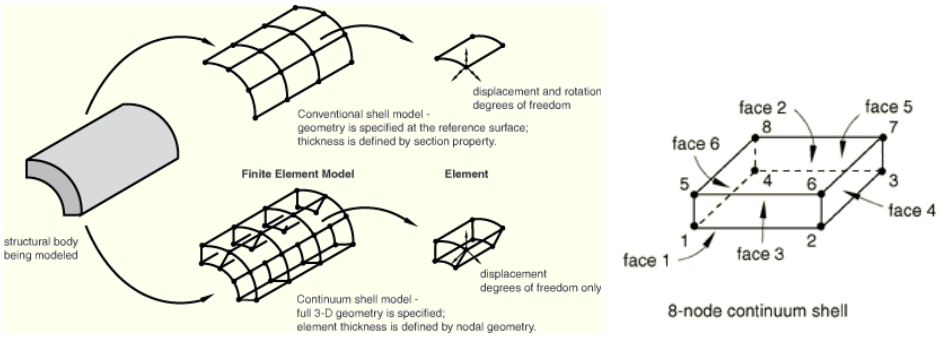

Figure 67. Continuum Shell Model (SC8R) (60,62)

Consequently, SC8R elements facilitate robust two-sided contact analysis and account for through-thickness deformation and changes in laminate thickness. This makes them ideally suited for modelling the complex contact conditions and energy distribution inherent in the impact simulations conducted for this research.

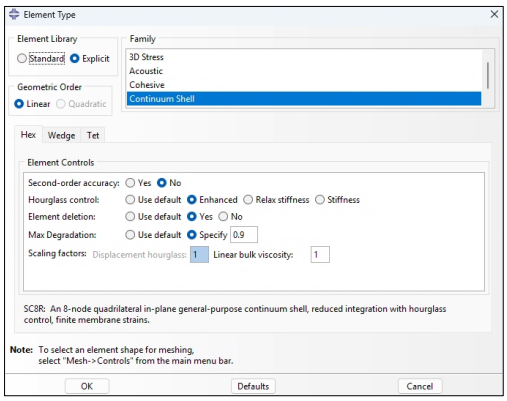

Figure 68. Element Type Selection in Abaqus – Continuum Shell SC8R

The impactor is defined using R3D4 discrete rigid element type. This is a 4-node, 3D bilinear rigid quadrilateral element specifically designed for surfaces that do not undergo deformation. A rigid formulation was selected because the internal strain or damage of the impactor is not a research objective (63).

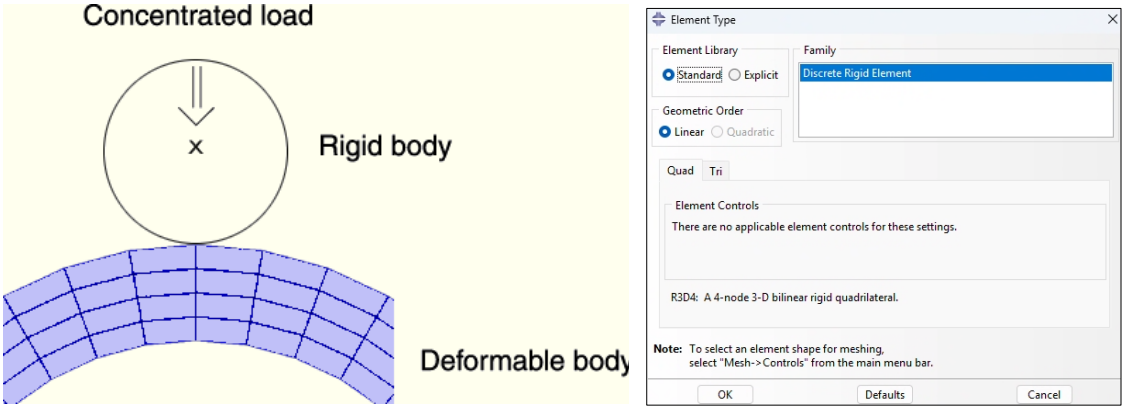

Figure 69. Discrete Rigid Element Type R3D4 (64)

The primary function of the rigid element is to serve as a high-stiffness vehicle for energy transfer into the cargo door. The use of R3D4 elements significantly enhances computational efficiency, as the solver bypasses internal element-level stress calculations for the rigid body, focusing all available processing power on the failure mechanics of the composite target (63).

Component	Element Type	Technical Justification
Outer Skin	*SC8R*	Through-thickness contact and accurate traction separation (delamination) analysis
Inner Skin		
Stringer		
Impactor	*R3D4*	Non-deformable impactor

Table 4.1 Assembly Mesh Element Types

4.1.2 Mesh Generation and Quality

The mesh generation strategy is dictated by the level of structural fidelity required to capture damage initiation. For the Main Deck Cargo Door simulations, a biased meshing approach is implemented to prioritise numerical accuracy in the strike region. Specifically, the element size within the impact zone is reduced to half that of the surrounding area, resulting in twice the mesh density per unit of surface area. This local refinement is essential for accurately capturing steep stress gradients during energy transfer while maintaining computational economy in the non-impact zones.

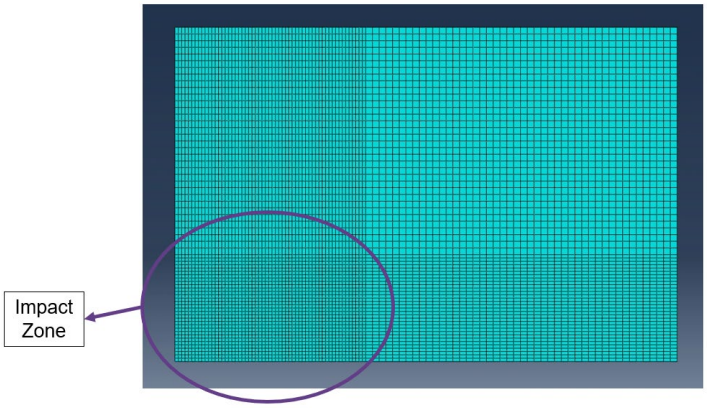

Figure 70. Impact Zone Mesh Modelling

To capture delamination mechanics, each composite layer is modelled as a discrete 3D part. This enables the implementation of specific cohesive interactions at every interlaminar interface. This discrete methodology allows for granular tracking of through-thickness shear and progressive failure on a ply-by-ply level, providing higher fidelity than standard composite layup definitions.

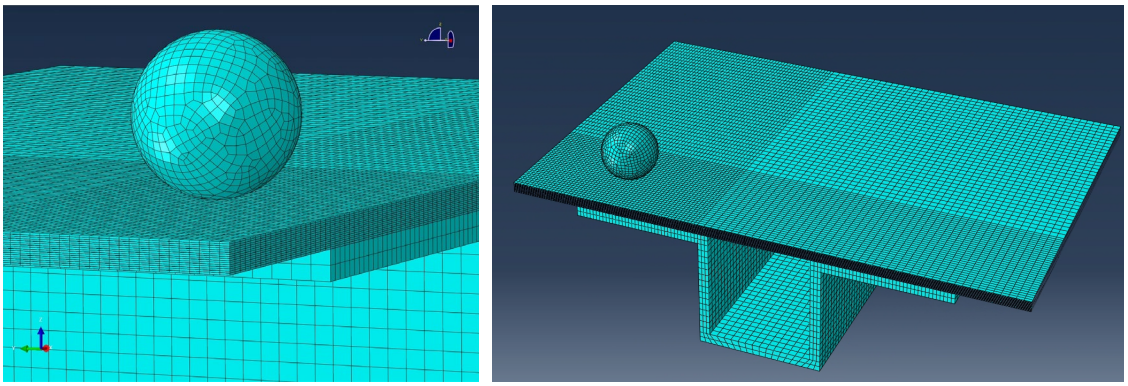

Figure 71. Assembly Mesh Generation

Further elements controls have been introduced to the mesh generation.

- **Enhanced hourglass control** is employed to ensure numerical accuracy when modelling non-linear material behaviours and tracking structural displacements. This method provides superior coarse-mesh accuracy and is specifically designed to handle the non-linear response of materials at high strain levels. By suppressing zero-energy deformation modes, the model maintains physical validity during the high-velocity impact events analysed in this research (65).
- **Element deletion** criterion is implemented to maintain simulation stability and prevent numerical failure. This feature automatically removes heavily distorted elements that would otherwise cause the simulation to crash due to mesh instability. By enabling the removal of failed elements, the model can realistically represent material failure and fracture propagation, ensuring computational efficiency during highly non-linear events (66).
- **Maximum degradation** threshold is set to 0.9, overriding the default settings to ensure elements are removed as they approach total failure. Once an element reaches this 90% stiffness degradation limit, it is triggered for deletion. This setting provides critical stability, and it prevents severely damaged elements from undergoing extreme distortion, thereby ensuring consistent mesh convergence during the most critical phases of structural failure (67).

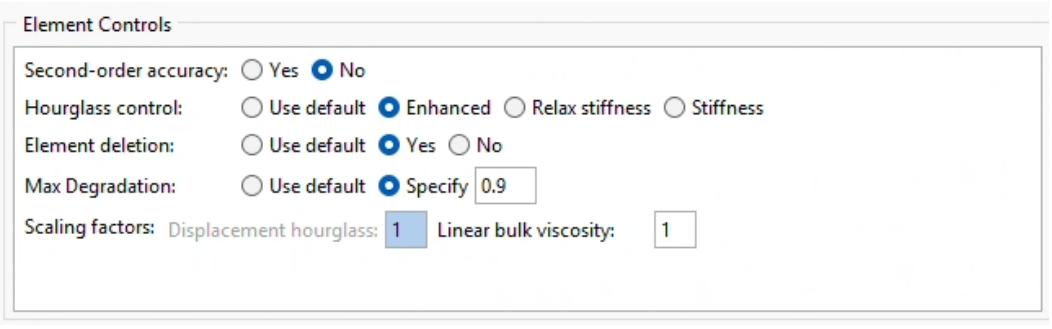

Figure 72. Mesh Element Controls

4.2 Impact Source Modelling

Aviation regulatory standards provide distinct requirements for modelling impact sources based on the intended threat scenario. For high-velocity events, such as bird strikes, EASA CS 25.631 and FAR 25.631 mandate that aircraft must remain capable of continued safe flight after a strike from a $1.8\ kg\ (4\ lb)$ bird at the design cruising speed (V_c) (68). However, for the low-velocity impacts addressed in this research, which are characterised by Barely Visible Impact Damage (BVID), the industry adopts a different standardised approach to ensure results are comparable across manufacturers.

The primary standard for low-velocity impact on composite coupons is **ASTM D7136**. This standard defines the parameters for a "Drop-Weight Impact" test, specifically requiring a 16 mm diameter hemispherical steel impactor head. While it typically utilises a standard carriage mass of $5.5\ kg$, the mass is often varied to achieve specific kinetic energy targets (69).

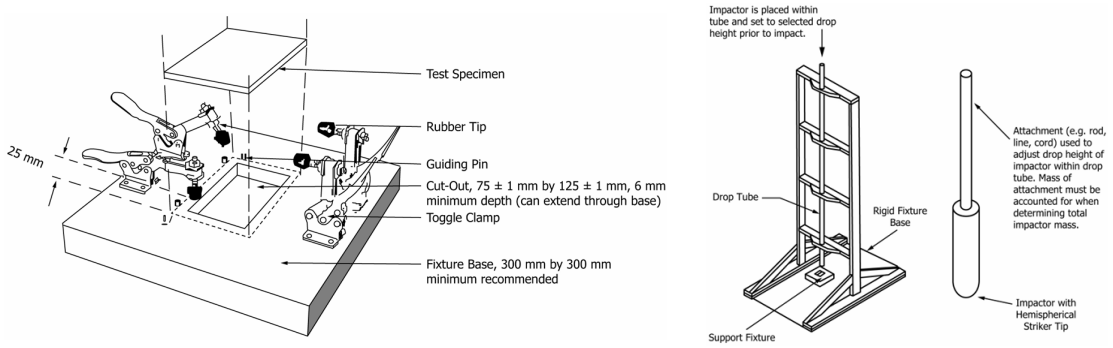

Figure 73. ASTM D7136 - Impact Device

Furthermore, regulatory guidance from EASA AMC 20-29 and FAA AC 20-107B defines energy thresholds for certification. Category 1 (BVID) damage, which typically results from tool drops or small hailstones, is evaluated between $20\ J$ and $50\ J$. In contrast, Category 2 damage involves higher energy strikes, such as ground support equipment (GSE) collisions, which result in visible damage requiring immediate repair.

Aligned with the ASTM standards, the impactor in this study is modelled as a spherical body with a diameter of $\mathbf{16}\,\boldsymbol{mm}$ and an initial mass of $\mathbf{5}\,\boldsymbol{kg}$. This configuration allows for a direct evaluation of the structural response of the **Main Deck Cargo Door** across the established energy levels of $\mathbf{5}\,\boldsymbol{J}$, $\mathbf{20}\,\boldsymbol{J}$, **and** $\mathbf{40}\,\boldsymbol{J}$.

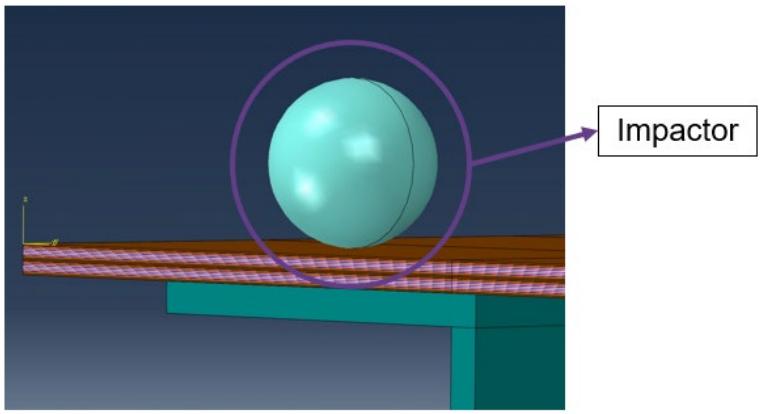

Figure 74. Impactor Model

As established in Section 4.1.1, the impactor is defined as a discrete rigid element to facilitate the direct transfer of kinetic and potential energy to the impacted fuselage skin. Rigid elements in Abaqus lack internal integration points, the part remains non-deformable and does not sustain internal stress throughout the simulation. By assigning a specific mass and velocity to a reference point on its surface, the component functions as a rigid impactor element, with the governing kinematic constraints detailed further in Section 4.4.

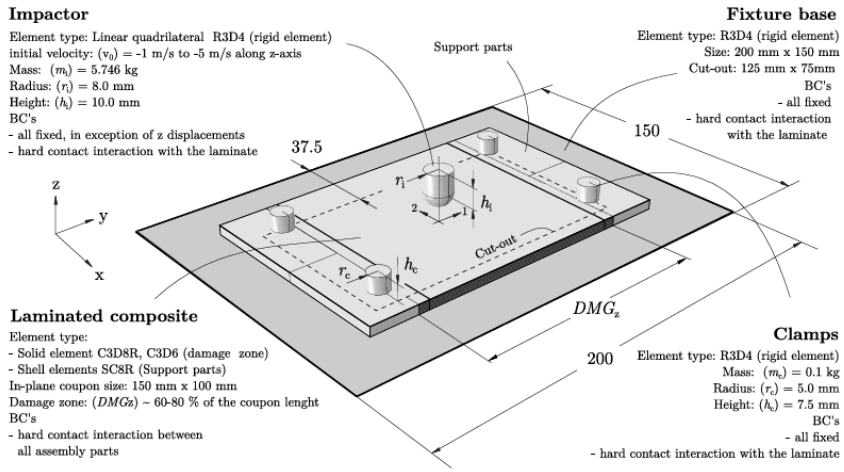

Figure 75. Simulation Setup Example for Low-Velocity Impact Damage of Composite Laminates (70)

4.3 Material and Failure Modelling

4.3.1 Material Specifications and Layup Definition

A unidirectional carbon fibre reinforced polymer pre-preg system, specifically **Hexcel AS4/8552**, was selected for the numerical model. This material represents a standard aerospace-grade composite system. It offers the high specific strength and damage tolerance required for primary fuselage structures subjected to impact loads.

Property Category	Parameter	Symbol	Value	Unit
Physical	Density	ρ	$1.58\ x\ 10^{-9}$	$tonne/mm^3$
Elastic	Longitudinal Modulus	E_1	137,100	MPa
	Transverse Modulus	E_2	8,800	MPa
	Major Poisson's Ratio	v_{12}	0.314	
	In-Plane Shear Modulus	G_{12}	4,900	MPa
	Out-of-Plane Shear Modulus	G_{13}	4,900	MPa
	Out-of-Plane Shaer Modulus	G_{23}	4,000	MPa
Hashin Damage Initiation	Longitudinal Tensile Strength	X^T	2,106.4	MPa
	Longitudinal Compressive Strength	X^C	1,675.9	MPa
	Transverse Tensile Strength	Y^T	74.2	MPa
	Transverse Compressive Strength	Y^C	322.0	MPa
	Longitudinal Shear Strength	S^L	110.4	MPa
	Transverse Shear Strength	S^T	110.4	MPa
Damage Evolution	Longitudinal Tensile Fracture Energy	G_{1c}^T	125.0	N/mm
	Longitudinal Compressive Fracture Energy	G_{1c}^C	61.0	N/mm
	Transverse Tensile Fracture Energy	G_{2c}^T	0.3	N/mm
	Transverse Compressive Fracture Energy	G_{2c}^C	0.87	N/mm

Table 4.2. Material Properties for Hexcel AS4/8552 Unidirectional Pre-preg

To accurately represent the physical door skin, the finite element model utilises a specific laminate stacking sequence designed to achieve quasi-isotropic behaviour. The laminate is constructed from 16 plies. Each ply has a cured thickness of $\mathbf{0.1875}\ \boldsymbol{mm}$. This results in a total shell thickness of $\mathbf{3.0}\ \boldsymbol{mm}$.

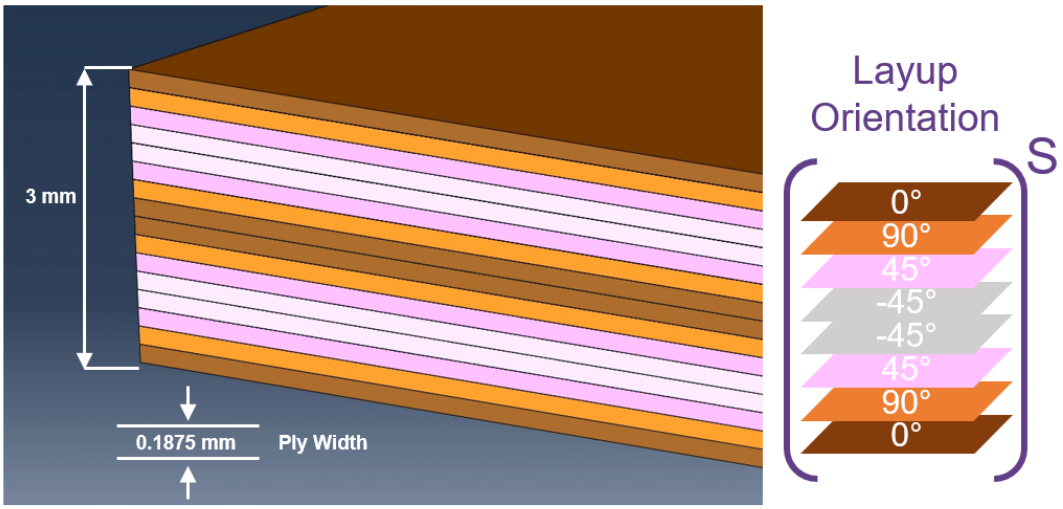

Figure 76. Schematic of the Laminate Stacking Sequence

The stacking sequence is defined as $[0/90/45/-45/-45/-45/90/0]_s$. This symmetric configuration places the 0° plies on the outer surfaces to maximise longitudinal bending stiffness. The internal $\pm$45° layers provide shear resistance while the 90° plies manage the hoop stresses generated by fuselage pressurisation. This ply schedule is applied to the continuum shell elements defined in Section 4.1.1. This ensures that the through-thickness integration points align with the physical orientation of the fibres.

4.3.2 Constitutive Damage Framework

Composite materials exhibit anisotropic behaviour, making it challenging to predict their structural response under specific conditions that induce stress or damage. Abaqus provides a constitutive damage framework that enables the user to predict this complex behaviour. This damage model requires three fundamental material specifications excluding the density to facilitate accurate damage predictions (71):

- **Elasticity** constants to define the structural response of the composite in its undamaged state.
- **Damage initiation** criteria, which identify the specific threshold where material degradation and damage initiation begin.
- **Damage evolution** properties, which characterise the post-damage behaviour used by the model to evaluate progressive material failure.

For elasticity properties, Abaqus utilises the plane stress condition of shell elements, requiring the definition of orthotropic material properties. This includes the shear moduli G_{13} and G_{23} , as transverse shear deformation is required for accurate shell performance. By defining the Poisson's ratio and the remaining elastic constants, the structural response in an undamaged state can be predicted.

$$\begin{Bmatrix} \varepsilon_1 \\ \varepsilon_2 \\ \gamma_{12} \end{Bmatrix} = \begin{bmatrix} 1/E_1 & -\nu_{12}/E_1 & 0 \\ -\nu_{12}/E_1 & 1/E_2 & 0 \\ 0 & 0 & 1/G_{12} \end{bmatrix} \begin{Bmatrix} \sigma_{11} \\ \sigma_{22} \\ \tau_{12} \end{Bmatrix}$$

Figure 77. Abaqus Shell Element Elasticity in Plane Stress (72)

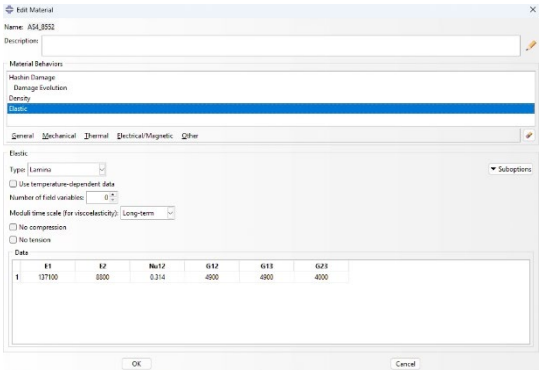

Figure 78. Elasticity Material Property Values

For damage initiation, Abaqus utilises the **Hashin** damage theory. This criterion evaluates four distinct damage initiation mechanisms: fibre tension, fibre compression, matrix tension, and matrix compression. Consequently, this model is highly suitable for composite materials, where multiple stresses and diverse failure mechanisms contribute to overall structural compromise.

Fiber tension $(\hat{\sigma}_{11} \geq 0)$:

$$F_f^t = (\frac{\hat{\sigma}_{11}}{X^T})^2 + \alpha(\frac{\hat{\tau}_{12}}{S^L})^2.$$

Fiber compression $(\hat{\sigma}_{11} < 0)$:

$$F_f^c = (\frac{\hat{\sigma}_{11}}{X^C})^2.$$

Matrix tension $(\hat{\sigma}_{22} \geq 0)$:

$$F_m^t = (\frac{\hat{\sigma}_{22}}{Y^T})^2 + (\frac{\hat{\tau}_{12}}{S^L})^2.$$

Matrix compression $(\hat{\sigma_{22}} < 0)$:

$$F_m^c = (\frac{\hat{\sigma}_{22}}{2S^T})^2 + [(\frac{Y^C}{2S^T})^2 - 1]\frac{\hat{\sigma}_{22}}{Y^C} + (\frac{\hat{\tau}_{12}}{S^L})^2.$$

Figure 79. Abaqus Hashin Damage Initiation Criteria (73)

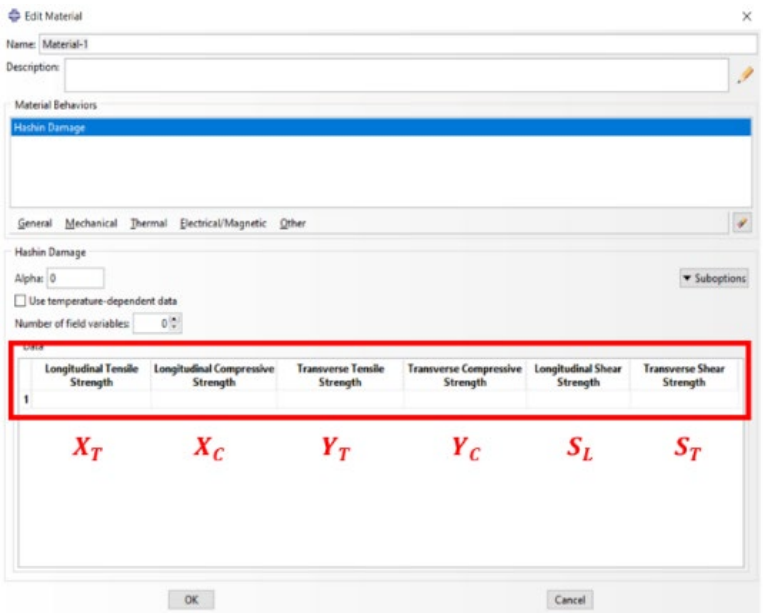

Figure 80. Hashin Damage Material Property Values (74)

Damage initiation and evolution are governed by the relationship between equivalent stress and equivalent displacement, as illustrated in the constitutive response curve. The linear elastic behaviour of the composite is represented by the initial ascending slope of the triangular area, leading to the peak which signifies the damage initiation point. Following this initiation, the descending slope on the right side of the peak represents the damage evolution phase, during which the material undergoes progressive stiffness degradation until total failure occurs (75).

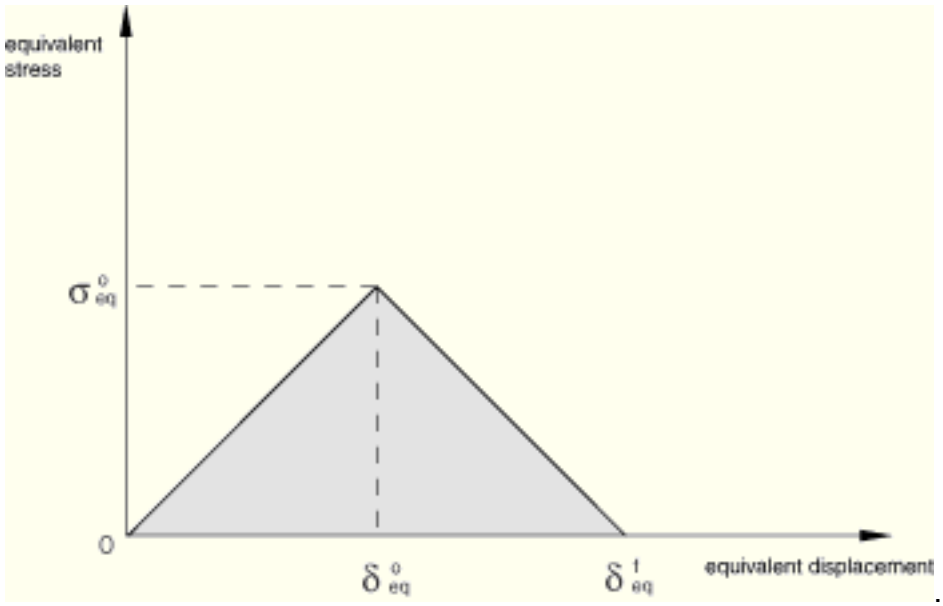

Figure 81. Abaqus Hashin Damage Initiation Criteria (75)

Figure 82. Hashin Damage Material Property Values (74)

Interlaminar delamination and skin-stringer debonding, is simulated using a surface-based cohesive zone modelling (CZM) framework. An executive decision was made to utilise **surface-based cohesive interactions** rather than discrete cohesive elements to model these interfaces. This approach eliminates the computational overhead and mesh-sensitivity associated with finite-thickness cohesive layers, favouring a more efficient interaction formulation that accurately captures the "zipping" failure modes of large-scale composite assemblies (76) (77).

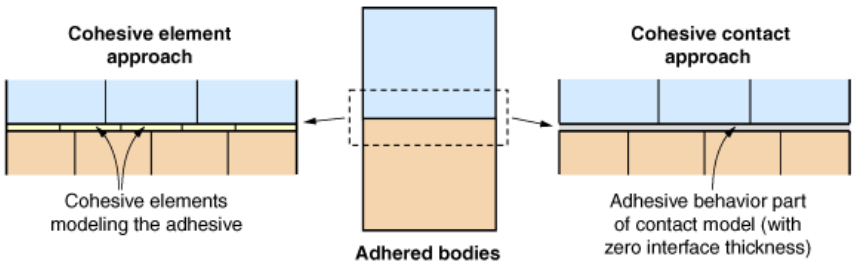

Figure 83. Cohesive Elements vs Cohesive Contact Approach (78)

The model employs the default contact interaction method for both the **ply interfaces** and the critical **skin-stringer bonds**. This implements an **uncoupled linear** elastic traction-separation law, where the normal and shear stiffness components are mathematically independent. As illustrated in Equation 4.1 and Figure 46, the uncoupled formulation uses a diagonal stiffness matrix (K), ensuring that displacements in one direction do not induce stresses in another. This selection is a critical stability measure; by avoiding mode-coupling during the initial elastic phase, the solver maintains robust convergence even under the high-frequency energy transfer of a GSE impact (78) (79).

$$\mathbf{t} = \begin{Bmatrix} t_n \\ t_s \\ t_t \end{Bmatrix} = \begin{bmatrix} K_{nn} & 0 & 0 \\ 0 & K_{ss} & 0 \\ 0 & 0 & K_{tt} \end{bmatrix} \begin{Bmatrix} \delta_n \\ \delta_s \\ \delta_t \end{Bmatrix} = \mathbf{K}\boldsymbol{\delta}.$$

(4.1) Abaqus Uncoupled Traction-Separation (79)

$$\mathbf{t} = \begin{Bmatrix} t_n \\ t_s \\ t_t \end{Bmatrix} = \begin{bmatrix} K_{nn} & K_{ns} & K_{nt} \\ K_{ns} & K_{ss} & K_{st} \\ K_{nt} & K_{st} & K_{tt} \end{bmatrix} \begin{Bmatrix} \delta_n \\ \delta_s \\ \delta_t \end{Bmatrix} = \mathbf{K}\boldsymbol{\delta}.$$

(4.2) Abaqus Coupled Traction-Separation (79)

While the elastic response is uncoupled, damage initiation is governed by a **quadratic traction (Quads)** criterion to realistically capture mixed-mode interactions at the threshold of failure. As shown in Figure 47, initiation is triggered when the combined interaction of normal and shear stresses exceeds the maximum strengths of 74.2 MPa and 110.4 MPa, respectively. This ensures that the skin-stringer flange separation (illustrated in Figure 45) accounts for the simultaneous peeling and shearing forces inherent in the impact zone (78).

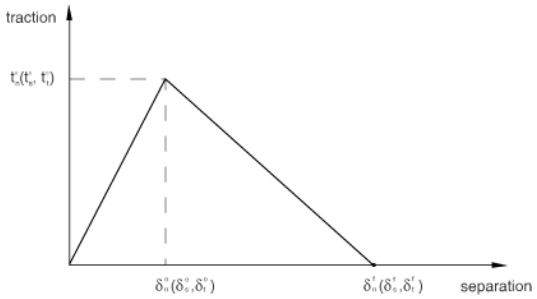

Figure 84. Abaqus Typical Traction-Separation Response (78)

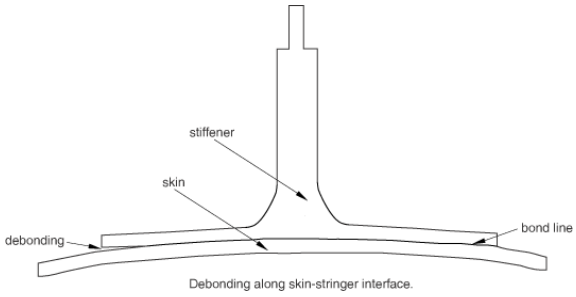

Figure 85. Abaqus Traction-Separation Modelling (79)

Following initiation, the Benzeggagh-Kenane (B-K) law controls the evolution of damage through energy dissipation. To align the simulation with composite fracture data, fracture energies of 0.3 $\frac{kJ}{m^2}$ (normal) and 0.87 $\frac{kJ}{m^2}$ (shear) were implemented, alongside a B-K exponent (η) of 1.45. This specific power-law formulation shown in Figure 48 allows the model to accurately track the transition from barely visible damage to structural debonding (80).

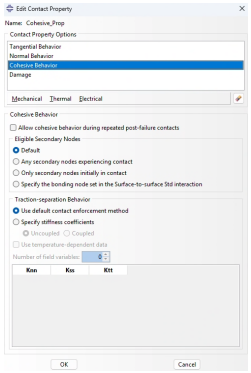

Figure 86. Abaqus Cohesive Contact

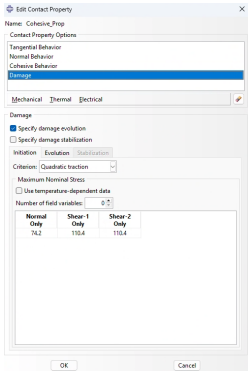

Figure 87. Abaqus Quads Damage Initiation

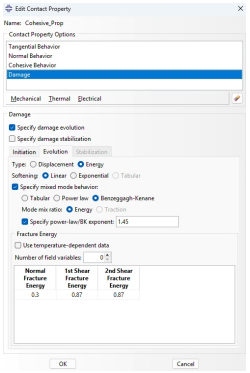

Figure 88. Abaqus B-K Damage Evolution

4.4 Boundary Conditions, Loads, and Interactions

To accurately simulate the structural response of the Main Deck Cargo Door, specific boundary conditions (BC) and kinematics (predefined fields) are applied to both the composite assembly and the rigid impactor. These settings are selected to replicate a high-fidelity impact scenario where the door is fixed to the airframe during a ground handling incident.

4.4.1 Structural Boundary Conditions

In reality the door skin is secured to the assembly. Therefore, a pinned condition is assigned to the edges of the skin and the stringer as shown in Figure 50, effectively restricting translation in all degrees of freedom.

$$U_1 = U_2 = U_3 = 0$$

(4.3) Structural BC - Pinned

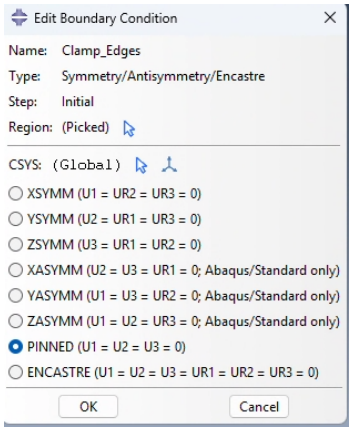

Figure 89. Abaqus Structural BC - Pinned

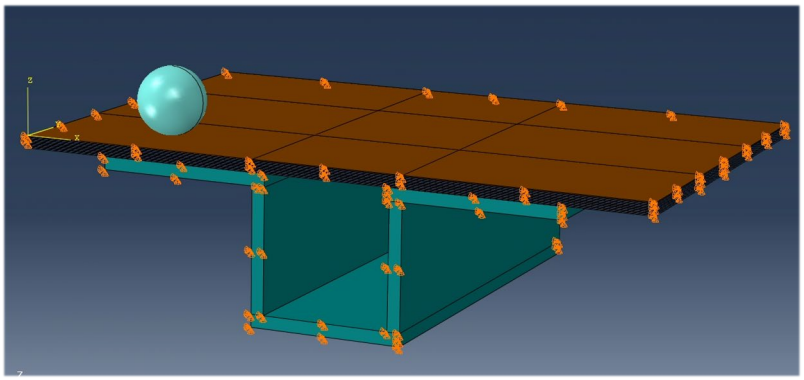

Figure 90. Skin-Stringer Assembly BC - Pinned

4.4.2 Impactor Kinematics and Loading

Abaqus governs the motion of the impactor through a reference point located on an assigned location, in this case a reference point is created at the bottom geometric centre of the impactor. To ensure a perfectly normal strike and to prevent parasitic energy loss through lateral sliding movement whilst impact, a displacement constraint is applied to restrict the impactor movement solely to the vertical Z-axis (U_3) and also restricting from translational and rotational degrees of freedom, illustrated in Figure 51.

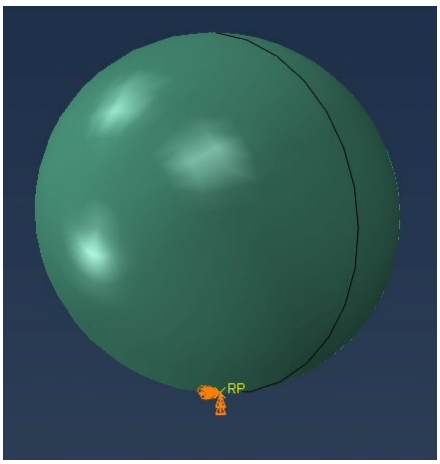

Figure 91. Impactor BC - U_3

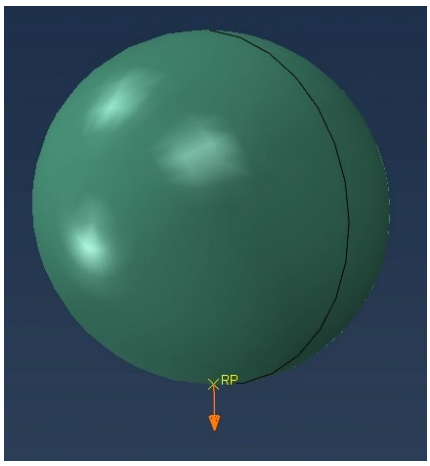

Figure 92. Impactor BC - V_3

Dynamic impact loading is applied through a predefined velocity field assigned to the reference point at the start of the simulation. Impact velocities of **1 ms^{-1}, 2 ms^{-1}, and 3 ms^{-1}** were assigned to represent kinetic energy (Variable name *ALLKE* in Abaqus) levels of **5 J, 20 J, and 40 J** respectively. These levels were chosen as an executive decision to simulate common "ramp/maintenance" scenarios, such as tool drops or equipment bumps, which are the primary sources of Barely Visible Impact Damage in service.

$$ALLKE = E_{KE} = E_k = \frac{1}{2} mv^2$$

(4.4) Kinetic Energy

4.4.3 Surface Interaction Assignments

The interaction properties are explained in Section 4.3 Material and Failure Modelling; these interaction properties are then assigned between the distinct parts of the model through a comprehensive contact assignment table. A general contact method is utilised to set individual property assignments, 18 items in total for this assembly as it can be seen in the below figure.

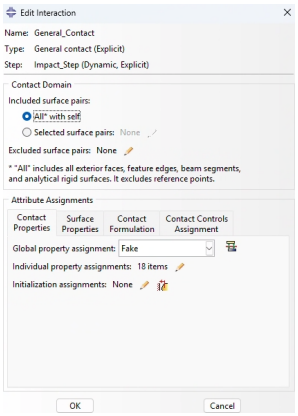

Figure 93. Abaqus General Contact Interaction

As shown in Figure 54, the **cohesive property** is assigned to each ply pair to facilitate delamination tracking, while a separate **friction property** is assigned to the impactor-to-skin interface. This assignment strategy ensures that the simulation captures the specific energy dissipation at every unique interface, including the high-stress regions where the stringers are bonded to the outer skin

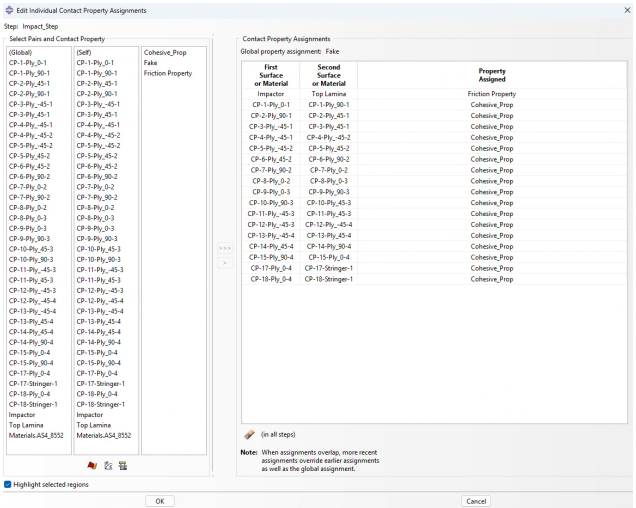

Figure 94. Abaqus Surface Interaction Assignments

4.5 Solver Setup

The impact simulation of the Main Deck Cargo Door is performed using the **dynamic explicit** solver. Explicit formulation is selected due to its superior ability to resolve highly non-linear dynamics, complex contact interactions, and the rapid stress wave propagation inherent in composite failure. The analysis is defined with a total step time of $\boldsymbol{0.05}\ \boldsymbol{seconds}$, ensuring the full duration of the impact and subsequent elastic rebound is captured.

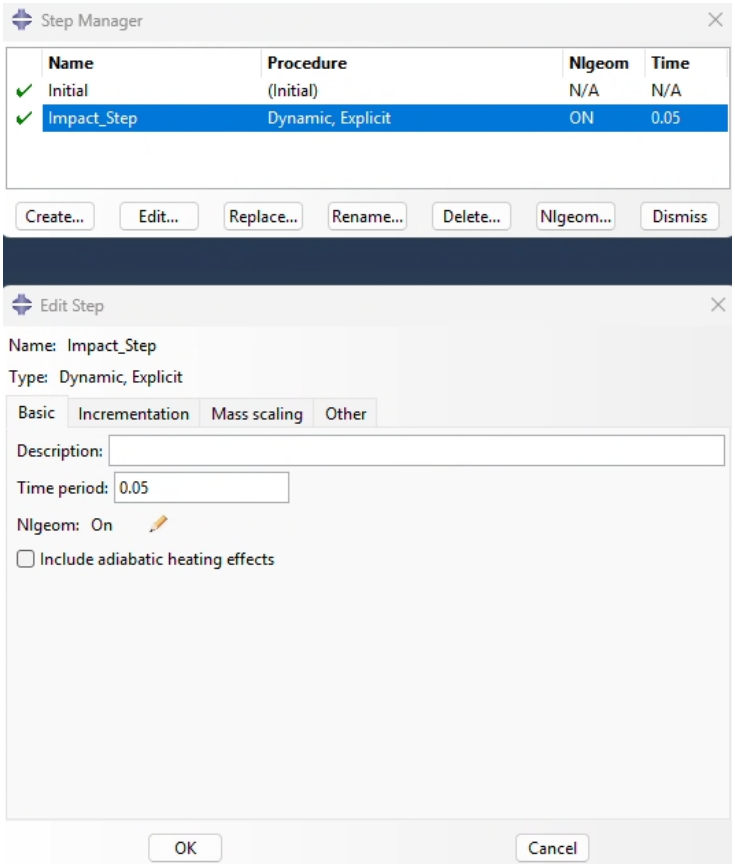

Figure 95. Abaqus Dynamic Explicit Solver

Large deformation effects are accounted for by enabling the nonlinear geometry (**Nlgeom)** setting. Nlgeom setting determines whether Abaqus will account for geometric nonlinearity which is essential for accurately capturing the membrane stresses in the door skin as it deflects under the impactor.

For the dynamic explicit solver stability, the time increment (Δt) must remain smaller than the time required for a stress wave to cross the smallest element in the mesh. This is known as the Courant-Friedrichs-Lewy (CFL) condition. To confirm stability condition, Equation 4.5 can be referred to (81).

Δt: The actual time increment used by the solver

L_{min}: The characteristic length of the smallest element in the mesh

c_d: The dilatational wave speed of the material

$$\Delta t \leq \Delta t_{stable} = \frac{L_{min}}{c_d}$$

(4.5) CFL Stability Condition (81)

$$c_d = \sqrt{\frac{E(1-v)}{\rho(1+v)(1-2v)}}$$

(4.6) Wave Speed for linear Elastic Material (81)

To maintain a balance between computational efficiency and physical accuracy, semi-automatic **mass scaling** was implemented with a target time increment of $1\ x\ 10^{-6}\ seconds$. This value was selected after multiple simulation comparisons as an optimal threshold as it aligns with the natural stable increment of the assembly while preventing localised element distortions from bottlenecking the simulation speed.

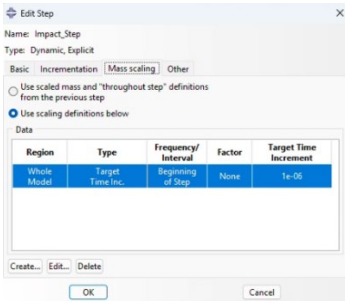

Figure 96. Dynamic Explicit Step - Mass Scaling

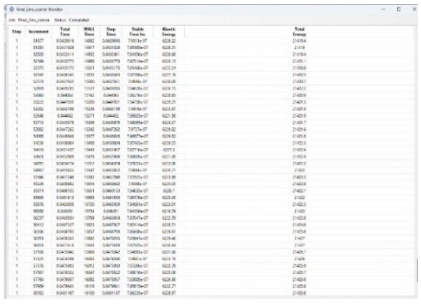

Figure 97. Dynamic Explicit Step - Mass Time Increments

Monitoring of the job status confirms that the solver maintained an actual stable time increment between $7.9\ x\ 10^{-7}$ and $9.3\ x\ 10^{-7}$ seconds throughout the event. This demonstrates that the mass scaling remained conservative and the target increment was never artificially forced at the expense of stability. The consistency of the total energy **(ETOTAL)** and kinetic energy **(ALLKE)** values validates that the internal energy dissipation through delamination and ply damage, confirming a high-fidelity representation of the physical impact event.

5 Results

This chapter presents the findings from the finite element simulations of the Main Deck Cargo Door assembly under various impact energy levels. The structural response is analysed across three specific energy regimes $5\,J$, $20\,J$, and $40J$, representing typical ground handling incidents. The analysis focuses on the initiation and propagation of damage within the composite laminates and the critical skin-stringer interfaces.

5.1 Model Verification

Prior analysing specific damage patterns, a rigorous model verification is performed to ensure the numerical validity of the explicit simulation solution. In explicit dynamics, the primary method of verification is the evaluation of the energy balance throughout the duration of the impact event. A mathematically sound simulation must demonstrate that the total energy (ETOTAL) remains constant, confirming that the work done by external forces is correctly balanced by internal energy dissipation and kinetic energy.

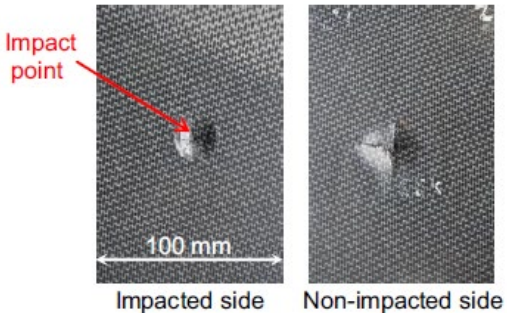

Figure 98. 25 *J* Impact of a CFRP Plate (2 mm) (13)

In addition to the numerical verification methods, extensive literature research was performed to benchmark the simulation results against existing experimental data. The research carried out by (11), (13) , (82), and (83) have been essential for experimental data availability. This comparative approach confirms the validity of the predicted damage patterns and facilitates a detailed discussion on potential structural improvements while identifying future refinements that could enhance the simulation's contribution to the field of composite impact research.

5.1.1 Energy Balance Analysis

The primary numerical verification involves evaluating the global energy balance throughout the impact event. As illustrated in **Figure 99**, the **total energy (ETOTAL)** is preserved with high precision across the 0.05 second step. This confirms that the impact simulation with complex contact interactions is stable.

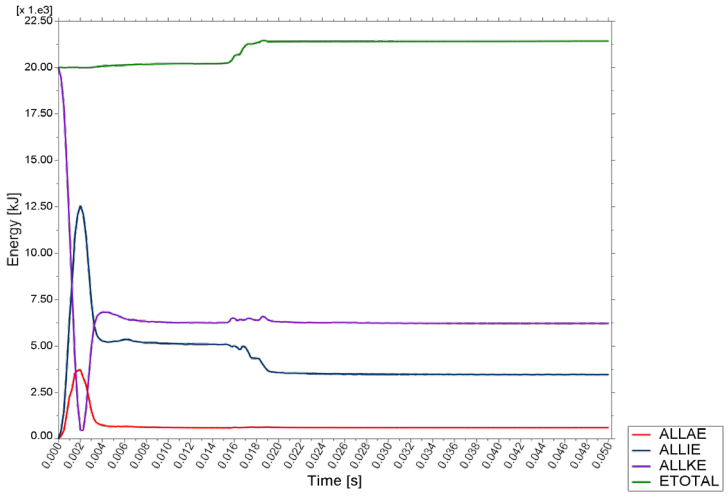

Figure 99. Global Energy History for the 20 J (2 m/s) Impact Scenario demonstrating ETOTAL Preservation

The **internal energy (ALLIE)** increases rapidly as the impactor deforms the door skin and initiates delamination, while the **kinetic energy (ALLKE)** demonstrates a corresponding decline as the impactor decelerates. The remaining plateau of internal energy post-impact represents the permanent energy dissipation caused by the quadratic traction damage and ply failure mechanisms defined in Section 4.3.

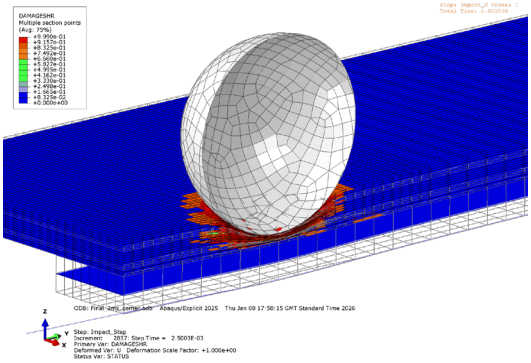

Figure 100. Transient Stress Distribution and Impactor Interaction at Peak Displacement (t = 0.0025 s)

5.1.2 Numerical Signatures of Mass Scaling

An executive analysis of the energy history reveals a marginal increase in the **ETOTAL** between $0.016\,s$ and $0.018\,s$. This is a characteristic numerical signature caused by the activation of semi-automatic mass scaling. As confirmed by the job monitor in Figure 101, at approximately $0.01589\ seconds$, the natural stable time increment of the model dropped to $5.83\ x\ 10^{-7}$

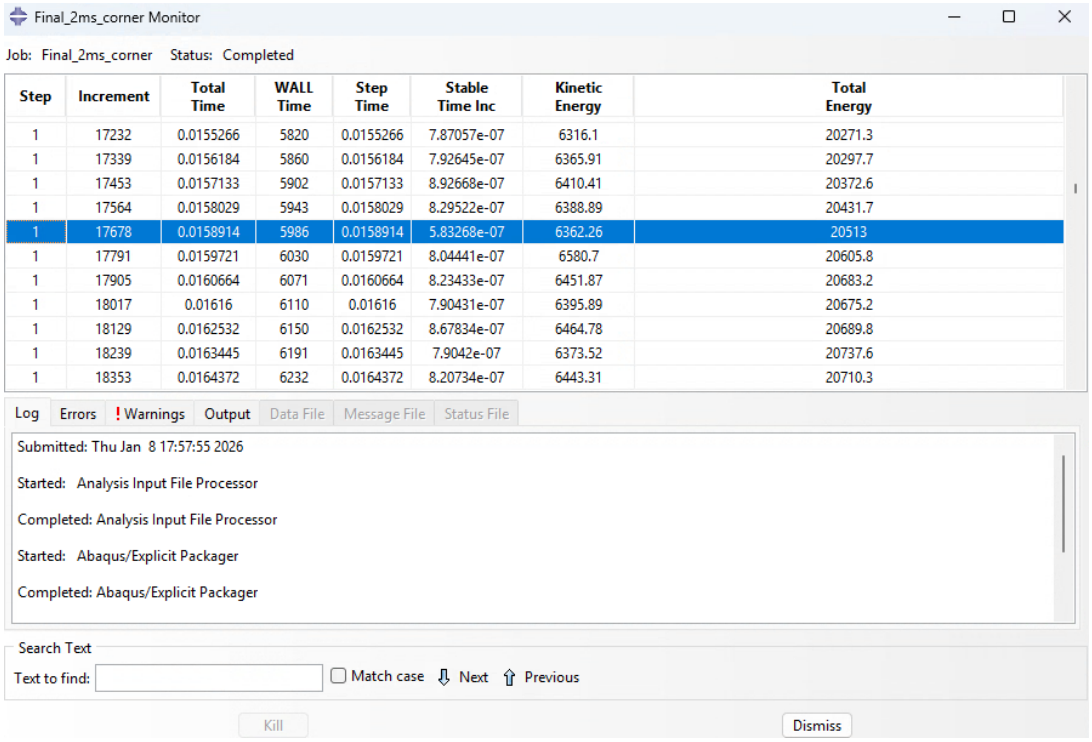

Figure 101. Explicit Solver Job Monitor illustrating Stable Time Increment Decay and Mass Scaling Trigger ($t\ \approx 0.016\ s$)

To maintain the executive target increment of $1\ x\ 10^{-6}\ s$, the solver artificially increased the nodal mass of the most distorted elements in the impact zone. This addition of mass introduces a negligible amount of artificial kinetic energy, explaining the slight rise in the green total energy line. Crucially, the **artificial strain energy (ALLAE)** remains significantly below the 5% threshold relative to the internal energy, proving that this mass scaling did not introduce non-physical inertial effects or compromise the accuracy of the structural damage results.

5.2 Chronological Impact Analysis

This section characterises the transient dynamic response of the skin-stringer assembly across the three impact energy scenarios $5\,J$, $20\,J$, and $40\,J$. The analysis is made of three distinct kinematic phases:

(1) Initial Loading & Contact

(2) Peak Deflection

(3) Elastic Rebound

5.2.1 Phase I: Inertial Loading & Contact Initiation

The impact event initiates with the rapid development of contact forces at the skin interface. Figure 102 compares the contact force history for the three impact velocities.

- **Peak Force Scaling:** The $5\,J$ $(1\,ms^{-1})$ case records a peak of approximately $3.5\,kN$, whereas the $40\,J$ $(3\,ms^{-1})$ case reaches a maximum of $8.5\,kN$. This sharp increase in force for the $40\,J$ scenario indicates a substantial increase in impact force compared to the substantial increase in impact speed.
- **Impulse Duration:** The contact duration is consistent across all cases at approximately $0.005\,s$, suggesting that the global structural stiffness of the door assembly governs the interaction time, independent of the impact velocity.

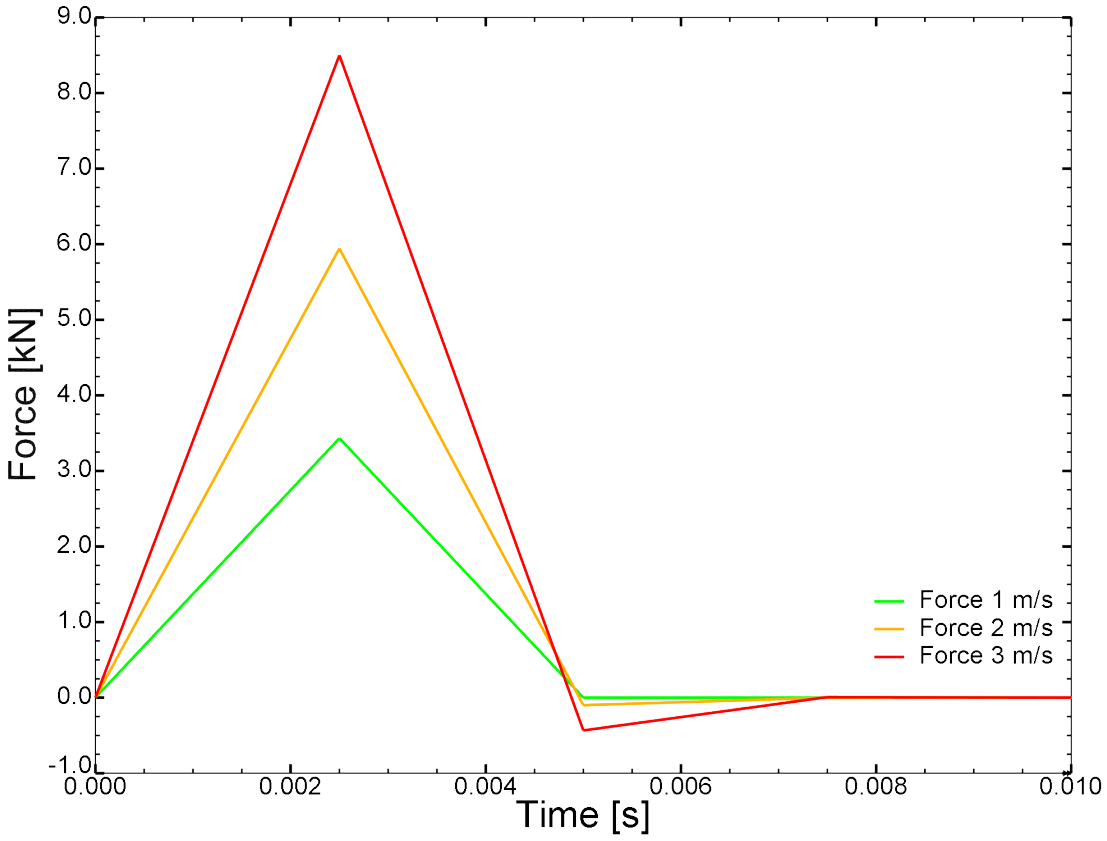

Figure 102. Impact Force Comparison

5.2.2 Phase II: Velocity Deceleration & Energy Absorption

The velocity history in Figure 103 provides a quantitative measure of the structural resistance during the impact event. The gradient of the velocity-time curve represents the instantaneous acceleration of the impactor $(a = dv/dt)$. According to Newton's Second Law $(F = ma)$, this acceleration is directly proportional to the resistive force exerted by the cargo door assembly.

Consequently, the magnitude of the velocity gradient serves as a direct indicator of the effective structural stiffness. A constant gradient implies a linear-elastic response, while a reduction in the gradient magnitude indicates a loss of structural integrity due to damage accumulation.

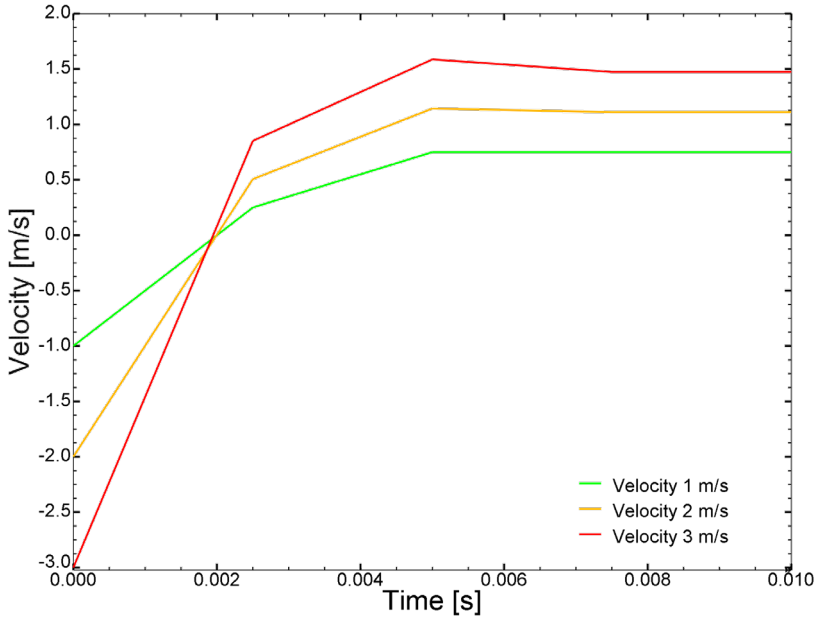

Figure 103. Velocity Comparison

Analysis of the **loading phase** $(t = 0\ to\ 0.0025\ s)$, where the initial interaction is characterised by the rapid deceleration of the impactor. Calculating the gradient of the velocity curves reveals a linear relationship between impact energy and structural response, consistent with linear elastic theory:

- $5\,J\ (1\ ms^{-1})$: Loading gradient = $500\ ms^{-2}$
- $20J\ (2\ ms^{-1})$: Loading gradient = $1002\ ms^{-2}$
- $40J\ (3\ ms^{-1})$: Loading gradient = $1541\ ms^{-2}$

The ratio of these gradients (500:1002:1541) correlates almost perfectly with the initial impact velocities (1:2:3). This proportionality confirms that at the onset of impact, the composite skin exhibits identical stiffness across all energy regimes, behaving as a linear-elastic spring

The **unloading phase** $(t = 0\ to\ 0.0025\ s)$ demonstrates a divergence from elastic behaviour observed in the loading phase. To quantify this, the average gradients were calculated using Equation 5.1 and are summarised in Table 5.1.

$$Gradient = \frac{V_2 - V_1}{t_2 - t_1} \quad \textbf{(5.1)}$$

Table 5.1: Evolution of Structural Stiffness via Velocity Gradients

Impact Case	Impact Velocity ($\boldsymbol{V_{in}}$)	Loading Gradient ($\boldsymbol{a_{load}}$)	Unloading Gradient ($\boldsymbol{a_{unload}}$)	Stiffness Ratio ($\boldsymbol{a_{unload}/a_{load}}$)
$\mathbf{5\,J}$	$1.0\ ms^{-1}$	$500\ ms^{-2}$	$200\ ms^{-2}$	$\mathbf{0.40}$
$\mathbf{20\,J}$	$2.0\ ms^{-1}$	$1002\ ms^{-2}$	$255\ ms^{-2}$	$\mathbf{0.25}$
$\mathbf{40\,J}$	$3.0\ ms^{-1}$	$1541\ ms^{-2}$	$294\ ms^{-2}$	$\mathbf{0.19}$

The **stiffness ratio** (a_{unload}/a_{load}) serves as a damage index. The $5\,J$ case maintains a ratio of **0.40**, indicating a robust elastic rebound where the stored strain energy is efficiently returned to the impactor.

In contrast, the $40\,J$ case exhibits a critical reduction in this ratio to **0.19**. If the structure similarly elastic, the unloading gradient for the $40\,J$ case would be expected to scale proportionally which is approximately $616\ ms^2$. The measured value of $294\ ms^2$ represents a $\mathbf{52\%}$ **deficit** in rebound stiffness. This loss of restoring force confirms that the stringer-skin interface has been compromised, it also suggests that the composite skin was nearly pierced through by the impactor.

5.2.3 Phase III: Peak Deflection & Elastic Rebound

The final phase of the chronological analysis focuses on the maximum deformation of the cargo door skin. Figure 104 presents the displacement time-history of the impactor for the three velocity cases.

The maximum peak deflection occurs at approximately $(t = 0.0025)$ for all three energy regimes, indicating that the time-to-peak is independent of the impact velocity. However, the magnitude of the deflection scales with the impact energy

- The $5\,J$ $(1\,ms^{-1})$ case results in a maximum indentation of $1.3692\,mm$.
- The $20\,J$ $(2\,ms^{-1})$ case results in a maximum indentation of $2.6146\,mm$.
- The $40\,J$ $(3\,ms^{-1})$ case results in a maximum indentation of $3.75215\,mm$.

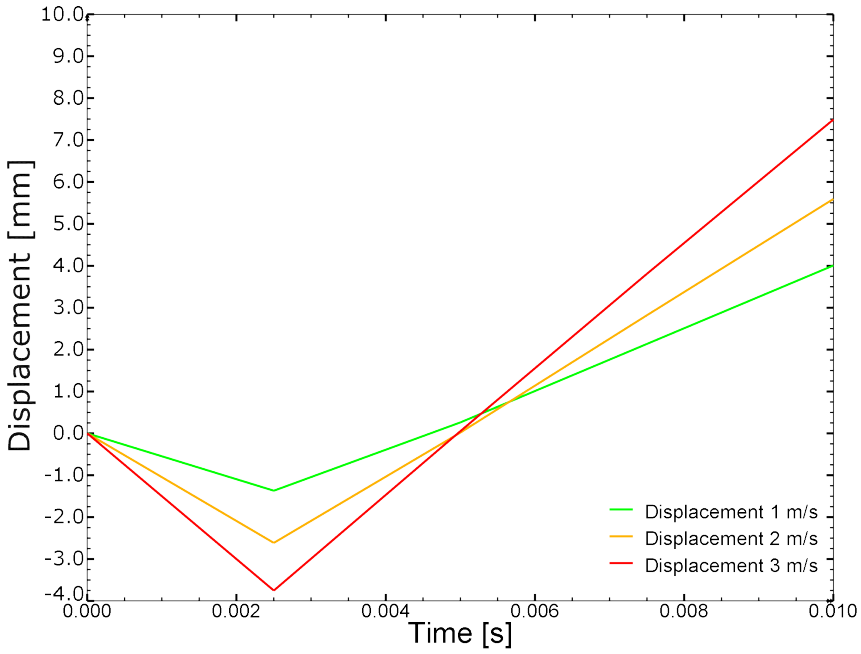

Figure 104. Displacement Comparison

Following the point of maximum deflection $(t > 0.0025)$, the displacement values become positive and increase linearly. This linear increase represents the flight path of the impactor as it rebounds away from the door surface. The steeper slope of the $40\,J$ curve compared to the $5\,J$ curve confirms that the impactor retains a higher residual velocity after separation, consistent with the kinematic data presented in Section 5.2.2

5.3 Damage and Failure Analysis

This section interrogates the comprehensive damage morphology of the skin-stringer assembly. Hashin damage criterion is employed to capture intralaminar failure (matrix and fibre) and quads damage criterion to predict cohesive debonding. To quantify the extent of structural degradation, the field output variables defined in Table 5.2 were extracted from the simulation results at the point of maximum damage accumulation ($t = 0.05$).

The analysis indicates that matrix and shear failure modes (DAMAGEMT, DAMAGEMC, DAMAGESHR) represent the dominant energy absorption mechanisms, exhibiting significantly higher failure indices compared to fibre fracture

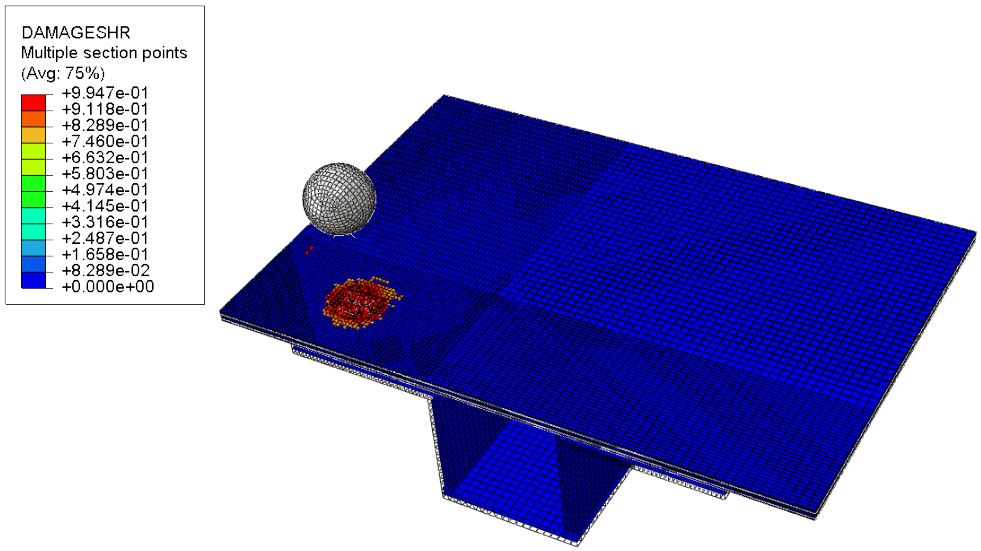

Figure 105. Isometric View of the Localised Damage Zone ($40\ J$ Impact Case)

Field Variable	Definition	Targeted Failure Mechanism
DAMAGEFT	Fibre Tensile Damage	Fracture of carbon fibres under tension (Penetration/Hole formation).
DAMAGEMT	Matrix Tensile Damage	Resin cracking due to bending (Back-face splitting).
DAMAGEMC	Matrix Compressive Damage	Resin crushing due to contact pressure (Front-face indentation).
DAMAGESHR	Shear Matrix Damage	Matrix failure driven by transverse shear stresses (Cone cracking).
CSDMG	Cohesive Damage	Delamination of the stringer flange (Debonding).

Table 5.2: Definition of Field Output Variable for Damage Evaluation

5.3.1 Intralaminar Matrix and Shear Failure

The primary failure mode observed across all impact energies is the degradation of the resin matrix. This is evaluated through a combination of matrix tensile (DAMAGEMT), compressive (DAMAGEMC), and shear (DAMAGESHR) criteria.

The morphological evolution of tensile matrix damage on the distal (rear) face reveals a clear dependency on impact energy. In the $5\,J$ $(1\,ms^{-1})$ case, the rear face remains intact, exhibiting no observable damage. The $20\,J$ $(2\,ms^{-1})$ case displays minimal damage initiation, indicating the onset of matrix micro-cracking. However, the $40\,J$ $(3\,ms^{-1})$ case exhibits catastrophic element failure.

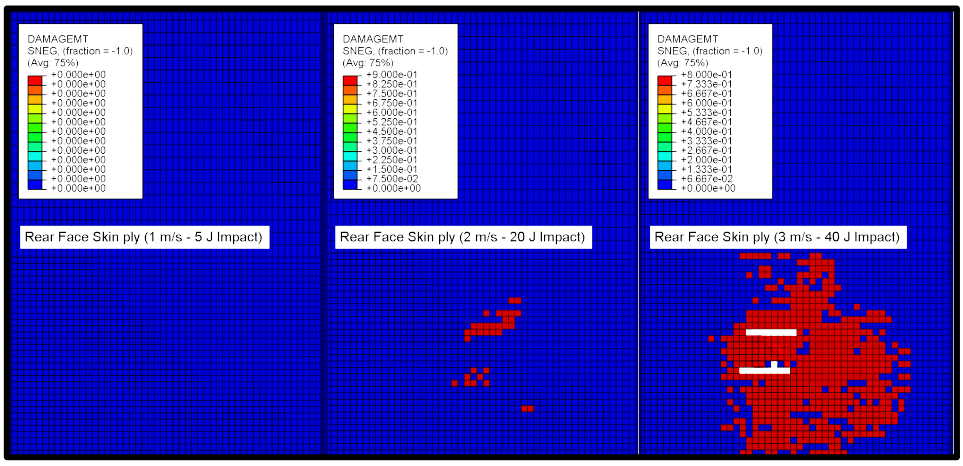

Figure 106. Evolution of Matrix Tensile Damage (DAMAGEMT) on the Last Ply (Rear Face) Impact Zone Across Impact Energies

By contrast, DAMAGEMC on the front face remains localised to the contact patch across all cases, governed purely by Hertzian contact pressure.

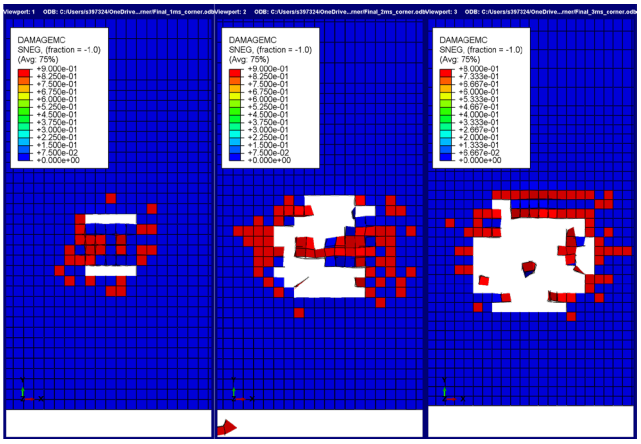

Figure 107. Evolution of Matrix Compressive Damage (DAMAGEMC) on the Front Face Impact Zone Across Impact Energies

Transverse shear damage (DAMAGESHR) provides critical insight into the depth of failure penetration. As illustrated in Figure 108, the $5\,J$ impact results in partial penetration, affecting only the upper half laminate layers. The $20\,J$ and $40\,J$ cases, however, exhibit through-thickness shear bands. Crucially, in the $40\,J$ scenario, this shear damage extends beyond the skin and propagates into the stringer flange. This bridging effect confirms that high-energy impacts transfer sufficient load to compromise the substructure, creating a direct damage path from the skin into the stiffener.

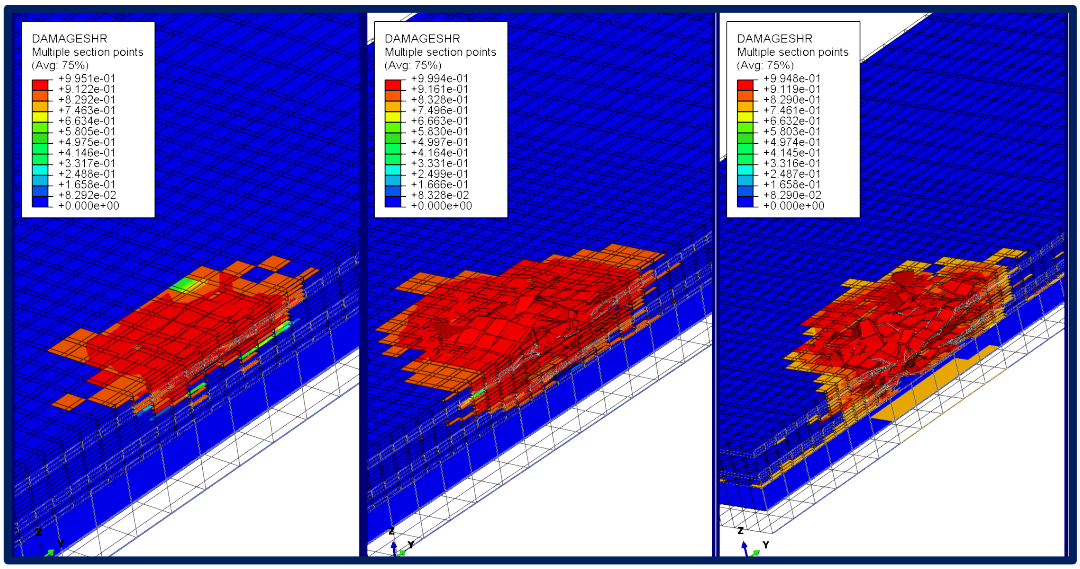

Figure 108. Cross-sectional 'Cut View' DAMAGESHR Penetration Depth Across Impact Energies

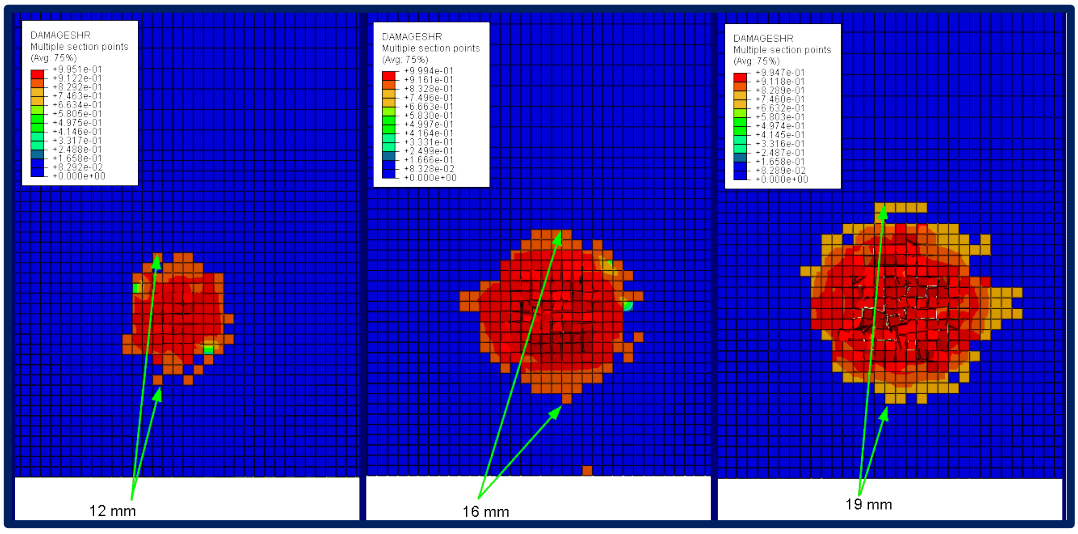

Figure 109. Front Face DAMAGESHR Impact Zone Length Across Impact Energies

5.3.2 Interlaminar Interface Integrity

The integrity of the bond between the fuselage skin and the stringer is evaluated using the cohesive damage (CSDMG) field output request. This variable identifies regions where the adhesive interface has degraded or delaminated.

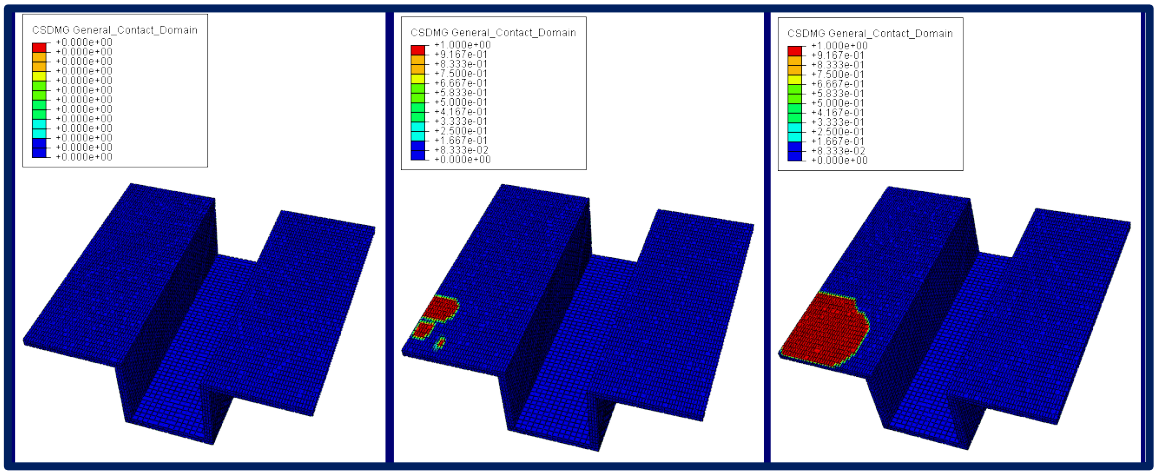

Figure 110. Top-down view of the Skin-Stringer Interface showing CSDMG distribution

A distinct failure pattern emerges at the interface edges. In the $5\,J$ $(1\,ms^{-1})$ case, the interface remains pristine with no recorded damage. The $20\,J$ $(2\,ms^{-1})$ case exhibits moderate damage initiation, while the $40\,J$ $(3\,ms^{-1})$ case shows extensive delamination.

Notably, the cohesive damage initiates at the pinned edges of the stringer flange rather than solely at the impact centre. This suggests that the failure is driven by local buckling or peeling stresses arising from the stiffness mismatch between the compliant skin and the rigid stringer. As the skin bends, the "pinned" boundary condition at the flange edge induces a stress concentration that initiates the debonding process, effectively decoupling the stringer from the skin.

5.3.3 Fibre Fracture and Penetration Depth

Unlike the matrix damage discussed in Section 5.3.1, which exhibits widespread propagation, fibre fracture is characterised by high localisation.

Figure 111 presents the through-thickness distribution of fibre tensile damage. A defining characteristic observed across all energy regimes is the limited radial expansion of the damage zone. The fibre failure remains confined to the immediate footprint of the impactor, with negligible spreading to the surrounding material

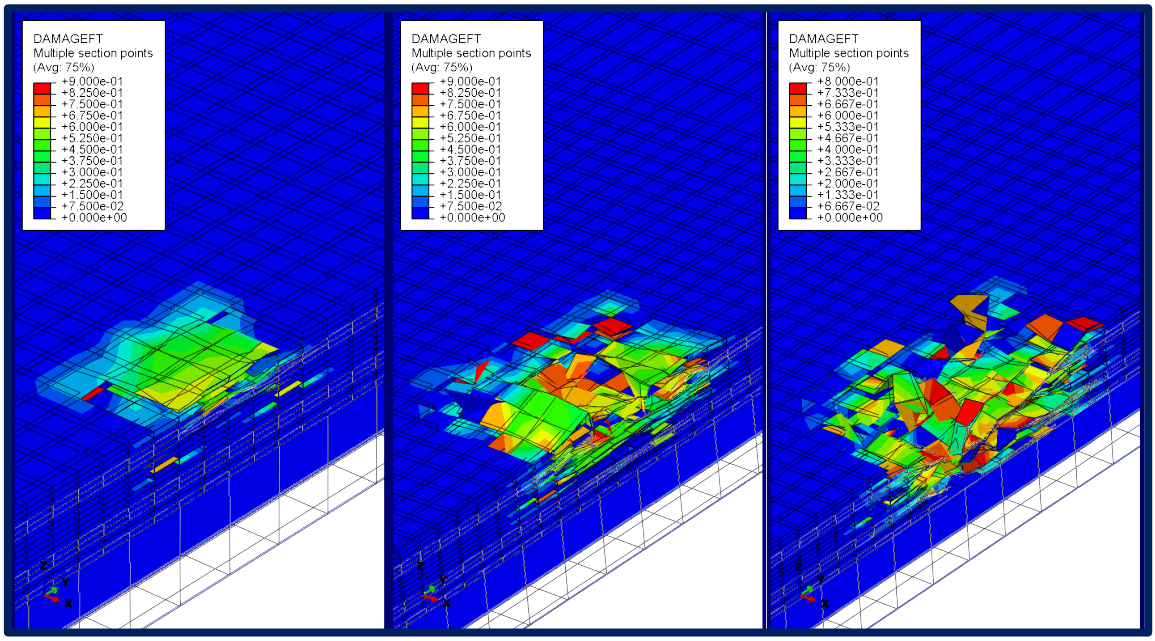

Figure 111. Cross-sectional 'Cut View' comparing DAMAGEFT Penetration Depth Across Impact Energies

This characteristic behaviour can be attributed to the high specific strength of the carbon reinforcement; whereas the matrix distributes energy through broad shear cracking, the fibres fail only when localised strains exceed their ultimate tensile limit, resulting in a concentrated "pinpoint" failure mode.

Despite the limited damage area, the cross-sectional analysis reveals significant differences in penetration depth, serving as a clearer indicator of structural compromise than damage area alone.

The $5\,J$ $(1\,ms^{-1})$ case, fibre damage initiation is detected up to **Ply 9**. While this indicates that internal stresses at the mid-plane exceeded the initiation threshold, the damage volume is microscopic and discontinuous

The $20\,J$ $(2\,ms^{-1})$ case exhibits a critical deepening of the failure path, with damage propagation detected up to **Ply 15** (the penultimate layer). While the final ply remained intact, preventing full penetration, the internal load-bearing column has been effectively severed through 93% of the laminate thickness

The $40\,J$ $(3ms^{-1})$ case demonstrates fibre rupture at certain elements of the composite ply throughout the thickness.

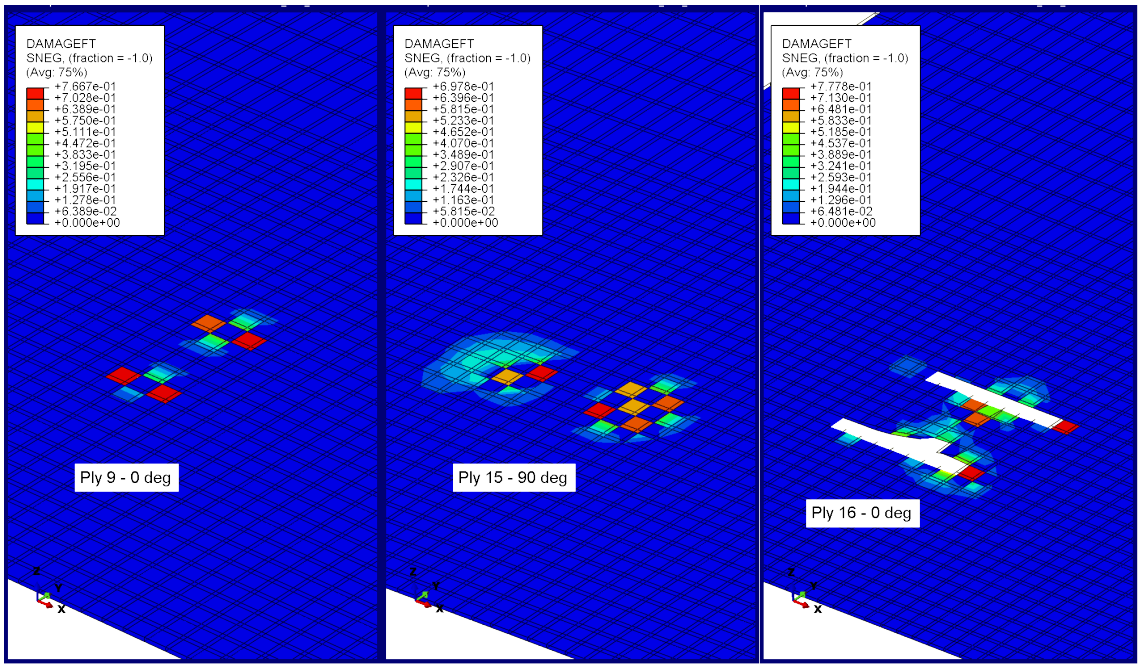

Figure 112. Ply View Comparing DAMAGEFT Penetration Depth Across Impact Energies

6 Discussion

The primary objective of this study was to evaluate the impact resistance and damage tolerance of a CFRP cargo door under low velocity impact conditions. By correlating the kinematic response presented in Section 5.2 with the internal damage morphology characterised in Section 5.3, this chapter harmonises the findings to determine the structural limits of the design.

The analysis is framed within the framework of EASA CS-25 certification requirements. These regulations mandate that aircraft primary structures must tolerate BVID without catastrophic failure under ultimate load. This discussion evaluates the simulation results against these damage tolerance benchmarks, interprets the hierarchy of failure mechanisms, and critiques the fidelity of the finite element modelling approach. A particular focus is placed on the use of continuum shell elements and their ability to capture through-thickness shear propagation.

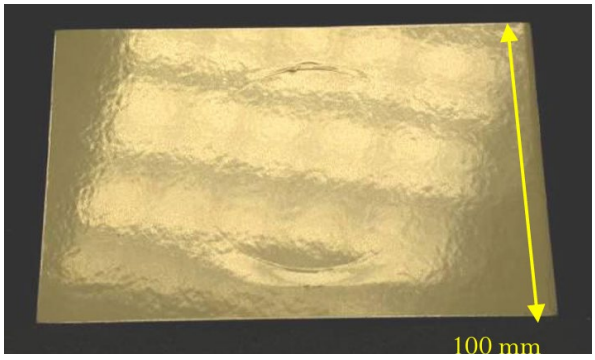

Figure 113. $30\,J$ Experimental Impact on 17 Ply Painted Laminate (84)

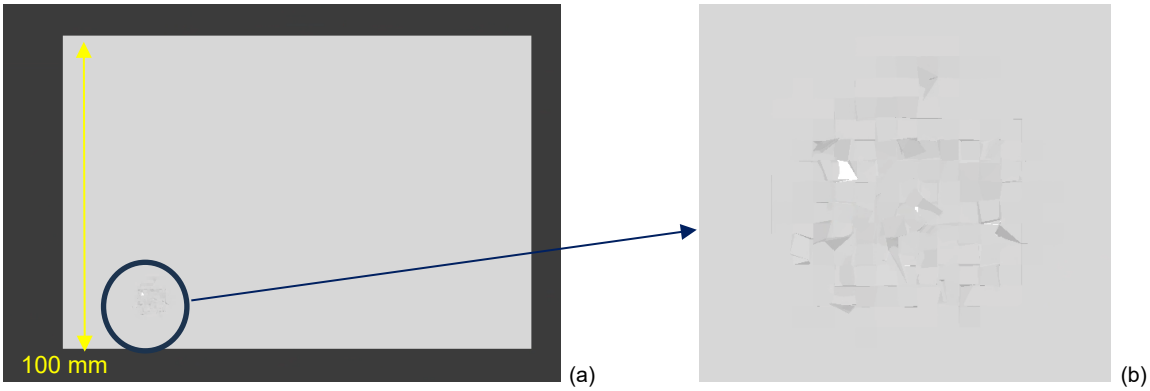

Figure 114. $40\,J$ Impact Simulation on 16 Ply Painted Laminate (a) Top-View (b) Impact Zone

6.1 Analysis of Failure Mechanisms

The failure progression observed in the cargo door skin follows a distinct hierarchy, governed by the strain energy thresholds of the constituent materials. Unlike metallic structures, which dissipate energy through isotropic plastic deformation, the carbon fibre reinforced polymer (CFRP) assembly exhibits a complex, multi-stage failure mode. This sequence advances from intralaminar matrix cracking to interlaminar decohesion, and finally to catastrophic fibre fracture. The simulation results confirm that the damage morphology is not governed by a single mechanism but rather by the coupling of local contact stresses and global flexural strains

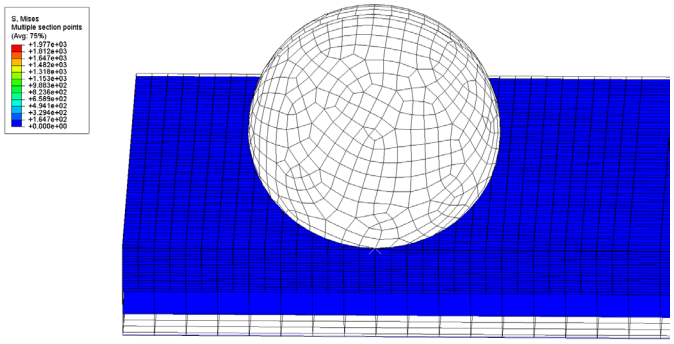

Figure 115. 5 J Impact Loading Phase Cut View

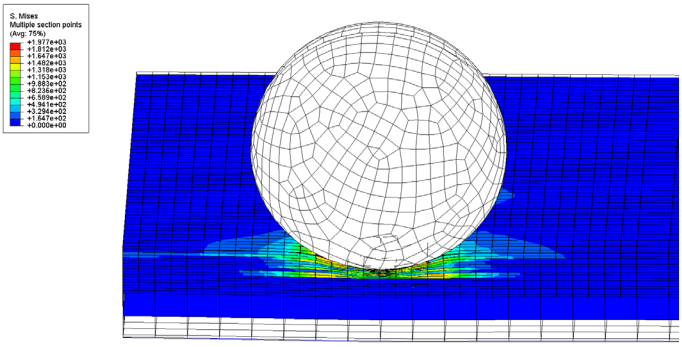

Figure 116. 5 J Impact Maximum Penetration Cut View

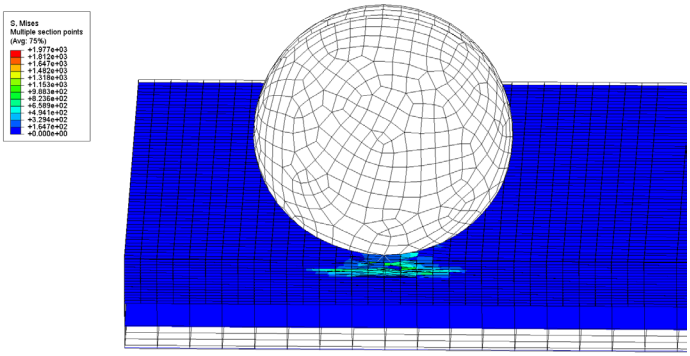

Figure 117. 5 J Impact Rebound Phase Cut View

6.1.1 Matrix Initiation and Invisible Micro-Cracking

The simulation results for the $5\,J$ $(1\,ms^{-1})$ regime challenge the operational assumption that low-energy impacts are structurally benign. Although the tensile matrix damage (DAMAGEMT) on the distal face remained negligible, the through-thickness shear analysis confirmed that damage initiation had occurred. The transverse shear stresses generated by the impactor contact induced matrix micro-cracking that penetrated the first 14 plies of the laminate. This depth corresponds to approximately 40% of the skin thickness.

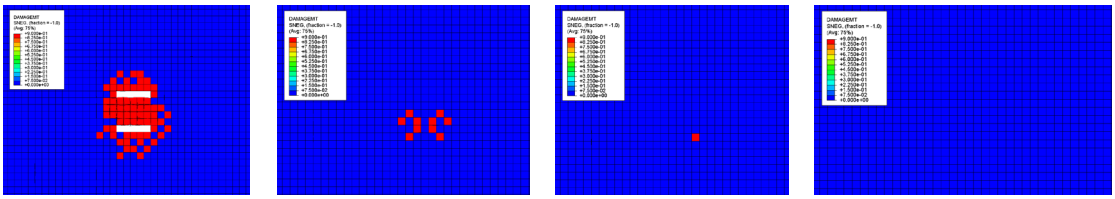

(a) (b) (c) (d)

Figure 118. Top View of Tensile Matrix Damage for $5\,J$
(a) Ply 1 - Top Face (b) Ply 9 (c) Ply 13 (d) Ply 14

However, from a certification perspective, this "invisible" damage is critical. It represents a latent defect; although it does not compromise the immediate static strength of the door, it creates initiation sites for fatigue crack growth. Under the cyclic pressurisation loads inherent to a cargo aircraft, these micro-cracks serve as stress concentrators, potentially leading to widespread matrix degradation over the service life of the airframe.

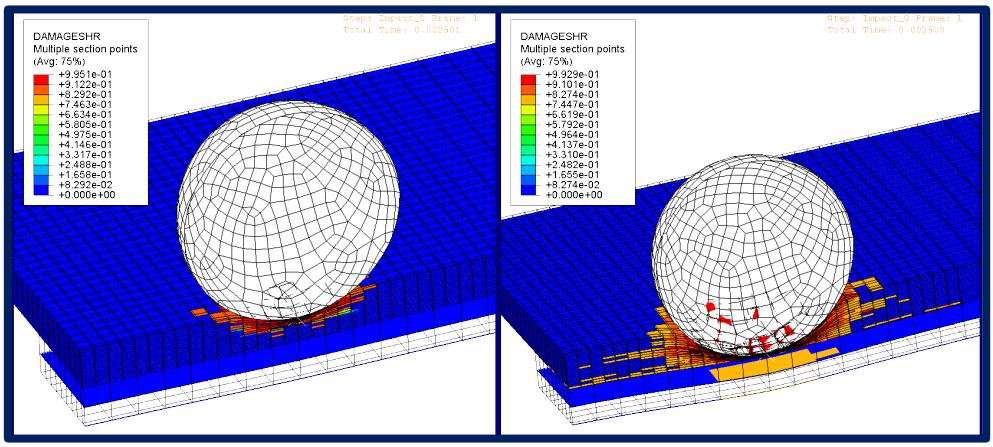

Figure 119. Cross-sectional View of Shear Damage (DAMAGESHR) Comparing the $5\,J$ Partial Penetration vs. $40\,J$ Full Penetration

6.1.2 The Mechanics of Barely Visible impact Damage (BVID)

The $20\,J$ impact case serves as the defining example of BVID, a condition identified by EASA CS-25 as the critical design driver for composite primary structures. The analysis captures a dangerous decoupling of internal and external damage states.

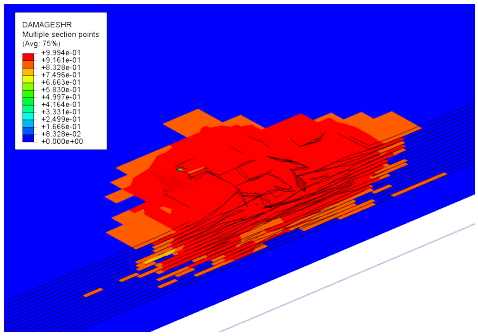

Figure 120. Cross-sectional View of $20\,J$ Impact Simulation Shear Damage (DAMAGESHR)

Externally, the surface exhibits a minor indentation depth. In an operational environment, where the cargo door is coated with primer and livery paint, such a defect would be indistinguishable from surface irregularities, likely escaping detection during standard visual ramp inspections. Internally, however, the structural compromise is severe. The simulation confirms that fibre damage initiates as deep as the 15th ply (the penultimate layer).

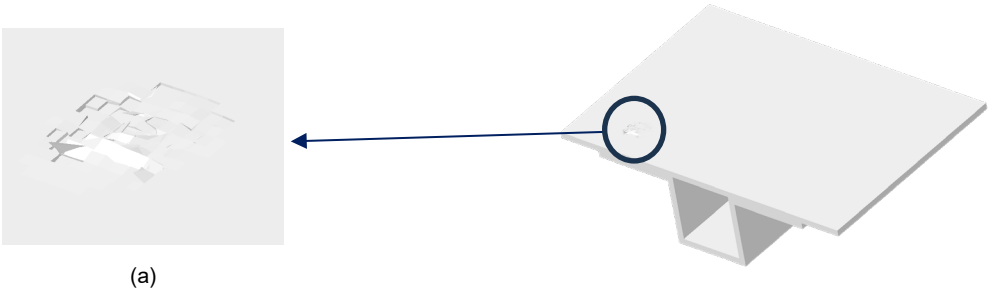

(a) (b)

Figure 121. $20\,J$ Impact Simulation Painted Assembly (a) Impact Zone (b) Isometric View

This phenomenon creates a false positive safety assessment. The lack of fibre fracture on the surface suggests structural integrity, yet the internal load-bearing column has been effectively severed through 93% of the laminate thickness. This finding validates the necessity for the stringent "damage tolerance" requirements in aerospace design, confirming that the residual strength of the door cannot be assessed by visual means alone

6.1.3 Interlaminar Coupling and Stringer Decohesion

A principal finding of this study is the complex interaction between the local impact loads and the global boundary conditions of the stringer. The cohesive damage analysis (CSDMG) reveals that delamination does not propagate from a single initiation point but rather develops through a dual-zone failure mechanism.

The $20\,J$ $(2\,ms^{-1})$ case serves as the critical evidence for this behaviour. As illustrated in the simulation results, two distinct and unconnected regions of cohesive failure are observed simultaneously:

1. **Impact zone failure:** A localised delamination patch forms directly beneath the impactor. This is driven by the immediate through-thickness shear and compressive forces crushing the skin onto the stringer flange.
2. **Pinned-edge buckling:** A secondary, separate delamination zone appears at the outer "pinned" edge of the stringer flange. This failure is driven by the global deformation of the panel. As the impactor strikes the unsupported area of the skin, the panel bends significantly. However, the stringer edge is geometrically constrained (pinned). This constraint forces the flange edge to buckle and peel upwards, initiating Mode I (opening) fracture remote from the actual impact site

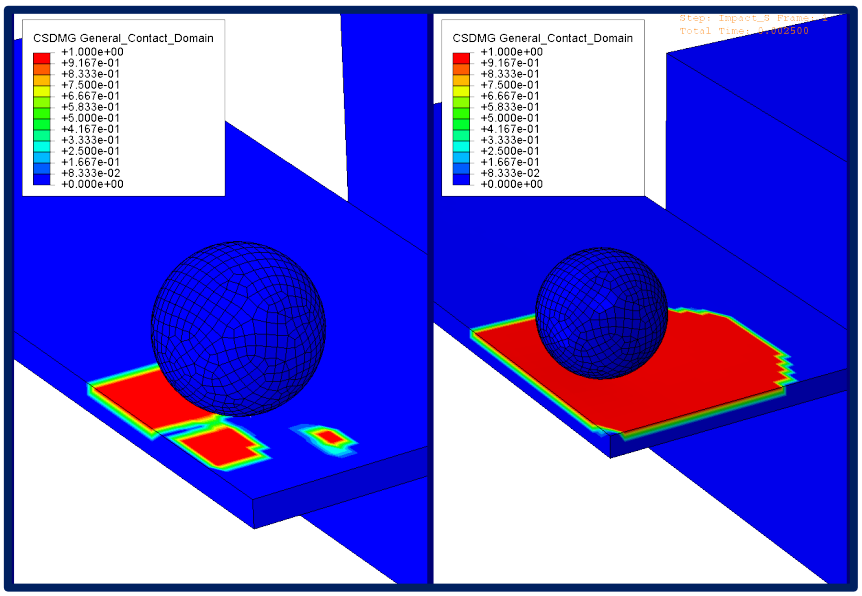

Figure 122. Comparative View of $20\,J$ Showing Two Separate Failure Zones vs. $40\,J$ Showing Merged Failure

In the $40\ J\ (3\ ms^{-1})$ regime, these two distinct failure zones coalesce. The increased energy input drives the edge-buckling delamination inwards and the impact-zone delamination outwards until they merge into a single, catastrophic failure surface. This confirms that the stringer flange is attacked from both sides: locally by the projectile and remotely by the bending strains.

The investigation into the $5\ J\ (1\ ms^{-1})$ energy regime exposes a critical finding. While the skin-stringer interface surface shows no permanent indentation, the internal cohesive damage (CSDMG) analysis reveals interlaminar decohesion propagating through the laminate stack **up to Ply 12**. This deep-seated failure confirms that the Hertzian contact pressure generated a transverse shear stress wave of sufficient magnitude to exceed the Mode II interlaminar fracture toughness (G_{II_c}) at the mid-plane, even in the absence of fibre fracture.

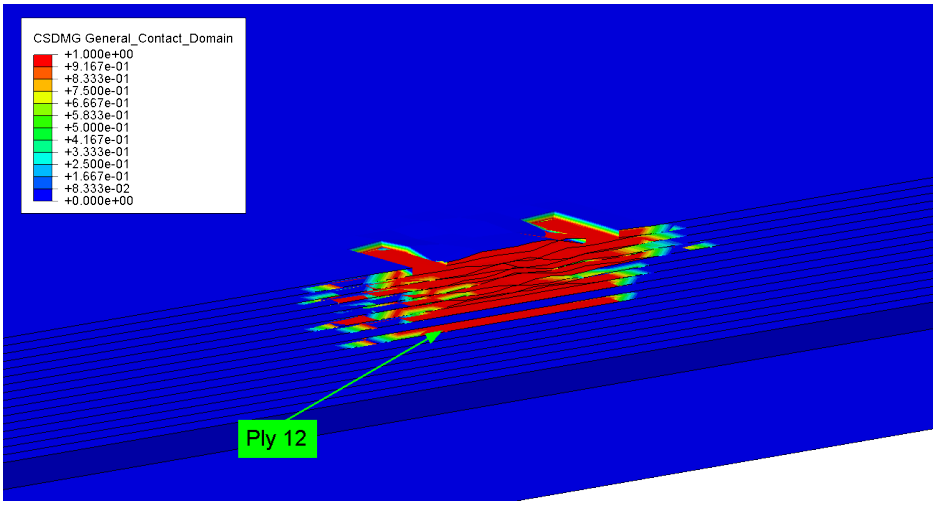

Figure 123. Cross-sectional View of the $5\ J$ Impact Showing CSDMG delamination

The minimal indentation on the outer surface is insufficient for reliable visual detection, effectively masking the internal failure up to Ply 12. Consequently, standard visual inspection protocols would be inadequate for determining damage. Reliable detection necessitates volumetric non-destructive testing (NDT), such as ultrasonic C-scanning, to identify the discontinuity. Without such intervention, the concealed delamination acts as a stress concentrator under cyclic pressurisation, creating a nucleation site for fatigue propagation during service

6.1.4 Stringer Interlaminar Failure

To fully characterise the structural compromise, the analysis must extend beyond the skin and interface to examine the stiffening substructure itself. A critical differentiation in failure modes is observed when comparing the stringer integrity across the energy spectrum.

In the $\mathbf{5}\,\boldsymbol{J}\,(\boldsymbol{ms^{-1}})$ regime, the stringer remains structurally pristine. Interrogation of the Hashin failure indices within the stringer plies reveals no element degradation. This confirms that at low energies, the stringer reinforced skin successfully absorbs and distributes the contact loads via flexure without transferring critical stresses to the substructure

However, the $\mathbf{20}\,\boldsymbol{J}\,(\mathbf{2}\,\boldsymbol{ms^{-1}})$ and $\mathbf{40}\,\boldsymbol{J}\,(\mathbf{3}\,\boldsymbol{ms^{-1}})$ cases exhibit a fundamental shift in load path mechanics. The simulation reveals that intralaminar damage has initiated within the stringer flange. Specifically, matrix cracking and shear failure are observed. This is not merely a surface phenomenon. The damage is coincident with the zones of cohesive delamination identified in Section 6.1.3

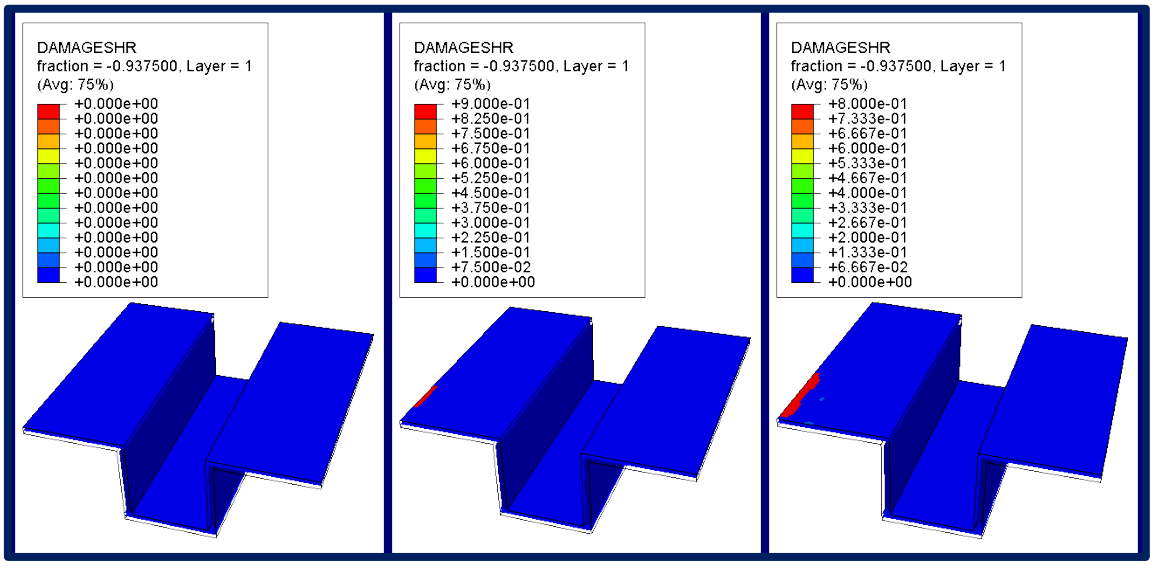

Figure 124. View of Stringer-only showing Shear Damage (DAMAGESHR) Across Impact Energies

In addition to that, the $20J$ $(2\,ms^{-1})$ case exhibits a complex, depth-dependent failure mechanism within the stringer laminate (16 plies total).

- **Lower Plies (1–8):** In the bottom half of the stack (closest to the skin interface), shear damage (DAMAGESHR) is concentrated directly above the impact zone. This indicates that these plies are acting as a direct reinforcement, absorbing the localized contact stress transferred from the skin.
- **Upper Plies (9–16):** As the analysis moves to the mid-plane and above, the damage morphology shifts. The failure disappears from the impact centre and re-emerges at the pinned edges of the flange.

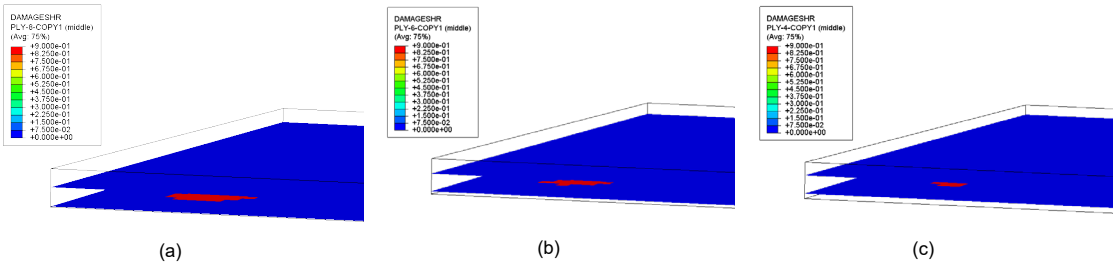

Figure 125. $20\,J$ Case Shear Damage on Lower Plies (1-8) (a) PLY 1 (b) PLY 3 (c) PLY 5

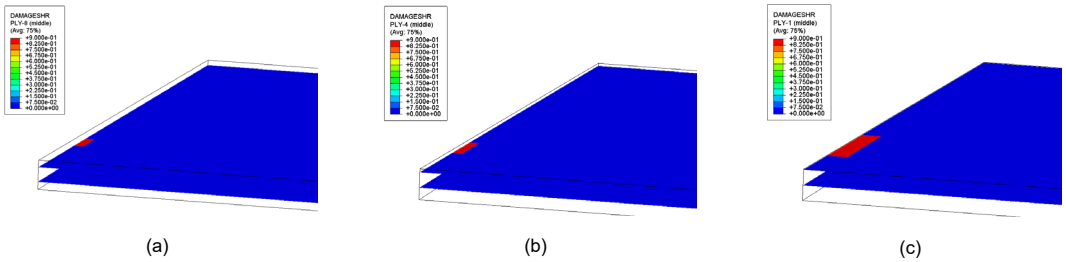

Figure 126. $20\,J$ Case Shear Damage on Upper Plies (9-16) (a) PLY 9 (b) PLY 13 (c) PLY 16

This transition suggests that the stringer's mechanical role changes through its thickness. The inner plies fail due to local contact pressure, while the outer plies fail due to global bending and the kinematic constraint at the pinned boundary.

In contrast, the $40\ J\ (3\ ms^{-1})$ case demonstrates a coalescence of these mechanisms. The shear damage is no longer separated by ply depth but is distributed across both the impact zone and the pinned edges throughout all 16 plies. The high energy input has overwhelmed both the local indentation resistance and the global boundary strength. This results in a "mixed" damage state where the stringer is compromised in its entirety, effectively severing the longitudinal load path of the cargo door.

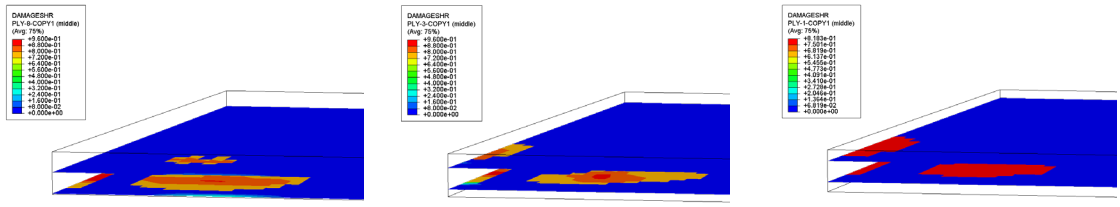

(a) (b) (c)

Figure 127. $30\ J$ Case Shear Damage on Lower Plies (1-8) (a) PLY 1 (b) PLY 6 (c) PLY 8

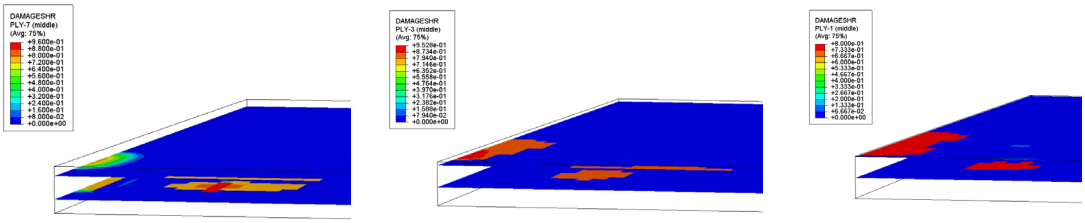

(a) (b) (c)

Figure 128. $30\ J$ Case Shear Damage on Upper Plies (9-16) (a) PLY 10 (b) PLY 13 (c) PLY 16

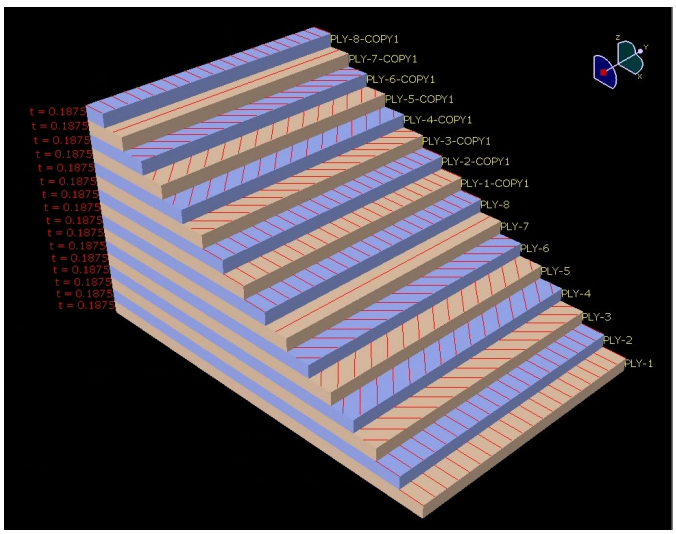

Figure 129. Ply Stack Plot for Stringer Composite Layup

6.2 Structural Performance Evaluation

This section evaluates the overall performance of the cargo door design by analysing its energy absorption characteristics and load bearing capacity. The assessment relies on the global history output variables extracted from the simulation. These are damage dissipation energy (ALLDMD) and elastic strain energy (ALLSE).

6.2.1 Energy Absorption Efficiency

The structural efficiency of the composite design is determined by its ability to store energy elastically versus dissipating it through irreversible damage.

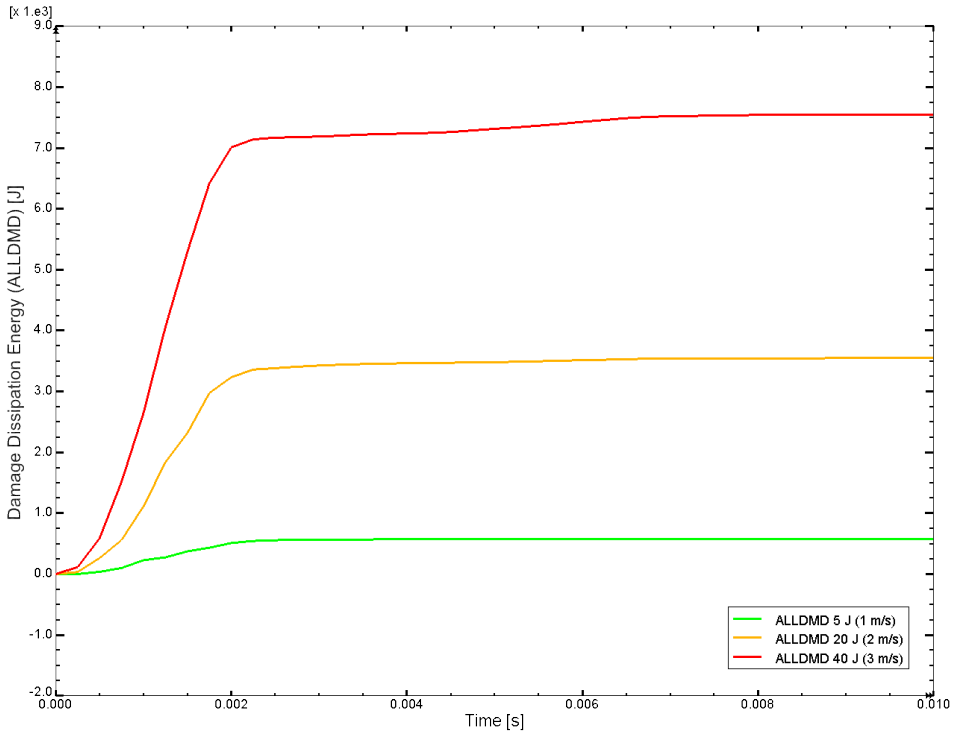

Figure 130. Comparing Damage Dissipation Energy (ALLDMD) Across Impact Energies

As illustrated in Figure 130, the $5\,J\ (1\,ms^{-1})$ impact exhibits negligible damage dissipation. The ALLDMD curve remains near zero throughout the event. This confirms that the impact energy was almost entirely converted into elastic strain energy and subsequently returned as kinetic energy during the rebound phase. Consequently, the structural response is classified as fully elastic.

In contrast, the $40\,J\ (3\,ms^{-1})$ case exhibits a rapid, step change increase in ALLDMD. Approximately $7\,J$ of energy is permanently dissipated within the first 2 milliseconds of contact. It consumes the impact kinetic energy through the creation of widespread matrix cracks and fibre fracture surfaces.

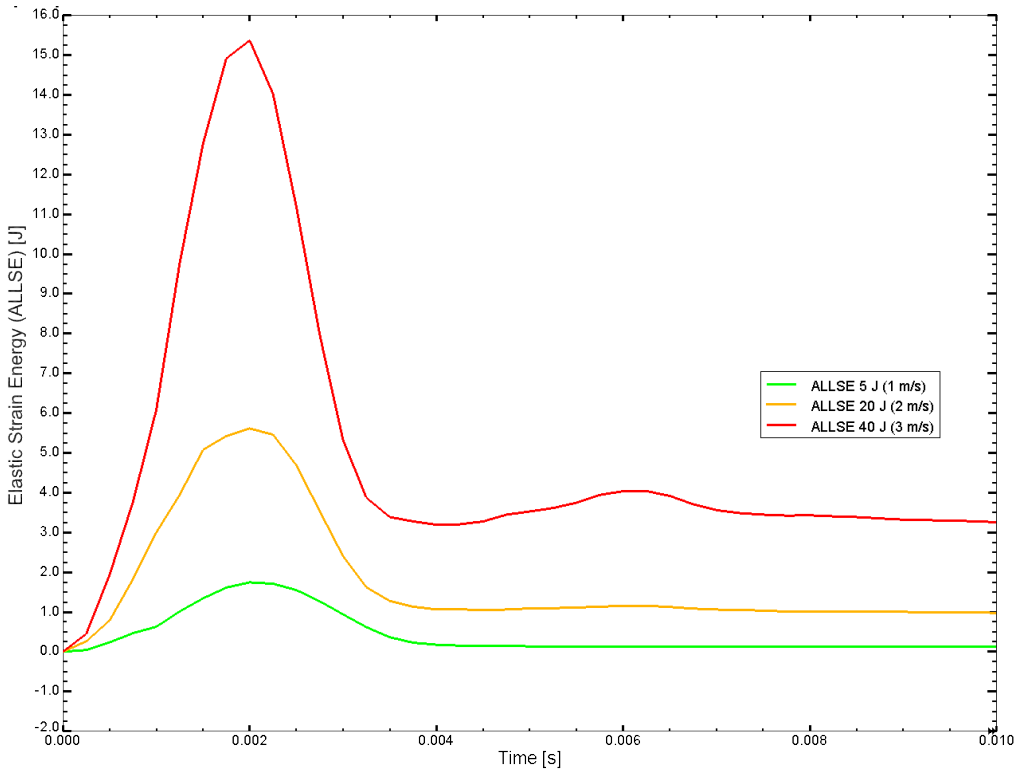

Figure 131.Comparing Elastic Strain Energy (ALLSE) Across Impact Energies

This behaviour is further elucidated by the ALLSE history presented in Figure 131. The $5\,J\ (1\,ms^{-1})$ case exhibits a near perfect parabolic response. The energy rises to a peak and returns to approximately zero after the rebound. This indicates a complete release of stored strain energy and confirms a fully elastic structural recovery.

In contrast, both higher energy cases exhibit significant residual strain energy. The $20\,J\ (2\,ms^{-1})$ case does not return to zero but settles at a residual plateau of approximately $1\,J$. This indicates that 5% of the impact energy remains trapped within the structure. This stored energy corresponds to permanent sub-surface deformation.

The $40\,J\ (3\,ms^{-1})$ case retains a much higher residual energy of approximately $3.5\,J$. The distinct oscillation observed in the post-impact phase suggests dynamic relaxation of the damaged constituent parts. The inability of the structure to release this energy confirms that the door has undergone irreversible geometric changes. It effectively proves that for impacts above $20\,J$, the cargo door behaves as a plastic system rather than an elastic shell

6.2.2 Ultimate Load Capacity

The peak contact force sustained by the panel serves as the definitive metric for its ultimate static strength under transverse loading.

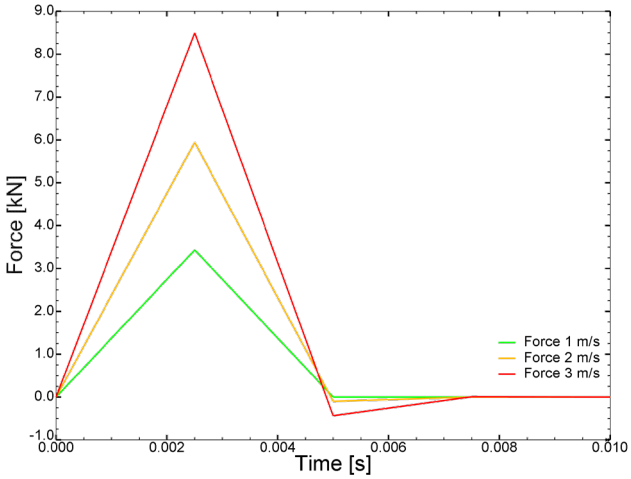

Figure 132. Impact Force Comparison

The impact force history reveals a clear limit state for the design. As shown in Figure 132, the peak force increases linearly with velocity. It reaches $3.5\ kN$ at $1\ ms^{-1}$ and $6.0\ kN$ at $2\ ms^{-1}$. Crucially, the $40\ J\ (3\ ms^{-1})$ case reaches a maximum of $8.5\ kN$ before precipitating a sharp drop.

This $8.5\ kN$ value represents the Critical Load Bearing Capacity of the skin-stringer assembly. Beyond this threshold, the local stiffness collapses due to the combined fibre fracture and stringer delamination discussed in Section 6.1. Consequently, $8.5\ kN$ is defined as the ultimate static design load for this specific cargo door configuration. Any dynamic event generating a reaction force exceeding this limit will result in immediate perforation.

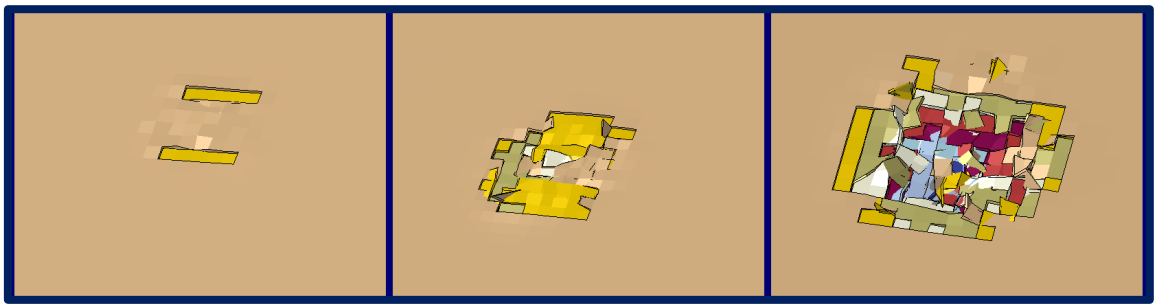

Figure 133. Top Face View Across Impact Energies $5\ J$, $20\ J$, and $40\ J$

6.2.3 Post-Impact Stability and Permanent Set

The final performance metric evaluates the geometric excursion of the assembly during the impact event. This magnitude of deformation is directly linked to the initiation of the stringer decoupling discussed in Section 6.1.

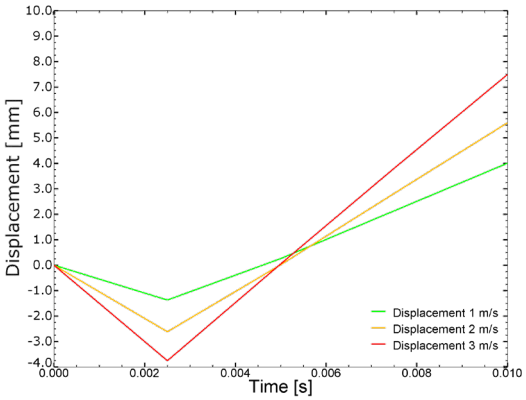

Figure 134. Displacement Comparison

The 2.61 mm deflection observed in the $20\,J$ case is particularly critical. While this depth was insufficient to cause skin perforation, it induced a local curvature severe enough to trigger the "dual zone" stringer failure. The bending strains associated with a $2.61\,mm$ excursion exceeded the peel strength of the adhesive interface at the pinned stringer edge

This confirms that the $2.6\,mm$ deflection threshold represents the geometric stability limit of the design. Beyond this point, even if the skin remains intact, the stiffening substructure detaches. This loss of constraint renders the door susceptible to "pillow buckling" under operational pressurisation loads, as the delaminated stringer can no longer enforce the original loft of the skin

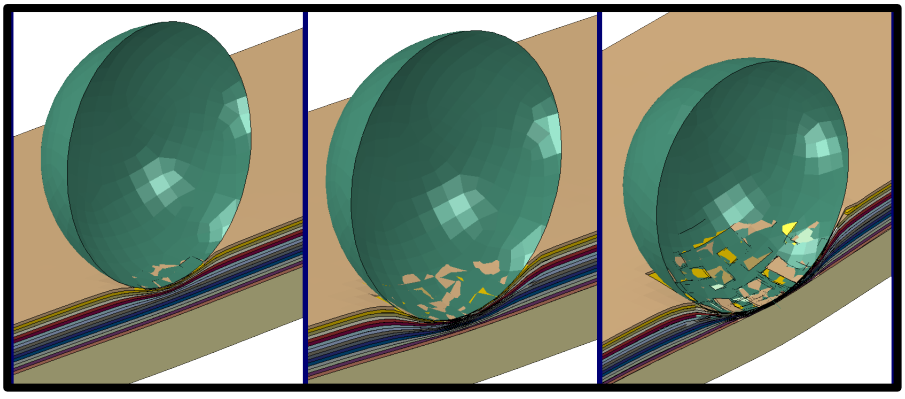

Figure 135. Cut View Across Impact Energies $5\,J$, $20\,J$, and $40\,J$

6.3 Critique of Modelling Approach

The predictive accuracy of any finite element analysis is intrinsically linked to the assumptions made during the discretisation of the physical problem. While the current model has successfully elucidated the primary failure mechanisms of the MDCD, it is imperative to rigorously evaluate the limitations of the methodology. This section critiques the simplifications regarding geometric idealisation, numerical stability controls, and the scope of the post-impact assessment.

6.3.1 Geometric Idealisation and Boundary Effects

A primary limitation of this study is the reduction of the full cargo door assembly to a representative "skin-stringer" sub-component. The model isolates the impact zone. It assumes that the kinetic energy is dissipated entirely within this local interface.

In the physical structure, the door is a complex assembly reinforced by shear clips, C-frames, and intercostals. These components provide significant global damping and facilitate load redistribution. By omitting these structural features, the model likely underestimates the global flexural stiffness. This forces the local skin-stringer interface to absorb a higher fraction of the strain energy than would occur in a full-scale test. While this approach yields a conservative prediction for local damage initiation (BVID), it precludes the assessment of secondary failure modes, such as shear clip detachment or frame buckling, which may propagate away from the immediate impact site at higher energy impacts.

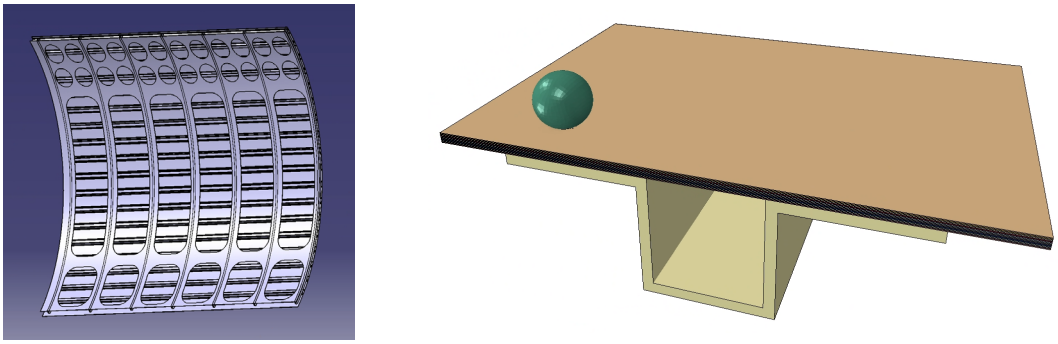

Figure 136. Development of FEA Model from 3D Cargo Door Model

6.3.2 Numerical Stability and Element Fidelity

The use of an explicit dynamic solver (Abaqus/Explicit) necessitates specific numerical controls to maintain computational stability. Two critical compromises were employed to manage the solution time and preventing solver divergence:

1. **Mass Scaling:** To prevent the stable time increment from diminishing to an infeasible level, semi-automatic mass scaling was utilised. While this technique accelerates the simulation, it artificially increases the nodal inertia. Strict controls were implemented to ensure the added mass remained below 5% of the physical mass to minimise dynamic artifacts.
2. **Maximum Degradation and Element Deletion:** For the high-energy $40\ J$ $(3\ ms^{-1})$ case, excessive element distortion posed a significant risk to the solver stability. To mitigate this, a Maximum Degradation (MAXDEGRAD) criterion was enforced within the damage evolution law. This parameter instructed the solver to delete elements once their stiffness degraded beyond a critical threshold (0.9), effectively removing highly distorted elements from the calculation before they could cause a negative volume error or a time increment collapse. While this method is essential for simulation completion, it introduces a mesh dependency. The macroscopic fracture path is effectively discretised by the element size rather than the physical crack propagation energy.

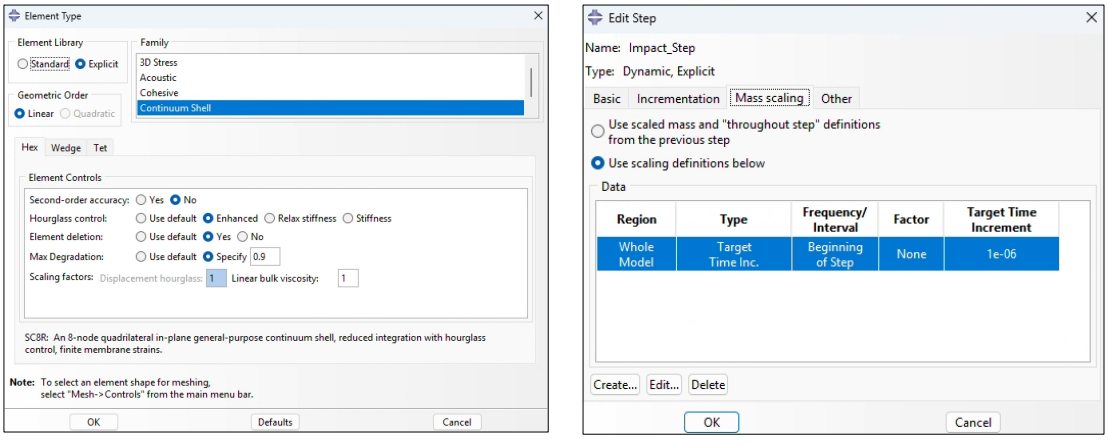

Figure 137. Max Degradation and Mass Scaling Employed for Explicit Simulation

6.3.3 Limitations of Residual Strength Assessment

The scope of this study is bounded by the assessment of damage tolerance (structural integrity) rather than the residual load-bearing capacity (residual strength). In a comprehensive certification workflow, the dynamic impact simulation would typically be followed by a static "Compression After Impact" (CAI) analysis, adhering to established standards such as ASTM D7137 ("Standard Test Method for Compressive Residual Strength Properties of Damaged Polymer Matrix Composite Plates") (85).

Figure 138. ASTM D7137 Test Specimen and Fixture Assembly Overview (86)

This multi-step methodology was excluded due to the prohibitive computational cost associated with mapping damage states from an explicit solver to an implicit static environment. The transfer of degraded material properties, delamination interfaces, and deformed mesh geometries into a static simulation frequently results in severe convergence difficulties. Consequently, this study quantifies the extent of the damage but does not numerically predict the reduction in the ultimate static strength of the door. Future work should prioritise a seamless co-simulation approach to quantify the precise knockdown factor associated with the observed $20\,J$ and $40\,J$ damage states relative to the pristine baseline.

6.4 Implications of Design Improvement

The numerical results presented in Section 5 and 6 provide critical insights into the vulnerability of composite airframe structures. Beyond the raw data of stress and failure indices, the simulation outcomes highlight significant risks regarding current ground handling procedures and the design of stiffened panels.

6.4.1 The Limits of Visual Inspection

The most concerning finding from this study is the disparity between internal damage and external visibility at the $20\,J$ impact energy level. The finite element analysis predicted the onset of significant interlaminar failure, particularly at the critical Ply 15 interface between the skin and the stringer. Despite this internal compromise, the external surface deformation remained minimal due to the elastic recovery properties of the carbon fibre reinforced polymer laminate.

Figure 139. Effect of Painted Aircraft Livery on Composite Visual Inspections (87)

In an operational environment, this creates a dangerous "latent defect" scenario. A $20\,J$ impact, which could easily result from a tool drop or a minor collision with a belt loader, might leave a surface indentation depth below the threshold of visual detection, especially when obscured by aircraft paint systems. Consequently, a cargo door could be visually inspected and cleared for flight while harbouring a compromised stringer bond. This latent damage would then be subjected to cyclic pressurisation loads, creating a high probability of damage propagation and fatigue failure over the service life of the airframe.

6.4.2 Recommendations for Maintenance Protocols

Given the confirmed existence of BVID thresholds in this design, reliance on visual inspection for post-incident assessment is statistically unreliable. The standard maintenance logic, which often dictates further inspection only if a dent exceeds a specific depth, is inadequate for this class of composite structure.

It is recommended that the aircraft maintenance manual (AMM) protocols for the main deck cargo door be revised. The findings of this research suggest that any reported contact with ground support equipment, regardless of visual evidence, should trigger a mandatory non-destructive testing (NDT) procedure.

Furthermore, future maintenance strategies should transition away from reactive tasks towards predictive **structural health monitoring** (SHM). By installing strain gauges or sensors at critical load paths during manufacturing, operators can move beyond reliance on ground staff reporting. These sensors could continuously monitor the airframe for transient impact events. If a strain spike exceeds the critical failure thresholds defined in this thesis (such as the $20\ J$ limit), the system would automatically trigger an inspection requirement. This eliminates human error and ensures that latent defects are identified before the aircraft returns to service.

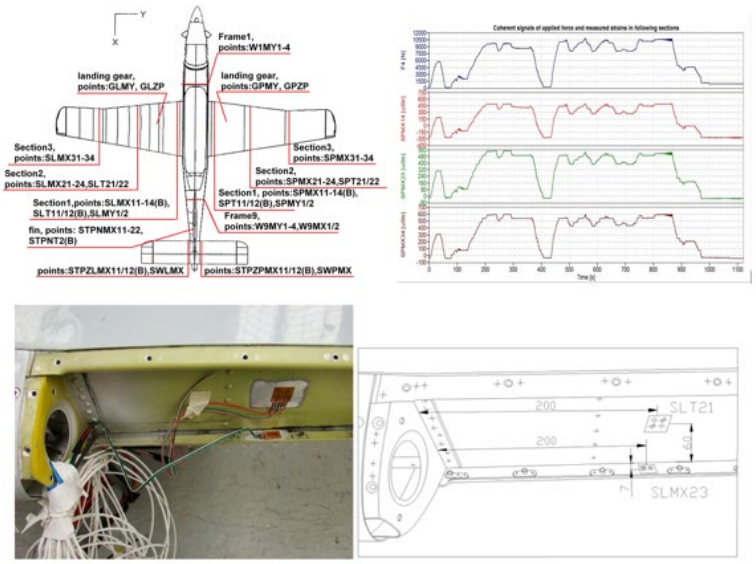

Figure 140. Strain Gauge Instalment example on PZL 130 Orlik for Loads Measurement at Critical Locations (88)

6.4.3 Design Optimisation and Future Principles

The structural analysis in Section 5.3.2 revealed a tendency for the stringer to debond at the free edge of the omega flange. This failure mode is driven by the abrupt change in stiffness at the transition between the monolithic skin and the reinforced stringer foot. This stiffness mismatch generates high localised peel stresses under impact loading which accelerates the delamination process.

To mitigate this vulnerability, a mechanical design optimisation is proposed. The stringer flange should incorporate a ply drop-off strategy or geometrical tapering towards the edge. By gradually reducing the thickness of the stringer foot at its boundary, the stiffness gradient is smoothed. This reduction in stiffness discontinuity would lower the peak peel stresses at the bond line.

In parallel with mechanical improvements, future design principles must embrace the concept of "smart structures". The design of the skin-stringer interface should explicitly accommodate the integration of the SHM sensors proposed in Section 6.4.2. Designing recesses or dedicated bond channels for these sensors within the stringer layup would protect them from environmental exposure while ensuring direct coupling with the laminate strain field. This integration represents a fundamental shift from designing solely for strength to designing for life-cycle manageability.

7 Conclusion and Future Work

7.1 Conclusion

The primary objective of this research was to evaluate the structural integrity of the Airbus A350F MDCD under low-velocity impact conditions. By developing a high-fidelity, multi-scale finite element model, this thesis successfully bridged the gap between academic coupon-level studies and the complex structural reality of a full-scale industrial assembly. The use of an explicit dynamic solver, combined with Hashin's failure criteria for intralaminar damage and cohesive zone modelling for interlaminar delamination, proved to be a robust methodology for predicting the onset and propagation of failure in large composite structures.

The numerical results have quantified specific damage thresholds that are critical for the operational safety of the airframe. At the **$5\,J$ impact energy level**, the door structure exhibited a purely elastic response with no permanent deformation or internal damage, confirming its resilience to minor operational handling. However, the **$20\,J$ impact scenario** identified a critical vulnerability. At this energy level, the simulation predicted the onset of significant internal delamination and matrix cracking at the skin-stringer interface, despite minimal external surface indentation. This confirms the presence of a "latent defect" threshold where structural integrity is compromised without visual indication, validating the concept of BVID in stiffened fuselage panels.

Furthermore, the investigation into the **$40\,J$ impact case** revealed extensive damage propagation, characterized by complete debonding of the stringer flange and severe fibre rupture in the outer skin. The failure mechanism was dominated by the stiffness mismatch between the monolithic skin and the omega stringer foot, which generated high localised peel stresses. This finding highlights that the critical failure mode for this assembly is not the puncture of the skin itself, but the decohesion of the stiffening elements, which drastically reduces the buckling stability of the cargo door under flight loads

7.2 Recommendations for Future Work

While this study has established a validated numerical framework for impact analysis, further research is recommended to expand the scope and applicability of these findings.

7.2.1 Experimental Validation

To fully validate the specific stiffness degradation (SDEG) values and damage evolution rates observed in the numerical model, a physical test campaign is recommended. A representative sub-component of the cargo door, specifically a single omega stringer bonded to a curved skin panel, should be manufactured and subjected to instrumented drop-weight impact testing. Correlating the experimental force-time histories and ultrasonic C-scan data with the FEA predictions would refine the material card parameters and enhance the predictive accuracy of the model.

7.2.2 Residual Strength Analysis (Compression After Impact)

The current study focused on the damage creation phase. However, the ultimate safety concern for a pressurised fuselage is its ability to carry load after being damaged. Future work should extend this analysis by importing the damaged mesh state (including the delamination field) into a static implicit solver to perform a "Compression After Impact" (CAI) simulation. This would quantify the reduction in buckling strength caused by the stringer debonding and determine the residual safety factor of the damaged door under ultimate flight loads.

7.2.3 Environmental Sensitivity

The fracture toughness (G_C) of the epoxy adhesive used in the cohesive zone model is sensitive to environmental conditions. It is recommended that future simulations investigate the effects of hygrothermal ageing (moisture absorption and thermal cycling) on the bond line interface. By degrading the cohesive properties to simulate an aircraft near the end of its service life, the research could determine if the BVID threshold drops significantly for aged airframes, potentially necessitating more frequent inspection intervals for older aircraft.

References

1. Glazer N. Composite Aircraft: 4 Popular Composite Aircraft Built to Date [Internet]. 2020 [cited 2025 Oct 12]. Available from: https://www.pilotmall.com/blogs/news/composite-aircraft-4-popular-composite-aircraft-built-to-date?srsltid=AfmBOoq533RV_7xW5t9meSTzIPUL0L_4h6CbVQvJxyrfXQauH1nECSOi

2. Aerodine Composites. How Aircraft Composites are Making Aircraft Lighter and More Fuel-Efficient | Aerodine Composites [Internet]. [cited 2025 Oct 12]. Available from: https://www.aerodinecomposites.com/news/how-aircraft-composites-are-making-aircraft-lighter-and-more-fuel-efficient/

3. Giurgiutiu V. Impact and Acoustic Emission Monitoring for Aerospace Composites SHM. Structural Health Monitoring of Aerospace Composites. 2016;317–94. doi:10.1016/B978-0-12-409605-9.00009-X

4. Mansuri AK, Medhane SL, Gunjal SU. COMPARATIVE STUDY OF ALUMINIUM LITHIUM ALLOY AND COMPOSITES. International Journal of Science, Technology & Management [Internet]. 2015 Mar [cited 2025 Oct 12];04(03). Available from: www.ijstm.com

5. Malaimeham S, Vinaitheerthan S. Finite element analysis in wheel crushing tests: Correlating simulation and physical testing for Aluminum alloy wheels. Proceedings of the Institution of Mechanical Engineers, Part D: Journal of Automobile Engineering. 2025 Jan 6. doi:10.1177/09544070241308630

6. Korukonda SK. Evolution of Aerospace Materials: A Review. International Research Journal of Engineering and Technology (IRJET). 2022 Apr;09(04).

7. Rafi HA. IMPACT OF COMPOSITE MATERIALS ON AIRCRAFT WEIGHT REDUCTION, FUEL EFFICIENCY, AND PERFORMANCE IN

COMMERCIAL AVIATION. International journal of mechanical engineering. 2024 Dec 4;04(01):21–35. doi:10.55640/ijme-04-01-06

8. Zhu L, Li N, Childs PRN. Light-weighting in aerospace component and system design. Propulsion and Power Research. 2018 Jun;7(2):103–19. doi:10.1016/j.jppr.2018.04.001

9. Salkind M. Fatigue of Composites. In: Composite Materials: Testing and Design (Second Conference). ASTM International; 1972. p. 143–69. doi:10.1520/STP27745S

10. Dutton Stuart, Kelly Donald, Baker Alan. Composite Materials for Aircraft Structures, Second Edition . American Institute of Aeronautics and Astronautics; 2004.

11. Tabatabaeian A, Jerkovic B, Harrison P, Marchiori E, Fotouhi M. Barely visible impact damage detection in composite structures using deep learning networks with varying complexities. Compos B Eng. 2023;264:110907. doi:https://doi.org/10.1016/j.compositesb.2023.110907

12. Giurgiutiu V. 7.19 Smart Materials and Health Monitoring of Composites. In: Beaumont PWR, Zweben CH, editors. Comprehensive Composite Materials II [Internet]. Oxford: Elsevier; 2018. p. 364–81. Available from: https://www.sciencedirect.com/science/article/pii/B9780128035818100438 doi:https://doi.org/10.1016/B978-0-12-803581-8.10043-8

13. Bouvet C, Rivallant S. 2 - Damage tolerance of composite structures under low-velocity impact. In: Silberschmidt V, editor. Dynamic Deformation, Damage and Fracture in Composite Materials and Structures (Second Edition) [Internet]. Woodhead Publishing; 2023. p. 3–28. Available from: https://www.sciencedirect.com/science/article/pii/B9780128239797000028 doi:https://doi.org/10.1016/B978-0-12-823979-7.00002-8

14. Völkerink O, Hühne C. Virtual testing for design and certification of (fusion) bonded longitudinal joints in a fibre composite fuselage: A

proposal using FEM-based progressive damage analysis. Composites Part C: Open Access. 2022;7:100236. doi:https://doi.org/10.1016/j.jcomc.2022.100236

15. EASA. Easy Access Rules for Acceptable Means of Compliance for Airworthiness of Products, Parts and Appliances (AMC-20). 2023. Report.

16. EASA. Proposed CM-S-014 Modelling & Simulation – for consultation. 2020. Report.

17. Talreja R, Singh CV. Damage and Failure of Composite Materials. Cambridge University Press; 2012. doi:10.1017/CBO9781139016063

18. Maria M. Advanced composite materials of the future in aerospace industry. INCAS BULLETIN. 2013 Sep 6;5(3):139–50. doi:10.13111/2066-8201.2013.5.3.14

19. Talreja R. On Failure Theories for Composite Materials. In. 2016. p. 379–88. doi:10.1007/978-981-10-0959-4_21

20. Kim JI, Huh YH, Kim YH. Static Residual Tensile Strength Response of GFRP Composite Laminates Subjected to Low-Velocity Impact. Applied Sciences. 2020;10(16). doi:10.3390/app10165480

21. Kim EH, Rim MS, Lee I, Hwang TK. Composite damage model based on continuum damage mechanics and low velocity impact analysis of composite plates. Compos Struct. 2013;95:123–34. doi:https://doi.org/10.1016/j.compstruct.2012.07.002

22. Guo Q, Yao W, Li W, Gupta N. Constitutive models for the structural analysis of composite materials for the finite element analysis: A review of recent practices. Compos Struct. 2021;260:113267. doi:https://doi.org/10.1016/j.compstruct.2020.113267

23. FedEx. Airbus 52 A300 A310 Doors. 2001.

24. Liebeck RH. Design of the Blended Wing Body Subsonic Transport. J Aircr. 2004 Jan;41(1):10–25. doi:10.2514/1.9084

25. Leishman JGordon. Introduction to aerospace flight vehicles. Embry-Riddle Aeronautical University; 2023.

26. Abbott R. ANALYSIS & DESIGN OF COMPOSITE & METALLIC FLIGHT VEHICLE STRUCTURES. 2017.

27. Megson THG. Aircraft structures for engineering students. 6th ed. Butterworth-Heinemann is an imprint of Elsevier; 2017. 891 p.

28. Niu Chunyun. Airframe Stress Analysis and Sizing. Hong Kong Conmilit Press Ltd.; 2001.

29. Soler Manuel. Fundamentals of aerospace engineering : an introductory course to aeronautical engineering. Create Space; 2014.

30. Sukumar Dhanapalan. MAINTENANCE OF AIRFRAME AND SYSTEMS DESIGN . SCHOOL OF AERONAUTICS (NEEMRANA) . p. 1–17.

31. Andrew Wood. AeroToolbox [Internet]. 2022 [cited 2025 Nov 18]. Aircraft Fuselage Structural Design and Layout. Available from: https://aerotoolbox.com/fuselage-structure/

32. Hüppauff J, Nagaraj V, Motsch-Eichmann N. DEVELOPMENT OF AN INNOVATIVE THERMOPLASTIC DOOR- SURROUND-STRUCTURE FOR A SINGLE AISLE-AIRCRAFT. 2023.

33. Swapnil J. Soni BSKNCCSTK. Stress Analysis of Door and Window of Boeing 787 Passenger Aircraft Subjected to Biaxial Loading. International Journal of Engineering Research & Technology (IJERT). 2014 Mar;3(3):2252–6.

34. Schmidt Daniel and Kolbe A and KR and WP and LS and SS and von DF and TJ and BC and N Ben. Development of a Door Surround Structure with Integrated Structural Health Monitoring System. In: Wölcken Piet Christof and Papadopoulos M, editor. Smart Intelligent Aircraft Structures (SARISTU). Cham: Springer International Publishing; 2016. p. 935–45.

35. Airbus. Airbus [Internet]. 2025 [cited 2025 Nov 23]. A350F: what makes the world’s largest main-deck cargo door a special one. Available from: https://aircraft.airbus.com/en/newsroom/web-story/2025-06-a350f-what-makes-the-worlds-largest-main-deck-cargo-door-a-special-one

36. Airbus. A330-200F A versatile and flexible freighter [Internet]. 2026 [cited 2025 Dec 22]. Available from: https://www.aircraft.airbus.com/en/aircraft/freighters/a330-200f

37. EFW. A330P2F [Internet]. [cited 2025 Dec 22]. Available from: https://www.elbeflugzeugwerke.com/en/solutions/freighter-conversion/a330p2f/

38. Cui Z, Wu H, Zhou M, Cui Z, Huang H, Liu Z. Research on the Design of Aviation and Aerospace Hatch Door Mechanisms and Their Future Bionic Prospects. Aerospace. 2024;11(8). doi:10.3390/aerospace11080601

39. Airbus. A350F: what makes the world’s largest main-deck cargo door a special one [Internet]. 2025 [cited 2025 Dec 22]. Available from: https://www.aircraft.airbus.com/en/newsroom/web-story/2025-06-a350f-what-makes-the-worlds-largest-main-deck-cargo-door-a-special-one

40. Boeing. Boeing: 777 Design Highlights [Internet]. 2026 [cited 2025 Dec 22]. Available from: https://www.boeing.com/commercial/777/design-highlights

41. Kansas Modification Center. Loaded with innovation [Internet]. 2023 [cited 2025 Dec 22]. Available from: https://www.kansasmod.com/features

42. David Müzel S, Bonhin EP, Guimarães NM, Guidi ES. Application of the Finite Element Method in the Analysis of Composite Materials: A Review. Polymers (Basel). 2020;12(4). doi:10.3390/polym12040818

43. SAAB. Saab and Boeing 787 – 20 years of successful collaboration [Internet]. 2025 [cited 2026 Feb 11]. Available from: https://www.saab.com/newsroom/stories/2025/december/saab-and-boeing-787--20-years-of-successful-collaboration

44. Patrik SCHMIEDEL, Manuel HOLZHEIMER. Development of CFRP Aircraft Doors with the Interaction of NDT and Strength Analysis. 19th World Conference on Non-Destructive Testing 2016. 2016 Jun 13;21.

45. Zhang J, Lin G, Vaidya U, Wang H. Past, present and future prospective of global carbon fibre composite developments and applications. Compos B Eng. 2023 Feb;250:110463. doi:10.1016/j.compositesb.2022.110463

46. Castanie B, Azoti W, Crouzeix L, Bello A, Taborda RP, Mahmood A, et al. Review of monolithic composite laminate and stiffened structures in aeronautic applications. Composites Part C: Open Access. 2025 Jul;17:100585. doi:10.1016/j.jcomc.2025.100585

47. Patel M, Sonkar L, Patel S. Assessment of Ply Stacking Sequence Effect on Damage Behavior of CFRP Composite Laminate Under Low-Velocity Impacts. Advances in Materials Science and Engineering. 2025 Jan 24;2025(1). doi:10.1155/amse/4349535

48. Chen M, Zhang B, Allegri G, Hallett SR. Effects of carbon-fibre Z-pins on the through-thickness tensile strength of curved composite laminates under four-point bending. Compos B Eng. 2024 Aug;283:111629. doi:10.1016/j.compositesb.2024.111629

49. Zhou P, Shen Y, Zheng Y, Zheng Y, Guo B, Du Y. A comprehensive review of ground support equipment scheduling for aircraft ground handling services. Transp Res E Logist Transp Rev. 2025 Nov;203:104341. doi:10.1016/j.tre.2025.104341

50. AD Balk. Safety of ground handling. Schiphol: NLR Safety and Security. 2008.

51. Caminero MA, García-Moreno I, Rodríguez GP, Chacón JM. Internal damage evaluation of composite structures using phased array ultrasonic technique: Impact damage assessment in CFRP and 3D printed reinforced composites. Compos B Eng. 2019 May;165:131–42. doi:10.1016/j.compositesb.2018.11.091

52. Deng K, Liu H, Yang L, Addepalli S, Zhao Y. Classification of barely visible impact damage in composite laminates using deep learning and pulsed thermographic inspection. Neural Comput Appl. 2023 May 31;35(15):11207–21. doi:10.1007/s00521-023-08293-7

53. Katunin A, Wronkowicz-Katunin A, Dragan K. Impact Damage Evaluation in Composite Structures Based on Fusion of Results of Ultrasonic Testing and X-ray Computed Tomography. Sensors. 2020 Mar 27;20(7):1867. doi:10.3390/s20071867

54. Bergan AC, Langley Research Center issuing body. Computational performance of progressive damage analysis of composite laminates using Abaqus/Explicit with 16 to 512 CPU cores. Hampton, Virginia: National Aeronautics and Space Administration, Langley Research Center; 2019. (NASA/TM ; 2019-220251).

55. Gattmah J, Shihab SK, Mohamed MT, Abbas AL. Effects of Increasing Mass Scaling in 3D Explicit Finite Element Analysis on the Wire Drawing Process. IOP Conf Ser Mater Sci Eng. 2021 Feb 1;1076(1):012072. doi:10.1088/1757-899X/1076/1/012072

56. Xu ZW, Chen YH, Cantwell WJ, Guan ZW. Multiscale modelling of scaling effects in the impact response of plain woven composites. Compos B Eng. 2020 May;188:107885. doi:10.1016/j.compositesb.2020.107885

57. Airbus. A350F [Internet]. 2025 [cited 2026 Feb 11]. Available from: https://www.linkedin.com/posts/airbus_a350f-freighter-cargo-activity-7216442939776864256-q5Fs/

58. Gardiner G. Manufacturing the upper half of the Multifunctional Fuselage Demonstrator (MFFD) [Internet]. 2021 [cited 2026 Feb 11]. Available from: https://www.compositesworld.com/articles/manufacturing-the-upper-half-of-the-multifunctional-fuselage-demonstrator-mffd

59. Madier Dominique. Practical finite element analysis for mechanical engineers. FEA Academy; 2020. 639 p.

60. Abaqus. 23.6.2 Choosing a shell element [Internet]. 2006 [cited 2026 Feb 11]. Available from: https://classes.engineering.wustl.edu/2009/spring/mase5513/abaqus/docs/v6.6/books/usb/default.htm?startat=pt06ch23s06alm15.html

61. Thorsson SI, Waas AM, Rassaian M. Low-velocity impact predictions of composite laminates using a continuum shell based modeling approach part A: Impact study. Int J Solids Struct. 2018 Dec;155:185–200. doi:10.1016/j.ijsolstr.2018.07.020

62. Abaqus. 18.1.1 User subroutines: overview [Internet]. 2015 [cited 2026 Feb 11]. Available from: http://130.149.89.49:2080/v2016/books/usb/default.htm?startat=pt04ch18s01aus106.html

63. Abaqus. 11.7.1 Rigid parts [Internet]. 2006 [cited 2026 Feb 11]. Available from: https://classes.engineering.wustl.edu/2009/spring/mase5513/abaqus/docs/v6.6/books/usi/default.htm?startat=pt03ch11s07s01.html

64. Abaqus. 39.1.2 Common difficulties associated with contact modeling in Abaqus/Standard [Internet]. 2015 [cited 2026 Feb 11]. Available from: http://130.149.89.49:2080/v2016/books/usb/default.htm?startat=pt04ch18s01aus106.html

65. Abaqus. 21.1.4 Section controls [Internet]. 2006 [cited 2026 Feb 11]. Available from: https://classes.engineering.wustl.edu/2009/spring/mase5513/abaqus/docs/v6.6/books/usb/default.htm?startat=pt06ch21s01aus90.html

66. Experts Of CAE Assistant Group. What is Abaqus Element Deletion? | When use it: Abaqus Element Deletion Criteria [Internet]. 2024 [cited 2026 Feb 11]. Available from: https://caeassistant.com/blog/abaqus-element-deletion-criteria/

67. Abaqus. 21.3.3 Damage evolution and element removal for fiber-reinforced composites [Internet]. 2010 [cited 2026 Feb 11]. Available from: http://orpheus.nchc.org.tw:2080/v6.10/books/usb/default.htm?startat=pt05ch21s03abm45.html

68. EASA. Easy Access Rules for Large Aeroplanes (CS-25) SUBPART D – DESIGN AND CONSTRUCTION [Internet]. 2023 [cited 2026 Feb 11]. Available from: https://www.easa.europa.eu/en/document-library/easy-access-rules/online-publications/easy-access-rules-large-aeroplanes-cs-25?page=22#_DxCrossRefBm548991409

69. ASTM. Test Method for Measuring the Damage Resistance of a Fiber-Reinforced Polymer Matrix Composite to a Drop-Weight Impact Event. West Conshohocken, PA: ASTM International; 2025. doi:10.1520/D7136_D7136M-25

70. Falcó O, Lopes CS, Sommer DE, Thomson D, Ávila RL, Tijs BHAH. Experimental analysis and simulation of low-velocity impact damage of composite laminates. Compos Struct. 2022 May;287:115278. doi:10.1016/j.compstruct.2022.115278

71. Abaqus. 19.3.1 Damage and failure for fiber-reinforced composites: overview [Internet]. 2006 [cited 2026 Feb 4]. Available from: https://classes.engineering.wustl.edu/2009/spring/mase5513/abaqus/docs/v6.6/books/usb/default.htm?startat=pt05ch19s03abm40.html

72. Abaqus. 17.2.1 Linear elastic behavior [Internet]. 2006 [cited 2026 Feb 8]. Available from: https://classes.engineering.wustl.edu/2009/spring/mase5513/abaqus/docs/v6.6/books/usb/default.htm?startat=pt05ch17s02abm02.html

73. Abaqus. 19.3.2 Damage initiation for fiber-reinforced composites [Internet]. 2006 [cited 2026 Feb 4]. Available from: https://classes.engineering.wustl.edu/2009/spring/mase5513/abaqus/docs/v6.6/books/usb/default.htm?startat=pt05ch19s03abm41.html

74. Veidth M. What is Hashin Failure Criteria? | Hashin Damage in Abaqus [Internet]. 2024 [cited 2026 Feb 4]. Available from: https://caeassistant.com/blog/hashin-failure-criteria-hashin-damage-abaqus/

75. Abaqus. 19.3.3 Damage evolution and element removal for fiber-reinforced composites [Internet]. 2006 [cited 2026 Feb 4]. Available from: https://classes.engineering.wustl.edu/2009/spring/mase5513/abaqus/docs/v6.6/books/usb/default.htm?startat=pt05ch19s03abm41.html

76. Abaqus. 32.5.3 Modeling with cohesive elements [Internet]. 2015 [cited 2026 Feb 8]. Available from: http://130.149.89.49:2080/v2016/books/usb/default.htm?startat=pt06ch32s05alm42.html

77. Abaqus. 37.1.10 Surface-based cohesive behavior [Internet]. 2015 [cited 2026 Feb 8]. Available from: http://130.149.89.49:2080/v2016/books/usb/default.htm?startat=pt09ch37s01alm66.html

78. Dassault Systemes. Contact Cohesive Behavior [Internet]. 2025 [cited 2026 Feb 8]. Available from: https://docs.software.vt.edu/abaqusv2025/English/?show=SIMACAEITNRefMap/simaitn-c-cohesivebehavior.htm

79. Abaqus. 32.5.1 Cohesive elements: overview [Internet]. 2015 [cited 2026 Feb 8]. Available from: http://130.149.89.49:2080/v2016/books/usb/default.htm?startat=pt09ch37s01alm66.html

80. Abaqus. 2.7.1 Delamination analysis of laminated composites [Internet]. 2006 [cited 2026 Feb 8]. Available from: https://classes.engineering.wustl.edu/2009/spring/mase5513/abaqus/docs/v6.6/books/bmk/default.htm?startat=ch02s07ach148.html

81. Abaqus. 6.3.3 Explicit dynamic analysis [Internet]. 2004 [cited 2026 Feb 10]. Available from: https://classes.engineering.wustl.edu/2009/spring/mase5513/abaqus/docs/v6.5/books/usb/default.htm?startat=pt03ch06s03at07.html#usb-anl-aexpdynamic

82. Correas AC, Crespo AC, Ghasemnejad H, Roshan G. Analytical Solutions to Predict Impact Behaviour of Stringer Stiffened Composite Aircraft Panels. Applied Composite Materials. 2021 Aug 25;28(4):1237–54. doi:10.1007/s10443-021-09909-8

83. Falcó O, Lopes CS, Sommer DE, Thomson D, Ávila RL, Tijs BHAH. Experimental analysis and simulation of low-velocity impact damage of composite laminates. Compos Struct. 2022 May;287:115278. doi:10.1016/j.compstruct.2022.115278

84. Cook L, Boulic A, Harris D, Bellamy A, Irving P. Reliability of Damage Detection in Advanced Composite Aircraft Structures. 2013.

85. Test Method for Compressive Residual Strength Properties of Damaged Polymer Matrix Composite Plates. West Conshohocken, PA: ASTM International; 2023. doi:10.1520/D7137_D7137M-23

86. Universal Grip CO. ASTM D7137.

87. Olsson R. Strength of composite laminates after impact: background and recommendations. 2011.

88. Reymer P, Leski A. Flight Loads Acquisition for PZL-130 Orlik TCII Full Scale Fatigue Test. Fatigue of Aircraft Structures. 2011 Jan 1;2011(3). doi:10.2478/v10164-010-0041-7

Appendices

Appendix A Ethical approval letter

Letter.pdf

26 June 2025

Dear Mr Chakir ,

Reference: CURES/25804/2025
Project ID: 29159
Title: "Numerical Modelling of Structural Compromising Events on Various Types of Typical Airframe Structures (Crashworthiness or Bird Strike)"

We are pleased to inform you that you have successfully declared that your research project is a **Literature Review – based solely on openly available literature which is in the public domain, and you are undertaking desk-based research not involving any other form of data or information.**

You have also confirmed that your project **does not meet** any of the literature review specified exceptions, listed both within the relevant section of the CURES form and below:

1) Your supervisor has requested that you apply for approval through CURES because:

- The journals or data are in a sensitive area (please discuss this with your supervisor)
- The project will be embargoed **i.e. will not be publicly available via the Cranfield library immediately or longer term**

2) Approval is/will be specifically required by another external body e.g. journal publishers

Therefore, **you do not require ethical approval** and your CURES application will be automatically closed.

Please keep a copy of this letter safe, if this exception is in relation to your thesis project, you will need to include a copy with your final thesis submission.

If you have any queries, please contact CURES Support.

We wish you every success with your project.

Regards,

CURES Team

Page 1 of 1